ISAE 2023

THE 2023 INTERNATIONAL SYMPOSIUM ON ADVANCED ENGINEERING

February 13-15, 2023

Kimdo Royal Hotel
Ho Chi Minh City, Vietnam

VNUHCM PRESS

TABLE OF CONTENTS

Acknowledgement

The Symposium Organizers would like to acknowledge:

General Co-chairs

- Jei-Pil Wang, Pukyong National University, Republic of Korea
- Nguyen Tan Tien, HCMC University of Technology, DCSELab, Vietnam
- Dong Sy Thien Chau, Ton Duc Thang University, Vietnam

Organizing Committee Co-chairs

- Woon Ik Park, Pukyong National University
- Kyu-Nam Rhee, Pukyong National University
- Tran Thanh Phuong, Ton Duc Thang University
- Nguyen Huy Hung, Saigon University

Program Committee Co-chairs

- Jung Min Sohn, Pukyong National University
- Huynh Van Van, Ton Duc Thang University
- Duong Van Tu, HCMC University of Technology, VNU-HCM
- Thanh-Long Le, HCMC University of Technology, VNU-HCM

Symposium Program

Date	Contents	Time	Place	Remark
13th February Mon	**Registration**	17:00 - 20:00		
	Welcome Reception	18:00 - 20:00		
14th February Tue.	**Registration**	09:00 - 12:00		
	Opening Ceremony Prof. Jei-Pil Wang, Dean of Engineering College, PKNU	09:00 - 09:10	King hall	1min/ea
	Keynote Speech 1 Prof. Mochammad Agung Wibowo, Dean Faculty of Engineering, Diponegoro University **Keynote Speech 2** Prof. Sang Bong Kim, Emeritus Professor, Pukyong National University	09:10 - 10:10	King hall	30min/ea
	Coffee Break	10:10 - 10:30		
	Keynote Speech 3 Prof. Tan Tien Nguyen, Director, HCMC University of Technology, DCSELAB **Keynote Speech 4** Prof. Le Van Sy, Vice Rector, PetroVietnam College	10:30 - 11:30	King hall	30min/ea
	Lunch	11:30 - 13:00		
	Oral Presentation I King: Mechanical, Material Science, Chemical Engineering Saigon: Advanced Electrical, Electronic, Computer and Communication Technology Tulip: Biomedical, Industrial, Civil, Architecture, Others	13:00 - 14:20	King hall Saigon hall Tulip hall	20min/ea 4papers
	Coffee Break	14:20 - 14:40		
	Oral Presentation II King: Mechanical, Material Science, Chemical Engineering Saigon: Advanced Electrical, Electronic, Computer and Communication Technology Tulip: Biomedical, Industrial, Civil, Architecture, Others	14:40 - 16:00	King hall Saigon hall Tulip hall	20min/ea 4papers
	Coffee Break	16:00 - 16:20		
	Oral Presentation III Saigon: Mechanical, Material Science, Chemical Engineering Tulip: Mechanical, Material Science, Chemical Engineering	16:20 - 17:40	Saigon hall Tulip hall	20min/ea 4papers
	Poster Presentation I	16:20 - 17:00	King hall	
	Poster Presentation II	17:20 - 18:00	King hall	
	Banquet	18:10 - 20:30	Queen hall	
15th February Tue.	**Technical Tour** Ton Duc Thang University Ho Chi Minh City University of Technology	09:00 - 12:00		

Oral Presentation I (14th February Tue. 13:00 ~ 14:20)

King Hall	**Mechanical, Material Science, Chemical Engineering**
Chairperson	Woon Ik Park / Pukyong National University
O-1-1	**Transparent conductive film with electrospun silver microfibers for LED media façade** Dong-Youn Shin Dept. Nanotechnology Engineering, Pukyong National University
O-1-2	**A study on the recovery of pig iron with low sulfur from copper smelting slag by reduction smelting** Urtnasan Erdenebold School of Technology, Mongolian University of Science and Technology
O-1-3	**Strain hardening recovery mediated by coherent precipitates in lightweight steel** Sung-Dae Kim Dept. of Materials and Science, Pukyong National University
O-1-4	**Charge transfer doping for high-performance flexible transistors based on emerging semiconductor materials** Jiyoul Lee Dept. of Nanotechnology Engineering, Pukyong National University
Saigon Hall	**Advanced Electrical, Electronic, Computer and Communication Technology**
Chairperson	Jei-Pil Wang / Pukyong National University
O-2-1	**Secure wireless communications at UVC bands: A review** Yeon Ho Chung Dept. of Information and Communications Engineering, Pukyong National University
O-2-2	**HMM with hybrid output models in geometric and gamma distributions** Bong-Kee Sin Division of Computer Engineering and AI, Pukyong National University
O-2-3	**Self-energy recycling in AF multi-relay full-duplex networks: Performance analysis** Tan N. Nguyen Communication and Signal Processing Research Group, Ton Duc Thang University
O-2-6	**On the physical layer security of RIS-assisted dual-hop asymmetric networks** Lam-Thanh TU Communication and Signal Processing Research Group, Ton Duc Thang University
Tulip Hall	**Biomedical, Industrial, Civil, Architecture, Others**
Chairperson	Jung Min Sohn / Pukyong National University
O-3-1	**Analysis of ductile-to-brittle transition temperature on DH36 high-strength steel using Charpy V-notch test and nonlinear finite element method** Haris Nubli Dept. of Marine Convergence Design Engineering, Pukyong National University
O-3-2	**Properties of cement paste using silica functionalized MWCNT dispersed by polycarboxylate ester** Chul-Woo Chung Division of Architectural and Fire Protection Engineering, Pukyong National University
O-3-3	**Multi-criteria decision-making model for reverse logistics in E-commerce** Van-Hau Nguyen Dept. of Industrial Systems Engineering, Ho Chi Minh City University of Technology
O-3-4	**Aggregate planning in manufacturing industry: A case study in Vietnam** Thanh-Thuy Truong Pham Dept. of Industrial Systems Engineering, Ho Chi Minh City University of Technology

Oral Presentation II (14th February Tue. 14:40 ~ 16:00)

King Hall	**Mechanical, Material Science, Chemical Engineering**
Chairperson	Thanh-Long Le / Ho Chi Minh City University of Technology, VNU-HCM
O-1-5	**Strong and stretchable thin film hydrogels** Hong Hieu Le Hutech University
O-1-6	**Application of multi-PID controllers for fire resistance testing furnace** Ho Hai Dang National Key Laboratory of Digital Control and System Engineering
O-1-7	**Development of rubber wheel track slip resistance tester on photovoltaic panel** Anh Duy Hoang Ngoc National Key Laboratory of Digital Control and System Engineering
O-1-8	**Evaluation of parameter effect on swimming trajectory of elongated undulating fin using computational fluid dynamic model** Quoc Tuan Vu National Key Laboratory of Digital Control and System Engineering
Saigon Hall	**Advanced Electrical, Electronic, Computer and Communication Technology**
Chairperson	Nguyen Huy Hung / Saigon University
O-2-4	**Microwave and millimeter-wave reconfigurable antenna for 5G smart wireless applications** Truong Khang Nguyen Division of Computational Physics, Institute for Computational Science, Ton Duc Thang University
O-2-6	**On the physical layer security of RIS-assisted dual-hop asymmetric networks** Lam-Thanh TU Communication and Signal Processing Research Group, Ton Duc Thang University
O-2-7	**A modified Kalman speed observer for sensorless control of induction motor** Nguyen Quang Dung Faculty of Electrical and Electronics Engineering, Ton Duc Thang University
O-2-8	**Direct torque controlled PMSM drive with space vector PWM and fuzzy logic** Quang Thanh Nguyen Faculty of Electrical and Electronics Engineering, Ton Duc Thang University
Tulip Hall	**Biomedical, Industrial, Civil, Architecture, Others**
Chairperson	Duong Van Tu / Ho Chi Minh City University of Technology, VNU-HCM
O-3-5	**Effect of pavement structure-cover soil system on behavior of buried precast box culverts under vehicle live loading** Nguyen Van Toan Thuyloi University Southern Campus
O-3-6	**Numerical analysis of local scour of the offshore wind turbines** Thi-Hong-Nhi Vuong Faculty of Transportation Engineering, Ho Chi Minh City University of Technology
O-3-7	**Numerical study of modeling and hydrodynamic characteristics of the automated hand-washing system** Thanh-Long Le Faculty of Mechanical Engineering, Ho Chi Minh City University of Technology
O-3-8	**Design of the smart cranial molding helmet for infant SCMH2023** Bao Vy Phan Faculty of Mechanical Engineering, HCMC University of Technology

Oral Presentation III (14th February Tue. 16:20 ~ 17:40)

Saigon Hall	**Mechanical, Material Science, Chemical Engineering**
Chairperson	Nguyen Quoc Chi / Ho Chi Minh City University of Technology, VNU-HCM
O-1-9	**Mechanical modular design of photovoltaic panel cleaning robot** Tan Tien Nguyen National Key Laboratory of Digital Control and System Engineering (DCSELab)
O-1-10	**Modeling of parallel power MOSFETs in steady-state** Minh Nhat Huynh National Key Laboratory of Digital Control and System Engineering
O-1-11	**Optimal central pattern generator for swimming gait of robotic fish using mutant particle swarm optimization** Quoc Tuan Vu National Key Laboratory of Digital Control and System Engineering
Tulip Hall	**Mechanical, Material Science, Chemical Engineering**
Chairperson	Tran Thanh Phuong / Ton Duc Thang University
O-1-13	**Torque balance of coaxial BLDC motor using feedback linearization in presence of cogging torque** Lam Cuong Quoc Thai National Key Laboratory of Digital Control and System Engineering
O-1-14	**A grey predictor-based feedforward controller and its application to force control of hydraulics system** Tran Nguyen Duy Phuong Faculty of Mechanical Engineering, HCMC University of Technology
O-1-15	**Designing a meal support system for the elderly MSS2023** Nguyen Quang Minh Faculty of Mechanical Engineering, HCMC University of Technology
O-1-16	**Design and simulation of a linear-motion compliant mechanism** Hai Nhan Le Department of Machine Design, Ho Chi Minh City University of Technology (HCMUT

Poster Presentation I (14th February Tue. 16:20 ~ 17:00, King hall)

Chairperson	Jei-Pil Wang & Woon Ik Park / Pukyong National University
P-1-1	**Comparison of transport property predictions of supercritical hydrocarbon aviation fuels** Hyung Ju Lee Department of Mechanical Engineering, Pukyong National University
P-1-2	**Smart nanotransfer printing process with high resolution at eight-inch wafer scale** Woon Ik Park Department of Materials Science and Engineering, Pukyong National University
P-1-3	**Development of diesel particulate filter on 100kW diesel engine for coastal ship** Min-A Je Pukyong national university
P-1-4	**Hydrophobically crosslinked PDMS-coated PVDF composite membrane for the pervaporation of isopropanol /1.5 pentanediol feed solution** Minyoung Shon Department of Industrial Chemistry, Pukyong National University
P-1-5	**Alloy development and property evaluation on high-temperature structural materials for advanced nuclear/fusion reactor components** Sanghoon Noh Department of Materials Science and Engineering, Pukyong National University
P-1-6	**Non-lead radiation shielding materials using metal salts and polymer composites** Junghwan Kim Department of Materials System Engineering, Pukyong National University
P-1-7	**Vibration-isolator design for electric power generator system under consideration of multi-excitation events** Chan-Jung, Kim School of Mechanical Engineering, Pukyong National University
P-1-8	**A study on the recovery of copper from leachate of solar cells and PV ribbon** Jei-Pil Wang Major of Metallurgical Engineering, Pukyong National University
P-1-9	**Ultraviolet electroluminescence from $CaSiO_3$: Ce^{3+} oxide in a metal-oxide-semiconductor structure** Jongsu Kim Department of Display Science and Engineering, Pukyong National University
P-1-10	**A study on the design of rock crushing machine for mining use** Tserendejid Bayarmaa Department of Mechanical Engineering School of Technology of MUST
P-1-11	**The study on the sintering condition for manufacturing of sintered-wick heat pipe** Yong-Sik Ahn Department of Materials Science and Engineering, Pukyong National University
P-1-12	**Performance evaluation of GCH_4-LOx small rocket engine according to the equivalence ratio variation under a fixed combustion-chamber pressure** Jeong Soo Kim Pukyong National University
P-1-13	**Fabrication of carbon dots (CDs) deposited graphitic carbon nitrides for photocatalytic CO_2 reduction** Minh-Tri Nguyen-Le Laboratory of Advanced Materials Chemistry, Advanced Institute of Materials Science, Ton Duc Thang University
P-1-14	**Reduction-responsive carboxymethyl cellulose-based soft hydrogels for cancer therapy application** Kwon Taek Lim Department of Smart Green Technology Engineering, Pukyong National University
P-1-15	**Experimental evaluation of the electrical and thermal efficiency of dual duct PV/T collectors** Kwnaghwan Choi Department of Refrigeration and Air Conditioning Engineering, Pukyong National University
P-1-17	**Ultraviolet electroluminescent sensor in metal-oxide-semiconductor structure** Jongsu Kim Department of Display Science and Engineering, Pukyong National University

Poster Presentation II (14th February Tue. 17:20 ~ 18:00, King hall)

Chairperson	Kyu Nam Rhee & Jung Min Sohn / Pukyong National University
P-1-16	**Motion control for two-wheeled mobile inverted pendulum using a MIMO robust servo controller** Dae Hwan Kim Realmaker.Inc
P-2-1	**Switching control of nonlinear systems with multiple inputs and multiple outputs** Seong Woo Kwak Department of Control and Instrumentation Engineering, Pukyong National University
P-2-2	**Distribution cable fault location using line impedance resonance analysis** Chun-Kwon Lee Department of Control and Instrumentation Engineering, Pukyong National University
P-2-3	**Inspection of welding bead defectiveness using brightness values** Jong-Nam Kim Division of Computer Engineering and AI, Pukyong National University
P-2-4	**Test bed methods for big data collection based on Klean IoT AP** Chang Soo Kim Division of Computer Engineering and AI, Pukyong National University
P-2-5	**Application of dimension reduction techniques for similar data search in oceanographic observation archives** Ha-Joo Song Division of Computer Engineering and AI, Pukyong National University
P-2-7	**Fish size detection for a fish farm by using deep learning** Moon G. Joo Pukuong national university
P-2-8	**Spontaneous conformational changes and functions of angiotensin I converting enzyme** Myunggi Yi Major of Biomedical Engineering, Division of Smart Healthcare, Pukyong National University
P-2-9	**CNN and vision transformer-based for video deepfake detection** Ki-Ryong Kwon Division of Computer Engineering and AI, Pukyong National University
P-2-10	**SARS-CoV-2 Omicron RBD binds more weakly to hACE2 than Delta RBD, as shown by the coarse-grained model** Thanh Hoa Le Laboratory of Theoretical and Computational Biophysics, Advanced Institute of Materials Science, Ton Duc Thang University
P-2-11	**A self-attention-based feature learning framework for visual localization** Dae Hwan Kim Realmaker.Inc
P-2-12	**Energy Efficiency Optimization for UAV-enabled Finite Block Length Backscatter Communications** Phuong T. Tran Wireless Communications Research Group, Ton Duc Thang University
P-3-1	**Evaluation of ventilation performance in a multi-use facility for the preparedness to prevent the next pandemic** Chul Kim Department of Architectural Engineering, Pukyong National University
P-3-3	**Development of an evacuation model for fire safety managers** Ryun-Seok Oh Industry-University Cooperation Foundation, Pukyong National University
P-3-4	**Rainfall-runoff-inundation assessment based on the radar rainfall database from the global precipitation climatology centre: A case study in north-central Vietnam** Nguyen Van Toan Thuyloi University Southern Campus
P-3-5	**Production capacity planning in uncertain time condition: A case study at a plastic manufacturing company** Tran Lan Anh Ho Chi Minh City University of Technology

Oral Presentation

[O-1-1] Transparent Conductive Film with Electrospun Silver Microfibers for LED Media Façade

Dong-Youn Shin[1, *, †], Suk-Hwan Ko[2], Gi-Hwan Kang[2]

[1] Dept. Nanotechnology Engineering, Pukyong National University, Republic of Korea

[2] Photovoltaic Laboratory, Korea Institute of Energy Research, Daejeon, Republic of Korea

[†] Leading - Corresponding author: dongyoun.shin@gmail.com

[*] Presenting author: dongyoun.shin@gmail.com

Abstract

As the concern about anthropogenic climate change has arisen, diverse measures to minimize the consumption of CO_2 emission fossil fuels have been taken. Building integrated photovoltaics (BIPV) is one of such measures, which ultimately aims to achieve a zero-energy building by integrating photovoltaic modules into the skin of a building and resultantly by supplying electricity for air conditioning, lighting, and office equipment. However, the monotonous design of a conventional photovoltaic module has been one of sources for low public acceptance and willingness to pay. For increasing public acceptance, one has begun to decorate a photovoltaic module with LEDs, which renders photovoltaic modules act not only as a source of electricity but also as an aesthetic media façade of a building. In this contribution, a novel method to fabricate a low-cost transparent conductive film with electrospun silver microfibers is presented, which is anticipated to be used for the exterior decorative LED media façade on the front surface of a photovoltaic module.

Keywords: *Media façade, Photovoltaic module, Silver microfibers, Transparent conductive film*

[O-1-2] A Study on the Recovery of Pig Iron with Low Sulfurfrom Copper Smelting Slag by Reduction Smelting

Urtnasan Erdenebold[1, *], Jong-Deok Lim[2], Hyun-Jong Kim[2], Seung-Uk Hwang[3], Tae-Yi Kang[3], Jeong-Sik Moon[3], Gyu-Dong Ryu[3], Tae-Jun Jeon[3], Jei-Pil Wang[4, †]

[1] School of Technology, Mongolian University of Science and Technology, in Darkhan, Mongolia
[2] Department of Metallurgical Engineering, Pukyong National University, Busan 48547, Republic of Korea
[3] Division of Convergence Materials Engineering, Major of Metallurgical Engineering, Pukyong National University, Busan 48547, Republic of Korea
[4] Division of Convergence Materials Engineering, Major of Metallurgical Engineering, Department of Marine Convergence Design Engineering (Advanced Materials Engineering), Pukyong National University, Busan 48547, Republic of Korea

[†] Leading - Corresponding author: jpwang@pknu.ac.kr
[*] Presenting author: erdenebold@stda.edu.mn

Abstract

Copper slag elements exist in oxide form and some sulfides may also present in the slag phase. The main components of copper slag are iron oxide and SiO_2, and these exist in copper slag mainly in the form of fayalite ($2FeO \cdot SiO_2$). Sulfur in the copper slag exists in form of FeS and Cu_2S. The aim is to produce a typical foundry pig iron with the chemical composition of C>3.40%, Si 1.40 to 1.80%, Mn 0.30 to 0.90%, P<0.03% and S<0.03% from copper slag. The CaO additives form basic slag with high CaO content and desulphurization may be effectively conducted in the reducing process of the copper slag. Therefore, this study examines how to conduct desulphurization. Reduction smelting with desulphurization additives was used to remove sulfur from the copper slag. The results showed that reduction smelting with CaO additives is possible to manufacture low sulfur pig iron from copper smelting slag.

Keywords: *Copper slag, Desulfurization, CaO addition, Sulphur, Basicity*

[O-1-3] Strain Hardening Recovery Mediated by Coherent Precipitates in Lightweight Steel

Sung-Dae Kim[1, *, †], Jae hoon Jang[2]

[1] Department of Materials and Science, Pukyong National University, Busan, 48513, Republic of Korea

[2] Advanced Metals Division, Korea Institute of Materials Science, Changwon, 51508, Republic of Korea

[†] Leading - Corresponding author: sdkim@pknu.ac.kr

[*] Presenting author: sdkim@pknu.ac.kr

Abstract

Aluminum-containing austenitic high-Mn steels (Fe-Mn-Al-C steels) have been widely revisited as one of the most promising subgroups of the high-Mn steels because of their attractive mechanical properties as well as low specific weight. Addition of 1 wt% Al reduces 1.5% of specific weight, rendering the alloys to be so-called 'light-weight steels' and an encouraging candidate for automotive applications. Deformed microstructure of the Fe-Mn-Al-C can be characterized by the pronounced planar dislocation glide. The origin of the unique deformed structure has been controversially discussed, and the majority of researcher attributes origin of the unexpected finding to the ordered phase in the alloys. That is, the ordered phases dispersed in the austenite matrix hinder dislocation movement, whereas if the ordered phases are sheared by some leading dislocations then the trailing dislocations are easy to glide on the same slip plane ("glide plane softening"). Many researchers agreed the validity of the "glide plane softening" effect, although, there are significant distinctions in the interpretations of the strain hardening process in the alloys. The present study aims to elucidate the deformation mechanism of the Al-added austenitic high-Mn steels by means of transmission electron microscopy (TEM). Especially, we conduct *in-situ* mechanical straining TEM experiments to show the dynamic evolution of the deformed microstructure including the dislocations gliding behavior. We seek to visualize the pronounced planar glide of the dislocations and the process of the mutual intersection of dislocations in the slip bands. In comparison with the previous *post-mortem* analysis on the deformation microstructure of the lightweight high-Mn steels, this study provides more evident clues towards understanding the high strain hardening capacity of the alloys by observing plastic deformation process in real time.

Keywords: *Lightweight steels, Precipitation strengthening, Strain hardening, Dislocation gliding, Transmission electron microscopy (TEM)*

[O-1-4] Charge Transfer Doping for High-Performance Flexible Transistors Based on Emerging Semiconductor Materials

Jiyoul Lee[*, †]

Department of Nanotechnology Engineering, College of Engineering, Pukyong National University, 48513, Republic of Korea

[†] Leading - Corresponding author: jiyoul_lee@pknu.ac.kr
[*] Presenting author: jiyoul_lee@pknu.ac.kr

Abstract

Doping technology, i.e., accurately modulating the charge carrier type and concentration in a controllable manner, is a key technology foundation for modern electronics and optoelectronics; however, for the emerging semiconductor materials, the conventional doping methods by introducing impurities into the nanostructures, results in low efficiency, poor reliability, and host lattice damage. In this presentation, surface charge transfer doping as an effective doping method for conjugated organic semiconductors and two-dimensional semiconductors will be introduced. Unlike the conventional ion doping used in the Si-technology, which implants ions and induces excess charge through counter ions of the implanted ions, the surface charge transfer doping method induces excess charges through the polarization of the material forming the interface with the active semiconducting channel of the transistor.

Herein, surface charge-transfer doping was performed in two ways: i) a thermal deposition of the DNTT monolayer onto the top of a two-dimensional WSe2 semiconductor materials, and ii) the surface polarization doping to a polymer field-effect transistor, where the DPP-2T-TT conjugated polymer and a block- copolymer insulating layer containing a fluorinated group form an interface and induce the excess charges at the interface. For both cases, it is observed that the threshold voltage shifts and the off-current increases after applications of the surface charge transfer doping. These results confirm that the excess charges are effectively induced through the deposition of small molecule organic semiconductors or the application of polymeric insulators containing the fluorine components.

Keywords: *Surface charge transfer doping, Semiconducting materials, Transistors*

[O-1-5] Strong and Stretchable Thin Film Hydrogels

Hong Hieu Le[1, *], Dae Hwan Kim[2, †]

[1] Hutech University, 475A Dien Bien Phu Street, Ward 25, Binh Thanh District, Ho Chi Minh City, 700000, Viet Nam

[2] Realmaker.Inc, R304 B23 Sinseon-ro, Nam-gu, Busan, KS012, Republic of Korea

[†] Leading - Corresponding author: dhkim@realmaker.kr

[*] Presenting author: lh.hieu@hutech.edu.vn

Abstract

Hydrogels are hydrophilic, three-dimensional networks that are able to absorb large quantities of water or biological fluids, and thus have the potential to be used as prime candidates for biosensors, drug delivery vectors, and carriers or matrices for cells in tissue engineering. Hydrogels have received special attention due to their promising properties such as biocompatibility and environmental friendliness, responsiveness to external stimuli, adhesion, and biodegradability. Recently, we have been successful in synthesizing hydrogels that have good mechanical properties: strong and stretchable properties were synthesized based on physical interaction (pi-pi interaction). The stress and strain properties of these hydrogels were indicated by the tensile test.

Keywords: *Hydrogels, Stretchable hydrogel, Strong hydrogel, Biomaterials*

[O-1-6] Application of Multi-PID Controllers for Fire Resistance Testing Furnace

Ho Hai Dang[1, *], Nguyen Quoc Bao, Nguyen Duc Tai[1], Van Tu Duong[1, 2, 3, †], Huy Hung Nguyen[4], Tan Tien Nguyen[1, 2, 3]

[1] National Key Laboratory of Digital Control and System Engineering (DCSELab), Ho Chi Minh City University of Technology (HCMUT), 268 Ly Thuong Kiet Street, District 10, Ho Chi Minh City 700000, Vietnam

[2] Faculty of Mechanical Engineering, Ho Chi Minh City University of Technology (HCMUT), 268 Ly Thuong Kiet, District 10, Ho Chi Minh City 700000, Vietnam

[3] Vietnam National University Ho Chi Minh City, Linh Trung Ward, Thu Duc District, Ho Chi Minh City 700000, Vietnam

[4] Faculty of Electronics and Telecommunication, Saigon University, Ho Chi Minh City 700000, Vietnam

[†] Leading - Corresponding author: dvtu@hcmut.edu.vn

[*] Presenting author: dang.ho753@hcmut.edu.vn

Abstract

Industrial firing test furnaces are gradually developed to evaluate the ability of insulation and integrity of elements of building construction in response to the ever-increasing demand for the experimentation of fire-resistant construction materials. Nonlinearity parameters of firing test furnaces cause the temperature and pressure control more complicated during the examination. Besides, these control variables are required to control accurately in accordance with the standardized temperature-time curve and the regulated pressure thresholds depending on the specimens to be experimented with. This article outlines an approach for manipulating furnace temperature and pressure via multiple PID controllers, each of which controls a zone according to the heating curve to maintain all control variables within the allowable ranges during combustion. Based on the assessment criteria in TCVN 9383:2012, experimental results when burning fireproof steel and wood doors validate the effectiveness of this control method.

Keywords: *PID controllers, Industrial furnace, Fire-resistance testing furnace, Temperature control, Segmental linearization*

1. Introduction

With several countries experiencing overpopulation, it is critical to address the issue of people's accommodation, particularly in large cities. Since then, the density of multi-story buildings has increased in response to this scenario, in tandem with the prevention and reduction of fatalities to the greatest extent possible whenever a fire occurs. One of the options is to install special doors that are fire-resistant and prevent smoke from entering to protect people's safety, give rescuers extra time to approach the fire, and prevent it from spreading to nearby locations. However, before being assembled, those doors must be thoroughly inspected, and the furnace is designed to accommodate this examination.

Electric resistance heating and gas heating (heat is produced by igniting an oxygen-gas mixture via gas-fired burners) are the two primary methods for regulating the temperature inside the furnace [1]. While the former is generally utilized in smelters, the latter is employed for boilers or fire testing [2]. Furthermore, when the capacity of the burners is adjusted, the temperature at the output changes accordingly, allowing them to track the predetermined temperature-time curve according to the standard.

Nevertheless, it can be clearly seen that temperature and pressure are two interdependent variables, thus controlling these parameters during the heating process is a complicated task. Besides, since this process contains nonlinear variables (thermal inertia, dead time), identification of the whole test furnace is challenging. As a result, a controller capable of self-identifying the system is necessary, thereby continuously adjusting the control parameters to regulate the temperature and pressure in the furnace. Some studies have applied PID controllers [3] to develop an algorithm for temperature control in the testing furnace, besides, the integration with other controllers [4]–[7] enhanced control quality and adaptability when uncertain factors are present. In addition, the outcomes of these papers are derived from computer-based simulation and system identification.

This paper describes a method to adjust the temperature and pressure inside the test furnace by combining multiple PID controllers. Each is responsible for controlling a zone of the heating curve, or in other words, linearizing the nonlinear system by using this method. The controller variables are determined through various experiments to obtain the most optimal set of parameters for the control process. This will also serve as the foundation for further development into a controller capable of self-updating parameters $\boldsymbol{K_p}$, $\boldsymbol{K_i}$, and $\boldsymbol{K_d}$ prior to the unexpected appearance of nonlinear or unidentified factors.

2. System Description

The fire resistance testing furnace, depicted in Fig.1, has internal dimensions of $\boldsymbol{3.0m \times 1.0m \times 0.5\,m}$, respectively (convection section). The furnace's wall structure is separated into three layers: the innermost is a fire-proof brick, the next is ceramic insulation, and the outside is covered by a high-temperature resistance steel frame.

The furnace is heated by a total of six gas-fired burners (1) which are alternately positioned on both sides of it and have a capacity ranging from 40 to 370 $\boldsymbol{kW}$ each. Its capacity is modified by adjusting the position of the mechanical cam through a programmable logic controller, which changes the flow of gas and oxygen into the burner's combustion chamber. The burners cooperate to regulate the temperature and pressure inside the furnace in accordance with the standard heating curve and the required pressure thresholds, depending on the test specimen (2). To avoid damage from high temperatures, the burners that are not responsible for heating the furnace will be controlled to

blow air only. Furthermore, the furnace is equipped with a blower (3) connected to the chimney system (4) at the furnace's back, which not only helps adjust the pressure during burning but also helps cool the furnace at the end of the combustion process.

Concerning the inner temperature sensor, the furnace is equipped with six K-type thermocouples (with measurement thresholds ranging from -270 to 1370 degrees Celsius [EN 60584-1:1995] (5) that are positioned on both sides of the furnace as well as avoid direct contact with the burner's flame. Additionally, the sensor is located $\mathbf{100 \pm 50}\,\boldsymbol{mm}$ away from the test specimen's fire-exposed surface [ISO 834-1:1999]. The pressure sensor, specifically the differential pressure sensor (which measures the pressure difference between ambient and inner furnace pressure), is situated at the neutral pressure plane, or in other words, at a height of 500mm above the notional floor level.

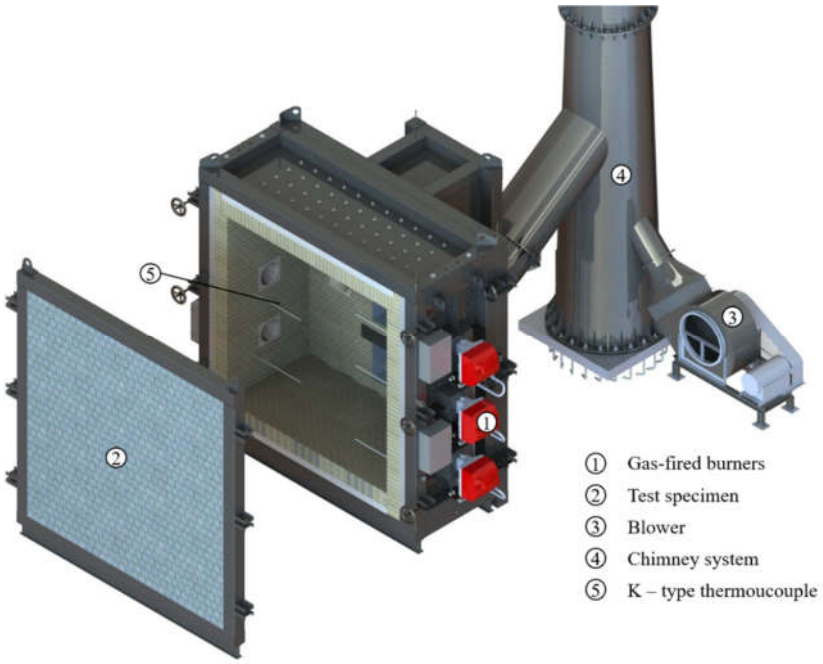

Figure 1. Overall furnace system

3. Design and Experiment

3.1. Summary of temperature and pressure criteria during testing

The Vietnamese Standard TCVN 9311 - 1:2022 [8], TCVN 9383:2012 [9] and outlines the following core requirements for the temperature inside the furnace as well as the differential pressure between ambient and the convection session during the experiment, specifically:

The temperature inside the furnace follows the standard heating curve, which is represented by the equation below:

$$T = 345 \log_{10}(8t + 1) + 20 \qquad (1)$$

where T denotes the reference temperature in the furnace at time t, degrees Celsius;

t denotes the testing time, minute;

The tolerance of the inner furnace temperature is given by these equations:

1. $d_e \leq 15\%$ for $5 < t \leq 10$

2. $d_e \leq 15 - 0{,}5(t - 100)\%$ for $10 < t \leq 30$
3. $d_e \leq 5 - 0{,}083(t - 30)\%$ for $30 < t \leq 60$
4. $d_e \leq 2{,}5\%$ for $t > 60$

$$d_e = \frac{A - A_s}{A_s}$$

where d_e denotes the percent deviation;

A is the area under the actual average heating curve of the test furnace;

A_s is the area under the standard heating curve;

t is the time, minute;

However, the standard also provides an additional error assessment method to simplify the process of heating the furnace for experimentation which is that the actual temperature should not exceed $\pm\mathbf{100}$ degrees Celcius relative to the reference one. The graph in **Fig. 2** illustrates the inner furnace temperature during the testing, together with the upper and lower error limits to help assess the controller's quality.

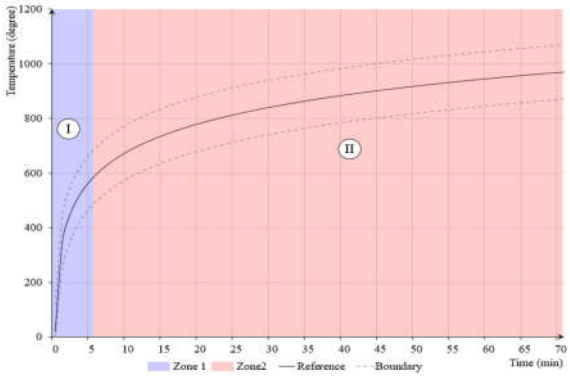

Figure 2. Standard temperature-time curve

For the differential pressure, after 10 minutes from the time that the furnace begins to heat, the actual value sampled by the sensor does not exceed ± 3 Pascal.

Before conducting the inspection, there are also some more prerequisites specified in the standard in order to guarantee the validity of the test results, such as:

- The inner furnace temperature before the inspection process should not exceed 50 degrees Celsius.
- Ambient temperature reaches 20 ± 10 degrees Celcius.

3.2. Determining the experimental process's parameters

Temperature

As described above, with a model with many influencing factors, the high latency makes the theoretical identification of the system's characteristics not guaranteed to be accurate when implemented real system test. Therefore, the temperature controller is preliminarily designed based on the requirements of the heat curve, and testing and parameter correction is performed on the real system.

Stage 1: Start-up is represented by the blue region (Zone I) of the graph in **Fig. 2**. from the start of heating to 5 minutes. The furnace is currently being heated, initially at room temperature. Bricks must have time to absorb the heat. The rate of heating is rapid, reaching 5 degrees Celcius per second.

Stage 2: Maintenance is represented by the red region (Zone II) of the graph in **Fig. 2** from 5 minutes onwards. At this stage, the temperature in the furnace has gradually approached a steady state, the brick has completely absorbed heat. The rate of heat increase in this stage is lower than in the previous stage, reaching 0,4 degrees Celcius per second. The temperature error mustn't exceed 15% in 5 to 10 minutes and does not exceed 5% after 10 minutes.

Therefore, the paper proposes to use two PID controllers for the **Start-up** stage and the next **Maintenance** stage.

Controller design

The output power $\boldsymbol{P(t)}$ of each burner depends on the temperature error $\boldsymbol{e(t)}$ between the actual temperature and the reference temperature according to the PID controller by the equation:

$$P(k) = P(t-1) + K_p e(t) + K_i(e(t) + e(t-1))\Delta t + K_d \frac{e(t) - e(t-1)}{\Delta t} \quad (2)$$

where $\boldsymbol{P(t)}$ and $\boldsymbol{P(t-1)}$ are burner power at current and previous time:

$\boldsymbol{e(t)}$ and $\boldsymbol{e(t-1)}$ are the error between the actual and the reference temperature at the above two times; $\boldsymbol{K_p, K_i, K_d}$ are the parameters of the PID controller; $\boldsymbol{\Delta t}$ is the sampling time.

The parameters K_p, K_i, K_d are selected according to the following method of ascending K_p until the temperature follows the standard curve. In case the scaler *P* does not meet the requirements completely but in some parts the error is larger than the requirement of the standard, the integrator *I* and the differential unit *D* will be added to improve the control quality.

Stage 1: In the first 5 minutes, by gradually increasing K_{p1}, we get the temperature error result after 5 minutes.

Table 1. The error corresponds to each K_{p1} at the first 5 minutes

Case	Value	Error(%)	Boundary conditions
1	$K_{p1} = 0.8$	4,67	Outside
2	$K_{p1} = 1$	2,89	Inside
3	$K_{p1} = 1.2$	4.18	Outside

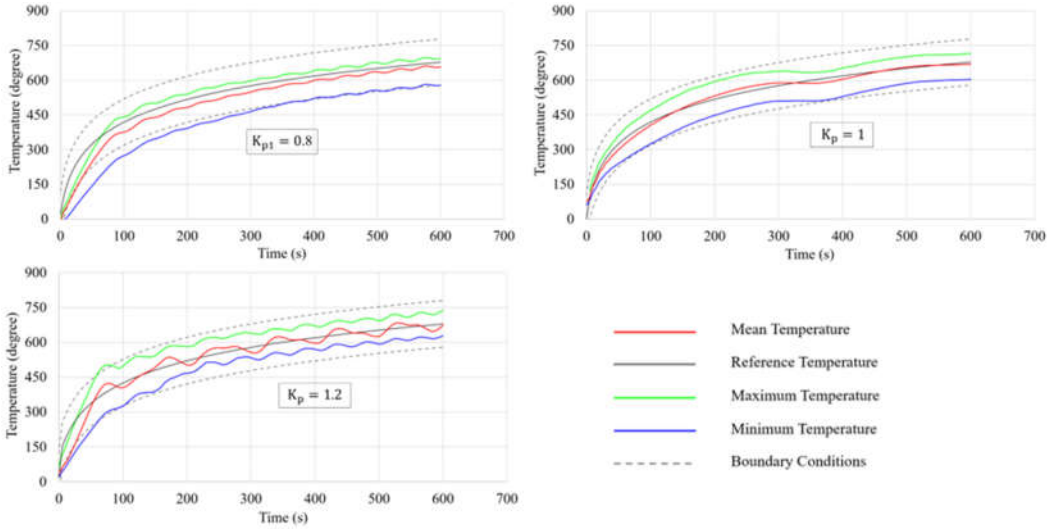

Figure 3. Graph of temperature over time with $K_p = 0.8;\ K_p = 1;\ K_p = 1.2$

At $\boldsymbol{K_p = 1}$, stability condition error of less than $\mathbf{15\%}$ after the first 5 minutes and condition all sensors are within $\pm\mathbf{100}$ degrees Celcius is qualified.

Step 2: Do the same to get the following result.

Table 2. The error corresponds to each K_{p2} after the first 5 minutes

Case	Specification	Error (%)	Boundary conditions
1	$K_{p2} = 0.4$	3.27%	Inside
2	$K_{p2} = 0.5$	2.89%	Inside
3	$K_{p2} = 0.6$	3.94%	Inside

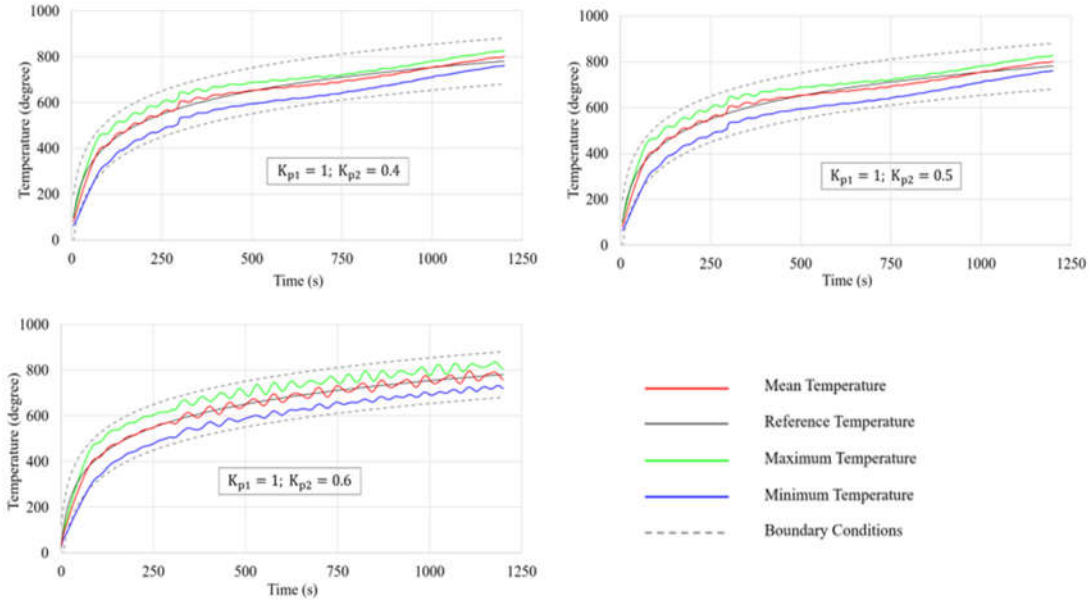

Figure 4. Graph of temperature and error between the actual temperature and reference temperature over time when using only two stages of ***P***

The results show that $\boldsymbol{K_{p2} = 0,5}$ has the smallest error. Although the actual temperature line follows the reference temperature line, the error does not guarantee the temperature tolerance stated in TCVN 9311-1:2012.

The cause of the error is due to the level of inertia when changing the burner power, the temperature in the furnace does not respond immediately, but it needs a fixed time. Therefore, we need to add a *D* link to the current controller to reduce the inertia of the model.

$$P(t) = P(t-1) + K_p e(t) + K_d \frac{e(t) - e(t-1)}{\Delta t} \quad (3)$$

We also gradually increase the value of K_d until the system reaches the required error. Do the same to get the result $K_{d2} = 0.07$. The error after 10 minutes reached 0,5%.

The results obtained when testing with early-stage P controllers and PD controllers are according to the chart below.

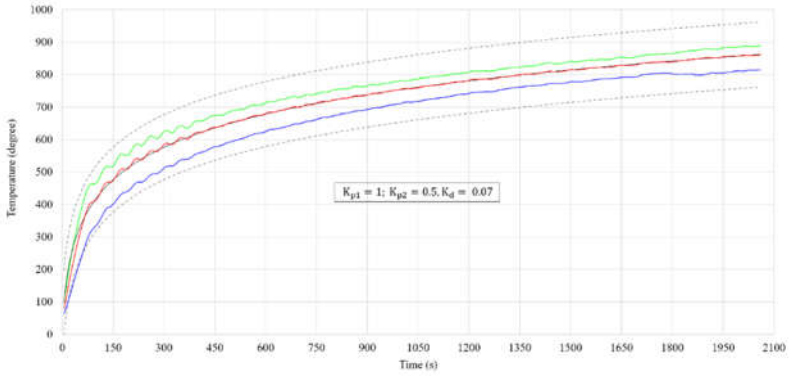

Figure 5. Graph of temperature and error between the actual temperature and reference temperature over time when using both *P* and *D*

Differential Pressure

Based on the priority level, after the furnace temperature requirements are met, verify the pressure inside and outside the furnace at the pressure neutral plane with the PD controller achieved.

In case the pressure exceeds the threshold of 90% of the allowable pressure error, adjust the pressure by controlling the fan to blow air in or suck the air out of the furnace. Specifically, if the error is close to -3 Pascal, the fan is controlled to rot the incoming air, conversely, when the error is close to $+3$ Pascal, the fan is controlled to suck the air out of the furnace.

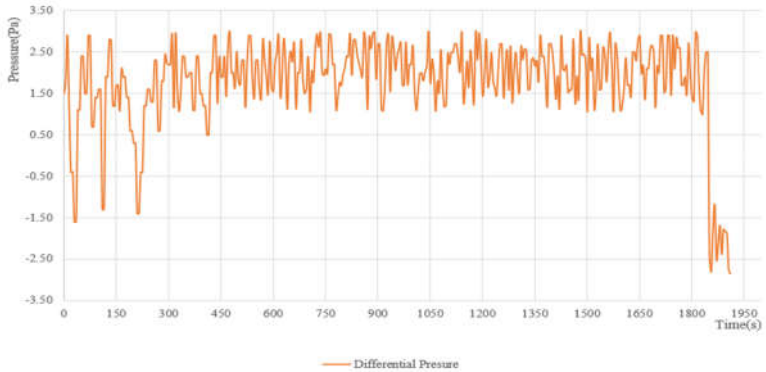

Figure 6. The graph of the pressure difference inside and outside the furnace at the pressure balance plane

4. Conclusion

This paper presents a method to regulate the temperature and pressure inside the furnace using multiple PID controllers during the testing. The experimental process used to estimate the parameters in the controller, as well as the results obtained from those experiments, demonstrate the efficiency of this approach. This is also the foundation for developing PID controllers capable of self-updating control parameters to adapt to the system when non-linear or undesirable factors interfere, thereby enhancing quality control.

Acknowledgments

This research is funded by Vietnam National University Ho Chi Minh City (VNU-HCM) under grant number TX2023-20b-01. We acknowledge the support of time and facilities from National Key Laboratory of Digital Control and System Engineering (DCSELab), Ho Chi Minh City University of Technology (HCMUT), VNUHCM for this study.

References

1. Huy Hung Nguyen, Chi Tuan Duong, Hoang Long Phan, Van Tu Duong, and Tan Tien Nguyen, "Model Identification of Gas-Fired Industrial Furnace", the 7th International Conference on Advanced Engineering – Theory and Applications, 2022.
2. G. Geng and G. M. Geary, "On Performance and Tuning of PID Controllers in HVAC Systems", in *Second IEEE Conference on Control Applications*, 1993.
3. A. Yoneya, T. Kondo, Y. Hashimoto, and Y. Togari, "Two-Valued PID Controller", 1998.
4. E. O'Rear, D. Webb, J. Kneifel, and C. O'Fallon, "Gas vs Electric: Heating System Fuel Source Implications on Low-Energy Single-Family Dwelling Sustainability Performance", *Journal of Building Engineering*, vol. 25, Sep. 2019, doi: 10.1016/j.jobe.2019.100779.
5. Y. Xie, F. Gan, and B. Liu, "Design and application of TS-PID controller in fire furnace", in *6th International Conference on Fuzzy Systems and Knowledge Discovery, FSKD 2009*, 2009, vol. 6, pp. 516–519. doi: 10.1109/FSKD.2009.689.
6. E. Grassi and K. Tsakalis, "PID Controller Tuning by Frequency Loop-Shaping: Application to Diffusion Furnace Temperature Control", 2000.
7. A. A. Vodat and I. D. Landau, "A Method for the Auto-calibration of PID Controllers", *Elsevier Science*, vol. 31, no. 1, pp. 41–53, 1995.
8. TCVN 9311-1:2012 and ISO 834-1:1999, "*Fire resistance test-Building construction elements*", Vietnam National Standard, 2012.
9. TCVN 9383:2012, "*Fire resistance test-Fire door and Shutter Assemblies"*, Vietnam National Standard, 2007.

[O-1-7] Development of Rubber Wheel Track Slip Resistance Tester on Photovoltaic Panel

Anh Duy Hoang Ngoc[1, *], Cong Toai Truong[1, 2, 3], Minh Tri Nguyen[1], Van Tu Duong[1, 2, 3], Huy Hung Nguyen[4], Tan Tien Nguyen[1, 2, 3, †]

[1] National Key Laboratory of Digital Control and System Engineering (DCSELab), Ho Chi Minh City University of Technology (HCMUT), 268 Ly Thuong Kiet Street, District 10, Ho Chi Minh City 700000, Vietnam

[2] Faculty of Mechanical Engineering, Ho Chi Minh City University of Technology (HCMUT), 268 Ly Thuong Kiet, District 10, Ho Chi Minh City 700000, Vietnam

[3] Vietnam National University Ho Chi Minh City, Linh Trung Ward, Thu Duc District, Ho Chi Minh City 700000, Vietnam

[4] Faculty of Electronics and Telecommunication, Saigon University, Ho Chi Minh City 700000, Vietnam

[†] Leading - Corresponding author: nttien@hcmut.edu.vn.

[*] Presenting author: duy.hoang261201@hcmut.edu.vn

Abstract

Due to its potential to increase photovoltaic efficiency by up to 30%, the utilization of mobile cleaning robots to clean photovoltaic panels is growing in popularity, especially for many energy production companies. These mobile cleaning robots are more flexible than other varieties thanks to the equipment of two rubber wheel tracks, enabling freely moving on photovoltaic panels. However, the surfaces of photovoltaic panels feature high-temperature, high slope, and condensate steam that reduces the slip resistance of the rubber wheel tracks. This can be overcome by proposing the shape pattern and materials of wheel tracks. Consequently, it is essential to achieve a testing device that stimulates the harsh working condition of the photovoltaic panels to evaluate the slip resistance of the proposed wheel tracks. This paper describes the structure of a testing device for validating slip resistance. The proposed testing device is able to control the wetness of the moving surface and the inclination of the photovoltaic panel. The experimental result of the proposed testing device can be served for extrapolation of the slip resistance of the mobile cleaning robot equipped with the validated wheel tracks.

Keywords: *Wet condition, Inclined surface, Tilt angle, Slip-resistance, Photovoltaics panel*

1. Introduction

During the decades of the last two centuries there have been many cases of accidents involving the word "slip" [1]–[8], which appears in almost all aspects of human life. "Slip" occurs in the lubrication of mechanical machines to increase the efficiency and life of machine parts; "slip" also occurs when the surface of the shoe does not guarantee adhesion [9]–[13] on wet and inclined surfaces [5]–[7], etc. wherever there is contact between two surfaces, it has both pros and cons. It is evaluated through the static friction parameter, which is described that if the pulling force is greater than the maximum static friction force between the two contacting surfaces, this changes the static state to sliding or rolling [14]–[15]. Moreover, it is very difficult to determine an exact value by calculation, because it is affected by many factors and they must take into account the microscopic properties of the material. Differences in temperature, roughness of the surface, contact area, wet or dry conditions, etc. are typical influencing factors and difficult to control. Therefore, many standards developed to evaluate slip or ensure slip resistance use experimental methods, and each standard has its unique assessment criteria and circumstances, but they all have the same purpose of precisely and asymptotically evaluating slip resistance. Specifically, rubber, this is an organic material and it is difficult to control its properties in daily life. It is modified by humans for many different purposes; a block of synthetic rubber moving on a smooth, inclined and wet ceramic surface like PV panel is a problem that needs to be considered because it is really practical and helpful. The purpose of this research is to present a system capable of controlling working conditions (inclination angle, wetness), applied to the particular case between the synthetic rubber and the solar panel surface, from there the requirement to limit the tilt angle at a specified wettability with synthetic to achieve slip resistance standard on the solar panel surface.

2. System Description

The system is designed with the ability to adjust the inclination and the wetness of the surface through controlling the flow of water sprayed on the plane. Based on those requirements, the system is designed to include four parts with different functions:

- Pair of test subjects (1)
- Wetness controller (2)
- Slip detector (3)
- Angle adjustable part (4)

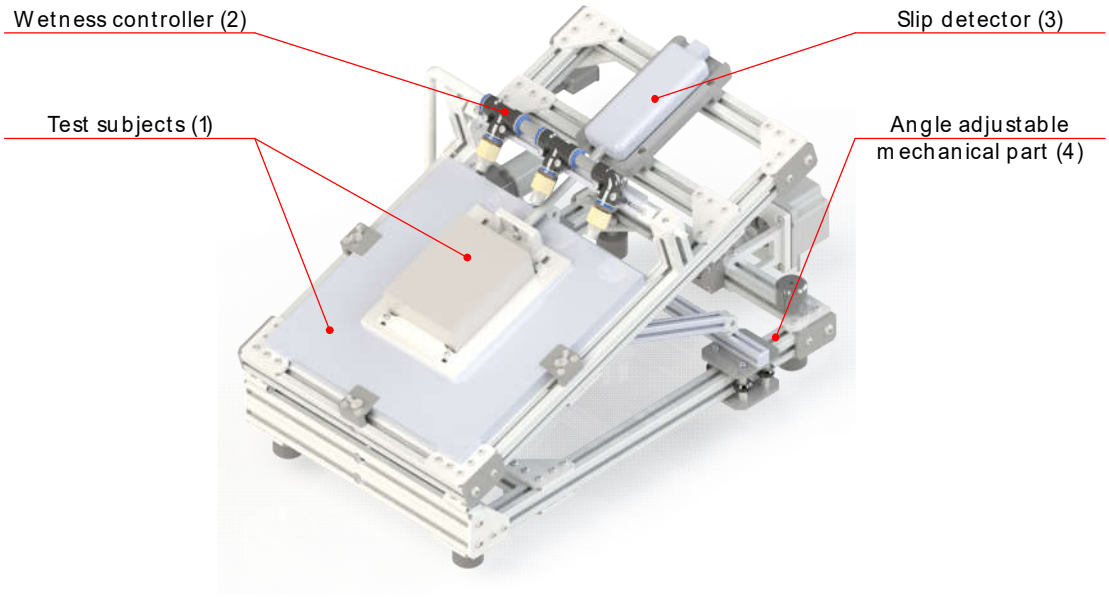

Figure 1. 3D design of the slip resistance tester

Fig. 1 shows the 3D design of the slip resistance tester. The mechanical structure, the system is the connection between the slotted aluminum rails by hard plastic sheets with a thickness of up to 5mm, thereby ensuring the straightness, perpendicularity, the reciprocating movement and sliding of casters are easier. The ability to change the tilt angle of inclination is due to the fact that it is equipped with a hinge joint and set of rollers to convert reciprocating motion into rotation. It is all driven by a screw mechanism through a stepper motor thereby ensuring the accuracy and furthermore the self-locking of this actuator. The accuracy is checked through the tilt angle sensor, flow sensor and booster pump. In case the drive motor makes the distance between the casters and the edge of the part (4) too close to the permissible limit, in order to avoid destruction or damage to the motor, the system is equipped with a metal sensor at the permissible distance of 4mm.

Table 1. General parameters of the slip resistance tester

Parameter	Unit	Value
Overall size	mm	$660 \times 410 \times 158mm \div 660 \times 410 \times 590mm$
Mass	kg	22
Testing region	mm^2	$353.5 \times 387.5mm$
Tilt angle range	°	$0 \div 45$

The slip resistance tester is designed as **Fig. 1** and the parameter of this includes overall size, mass, testing region, tilt angle range, and flow range. All ranges of those parameters are shown in **Table 1**.

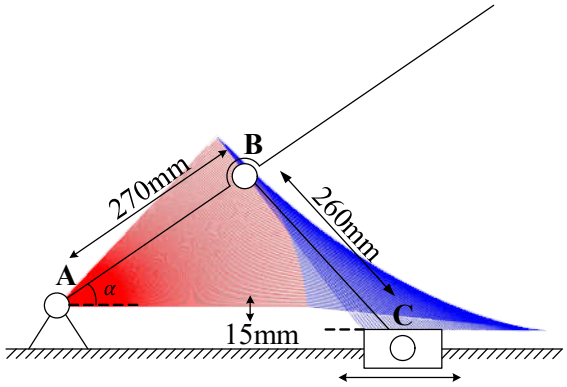

Figure 2. Kinematic diagram and operating simulation of the slip resistance tester

Fig. 2 shows the simulation operating range of the slip resistance tester. The parameters of link AB and BC are determined respectively to be **270mm and 260mm**. Point C is the position associated with the movement of the screw mechanism. If point C changes, the line segment AB will be moved up or down which makes the tilted angle ($\boldsymbol{\alpha}$) change in range $\mathbf{0}^{\circ} - \mathbf{45}^{\circ}$. This result will be used for setting up test scenarios to research the relationship between position point C and the tilted angle.

Table 2. General parameters of the slip resistance tester

Component	Type	Detail
Stepper motor	Hybrid	200 pulses, micro-step 1.8 degrees
Screw step	mm/round	5mm
Tilt angle sensor	GY-521 6DOF IMU MPU6050	Gyroscopes +/- 250 500 1000 2000 degree/sec, accuracy ~0%
Flow sensor	Range 1 ÷ 30 l/m	Accuracy 90%
Metal detection sensor	PNP NO	4mm, hysteresis 10% sensing distance

Each position of point C (x_C) corresponds to the value of a specified tilt angle alpha (α); the relationship follows the equation below:

$$270\cos(\alpha) + \sqrt{260^2 - (270\sin(\alpha) + 15)^2} = x_C \quad (1)$$

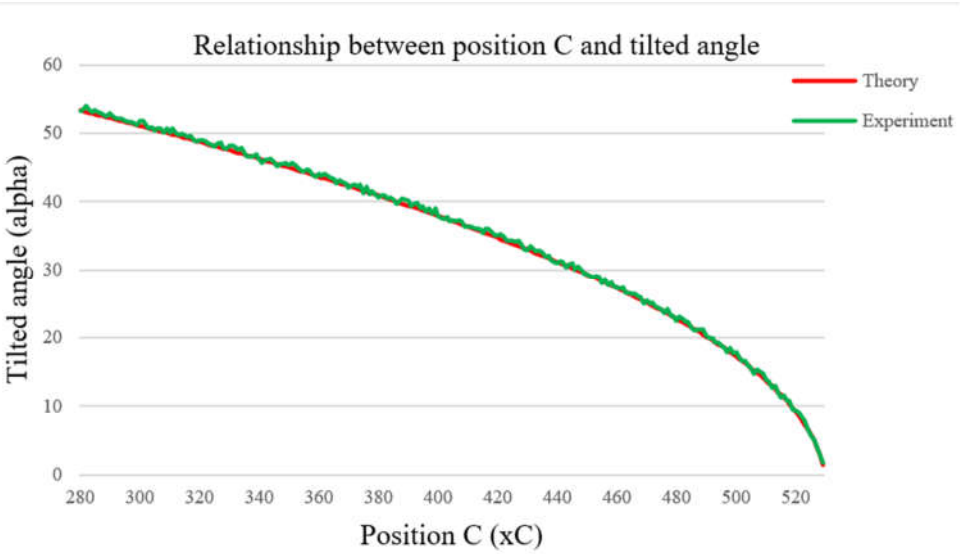

Figure 3. Relationship between position C (x_C) and tilted angle (α)

With data collected in the experiment and shown in **Fig. 3**, the similarity between the two graphs above, proves the reliable accuracy of the system, with a maximum error of about 5%.

The whole system works on the following principle: thanks to the drive of the stepper motor, the linear rotation of the screw and roller steps helps the whole system change the tilted angle. Besides, the tilt angle and flow values are sent to the computer for next step processing thanks to the sensors. When a slip occurs, the device detects the slip and sends data to the computer. The system can be used on many different surfaces.

3. Design and Experiment

The first experiments using this system were conducted with the tempered glass surface of the solar panel and a heavy block placed on the surface of a synthetic with variable Shore hardness. From this, a limit on the tilt angle can be moved for a given block of rubber at a given wetness.

Table 3. General conditions of the experiments

Parameter	Unit	Value
Screw adjustment step	mm	0.5
Heavy block	kg	1
Flow adjustment step	l/min	0.5
Shore hardness	Shore A	A35, A40, A70

Table 3 shows the conditions of the experiment. In which the rubber samples selected for the experiment are shore A, there are 3 hardness values representing the test as A35, A40, and A70.

Table 4. Conditions and results of maximum tilted angle when testing the relationship between shore hardness and flow

Flow	Shore A35	Shore A40	Shore A70
0 l/min	28.90°	26.50°	14.70°
1 l/min	21.08°	19.77°	11.34°
1.5 l/min	19.84°	18.33°	10.30°
2 l/min	18.80°	17.40°	9.54°
3 l/min	16.90°	16.33°	8.96°
4 l/min	16.27°	15.80°	8.33°

Table 4 shows the maximum tilt angle results to avoid slip with different flow rates. As the above results, in the same value of shore A, if the flow rate is higher, the angle will be lower. As for the same value of flow rate, if the hardness trends are higher, the title angle maximum will be smaller (for example shore A35 at 0ml/min is 28.90° and Shore A70 is 14.70°).

Table 5. Required range of tilted angle for each case of shore hardness and corresponding flow

Shore	Flow range	Recommended tilted angle
Shore A35	$1 \div 4\ l/min$	$< 16°$
Shore A40		$< 15°$
Shore A70		$< 8°$

After the experiment, the results are shown in **Table 5**. This study gives some recommendations for rubber shore A with different hardness. With the same flow range of **1-4l/min**, shore A35 should work with a tilted angle below 16º, shore A40 below 15º, and shore A70 below 8º to avoid slipping. Thus, with the same flow range conditions, if the hardness value of shore A is higher, the slipping tendency will be greater, so the tilt angle working should be noted to choose the suitable type of shore A.

4. Conclusion

The paper presents a design that can be used to test the slip resistance of a specified material on a specified surface at a specified wetness. Besides being able to accurately check the working conditions in terms of tilt angle and wetness with the maximum error of about 5%, it is also possible to recognize the slip when it occurs to the test object. Moreover, another success of the paper was to give a report on the maximum tilted angle requirement when using synthetic rubber that moves on wet inclined PV panel surfaces and can apply the results to the solar panel cleaning robot industry.

Acknowledgements

This research is funded by Vietnam National University Ho Chi Minh City (VNU-HCM) under grant number TX2023-20b-01. We acknowledge the support of time and facilities from National Key Laboratory of Digital

Control and System Engineering (DCSELab), Ho Chi Minh City University of Technology (HCMUT), VNU-HCM for this study.

References

1. M. Olabarria *et al.*, "Head-on crashes on two-way interurban roads: A public health concern in road safety", *Gac. Sanit.*, vol. 29, pp. 16–23, 2015, doi: 10.1016/j.gaceta.2015.03.007.
2. X. Wang, H. Yu, C. Nie, Y. Zhou, H. Wang, and X. Shi, "Road traffic injuries in China from 2007 to 2016: The epidemiological characteristics, trends and influencing factors", *PeerJ*, vol. 2019, no. 8, pp. 1–14, 2019, doi: 10.7717/peerj.7423.
3. S. Feng, Z. Li, Y. Ci, and G. Zhang, "Risk factors affecting fatal bus accident severity: Their impact on different types of bus drivers," *Accid. Anal. Prev.*, vol. 86, pp. 29–39, 2016, doi: 10.1016/j.aap.2015.09.025.
4. M. Hippi and S. Hartonen, "Statistical data of slipping injuries happened in the winter time", *Sirwec*, no. May, pp. 1–6, 2012.
5. L. Strandberg, "On accident analysis and slip-resistance measurement," *Ergonomics*, vol. 26, no. 1, pp. 11–32, 1983, doi: 10.1080/00140138308963309.
6. U. S. Department of Labors, "National Census of Fatal Occupational Injuries Summary", *Bur. Labour Stat.*, vol. December, no. USDL-21-2145, p. 11, 2021.
7. D. P. Manning, "Deaths and injuries caused by slipping, tripping and falling", *Ergonomics*, vol. 26, no. 1, pp. 3–9, 1983, doi: 10.1080/00140138308963308.
8. N. Amarasingha and S. Dissanayake, "Factors associated with rural run-off-road and urban run-offroad crashes: a study in the United States," no. December, pp. 168–177, 2014, doi: 10.31705/apte.2014.14.
9. D. Demydov and D. Ph, "Progress Report (2nd quarter) Advanced Lubrication for Energy Efficiency, Durability and Lower Maintenance Costs of Advanced Naval Components and Systems Prepared for Office of Naval Research Submitted by", no. August, 2010.
10. K. S. Vario, "We have a system for effective lubrication. Klübermatic lubricant dispensers. The right lubricant at the right point at the right time."
11. M. Johnson, "Energy effi ciency through precision lubrication."
12. N. M. Aljamali, W. Hashim, Y. Almuhana, and H. A. Hussein, "Review on Effect of Machine oils on the Efficiency of Operating Thermal Machines", no. October, 2021.
13. T. LUBRIFIANTS, "Lubrication solutions for industrial applications," pp. 0–41, 2016.
14. C. E. Mungan, "Rolling friction on a wheeled laboratory cart", *Phys. Educ.*, vol. 47, no. 3, pp. 288–292, 2012, doi: 10.1088/0031-9120/47/3/288.
15. R. Grönqvist, "Mechanisms of friction and assessment of slip resistance of new and used footwear soles on contaminated floors", *Ergonomics*, vol. 38, no. 2, pp. 224–241, 1995, doi: 10.1080/00140139508925100.

[O-1-8] Evaluation of Parameter Effect on Swimming Trajectory of Elongated Undulating Fin Using Computational Fluid Dynamic Model

Quoc Tuan Vu[1, *], Huynh Nguyen Phong[1], Quang Dat Trinh[1], Van Tu Duong[1, 2, 3], Huy Hung Nguyen[4] and Tan Tien Nguyen[1, 2, 3, †]

[1] National Key Laboratory of Digital Control and System Engineering (DCSELab), Ho Chi Minh City University of Technology (HCMUT), 268 Ly Thuong Kiet Street, District 10, Ho Chi Minh City, Vietnam
[2] Faculty of Mechanical Engineering, Ho Chi Minh City University of Technology (HCMUT), 268 Ly Thuong Kiet, District 10, Ho Chi Minh City, Vietnam
[3] Vietnam National University Ho Chi Minh City, Linh Trung Ward, Thu Duc District, Ho Chi Minh City, Vietnam
[4] Faculty of Electronics and Telecommunication, Saigon University, Vietnam

[†] Leading - Corresponding author: nttien@hcmut.edu.vn
[*] Presenting author: vuqquoctuan.sdh20@hcmut.edu.vn

Abstract

Due to great efficiency, outstanding mobility, and stealth bio-propulsion, fish robots have been extensively recognized for decades as a potential vehicle for underwater research. However, the swimming efficiency of contemporary fish robots is still quite far compared to those of alive fish. One of the challenges of the development of swimming control is to obtain well-suited control parameters. In this paper, we provided three contributions: 1) to calculate parameters and control fin-rays moving in a fixed gait; 2) to simulate the swimming trajectory of fin-rays in CFD environment; and 3) to evaluate the effect of changes in environmental parameters on its moving orbit. The simulation results offer an important insight into the impact of factors on the robotic fish model and then give the best solution in designing and testing the real model.

Keywords: *Computational fluid dynamics, Dynamic mesh, Robotic fish, Undulating fin*

1. Introduction

Underwater missions, such as ocean exploration, search and rescue, and the inspection of coastal structures, require the use of autonomous underwater vehicles (AUVs) [1-4]. Traditionally, these vehicles are powered by water pumps, air-jet engines, or a single propeller, with additional actuators providing maneuverability. However, these propulsion systems have limitations when performing tasks in complex environments, such as the presence of ocean disturbances.

Inspired by the efficient and stable movements of underwater creatures like stingrays, knife fish, and cuttlefish, scientists have developed robot fishes with biomimetic fin propulsion systems [5-8]. These robots that employ undulating fin propulsion have great potential thanks to their advantages, including the ability to perform complex maneuvers with minimal disturbance to the surrounding water flow.

Recent years have seen the development of many bionic underwater vehicles with undulating fins, and researchers are studying various problems related to their kinematics modeling, mechanical design, implementation, and experimentation [9-12]. To optimize their design, it is essential to pre-evaluate the fin motion and investigate the impact of design parameters and environmental factors on robot fish movement.

This paper uses Computational Fluid Dynamics (CFD) simulations to analyze the hydrodynamics of the continuous undulating fin. The computational model simulates the motion of the undulating bionic fin under certain pre-set conditions.

2. Computational Simulation Method

The fluid flow plays an important role in flow problems of the airflow around aircraft, through civil constructions, the water flow of irrigation structures, around the hull of a ship, etc. Forasmuch as, by capturing the flow properties, and the variation of the fluid properties, the engineer is able to calculate, design the product, and optimize the material with durable quality and high performance. Fluid Dynamics (CFD) method is a promising tool for the swimming gait simulation of robotic fish due to better evaluation, calculation, and analysis of complex flows, and physical parameters [13]. CFD simulation methods are divided into two main methods: the meshing method and the particle method [14].

The simulation process of CFD includes steps: geometry creation, geometry processing, meshing, parameter settings, solution settings, simulation implementation, convergence check, and result processing as illustrated in Figure 1.

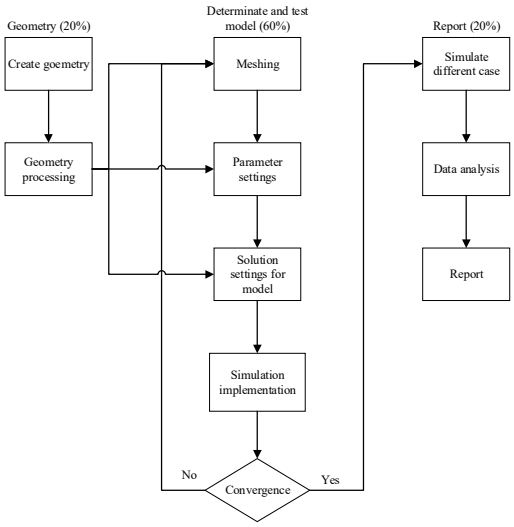

Figure 1. The simulation process of CFD

In the implementation steps, the geometry can be created with CAD software such as Solidworks, NX, Inventor, and Catia to create 3D models for the purpose of designing. After that, ANSYS software is used to perform simulations. When simulating non-moving objects, the simulation will be less complicated. For the simulation of a moving object, program C is used to generate the UDF code.

In order to analyze the motion of the elongated fin propulsion system, it is important to have a well-sized mesh for the computational analysis. The mesh size must be small enough to accurately capture the hydrodynamics, but also large enough to be computationally feasible. All of the forces acting on the propulsive element are assumed to be generated by its motion in the fluid, due to the high Reynolds number.

The fin design parameters used in the computational study are as follows:

Table 1. Fin geometric parameters

Amplitude (mm)	Fin length (mm)	Wavelength (mm)	Frequency (Hz)	Motion speed (m/s)
60	900	450	2	0.53

The mesh zone is divided into two parts: The first part is the main calculation area of the fin bounded by a circle with a diameter of 1500mm, originating at the position of the fin head (center of the circle). The meshing size is chosen by 0.01 square mm. The second part is the water area; the purpose is to create a wider net area for the fins to move represented by a rectangle 3x7 m; the origin is set at 1.5m from the right edge and the lower edge 1.5m. The meshing size is chosen by 0.035 square mm. Figure 2 illustrates the mesh zone of the computational simulation.

To define fin motion, the dynamic mesh function and the user-defined function (UDF) illustrating sine wave movement are pre-defined and imported into Ansys-Fluent.

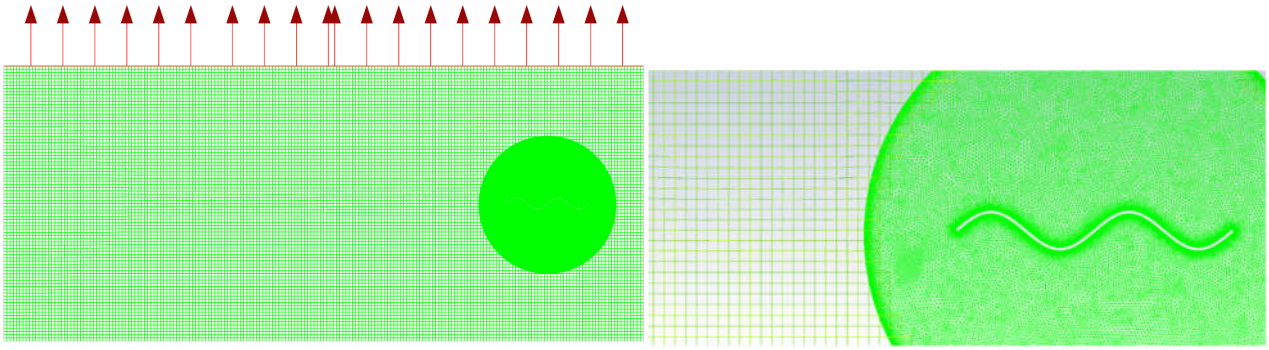

Figure 2. Mesh model of the undulating fin movement

3. Simulation Results and Discussion

During fin oscillation up and down, negative force (same direction of motion – thrust) when the fin oscillates from position "0" to position "-1" or "1", positive force (opposite of motion – drag/resistance) when the fin moves from "1" or "-1" to "0" as shown in Figure 3.

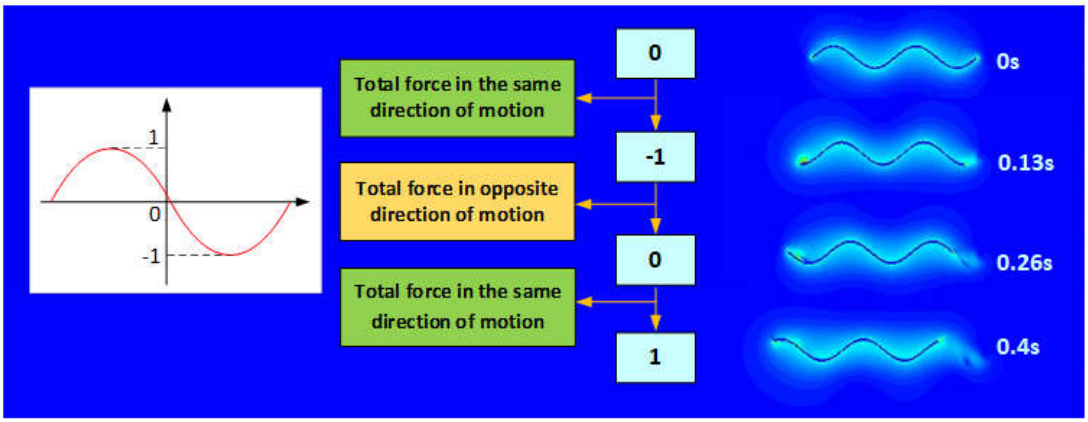

Figure 3. Force generated along the fin during movement

The graph of the total thrust of the fins during motion is shown in Figure 4.

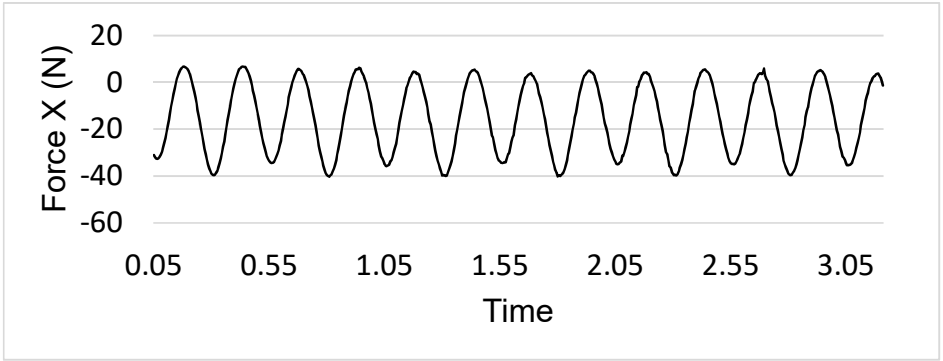

Figure 4. Force generated along the fin during movement

While the force is negative, the fin pushes to surrounding water to help the fins move forward because, in the simulation, the direction of the fin's movement is negative.

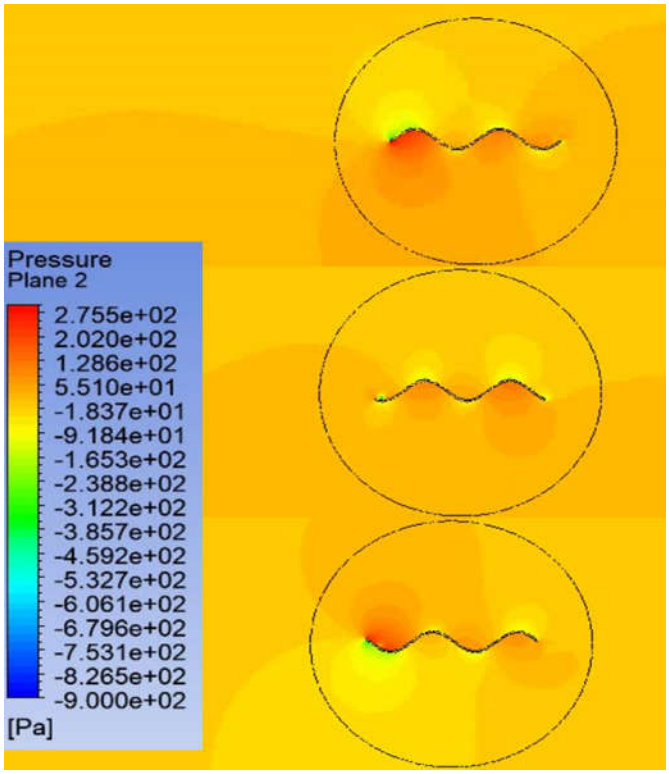

Figure 5. Distribution of pressure during fin movement

As can be seen in Figure 5, the high pressure is recorded on the concave side and low on the convex part of the fin.

4. Conclusion

In this study, the motion of the elongated undulating fin was analyzed by employing 2D CFD simulations. By obtaining the force generated and pressure distribution during the movement of the fin, the explanation of fin motion is given. The obtained results and discussion in this paper would have potential notices for a continuous undulating fin design of the robot fishes and other underwater biomimetic vehicles.

Acknowledgment

This research is funded by Vietnam National University Ho Chi Minh City (VNU-HCM) under grant number TX2023-20b-01. We acknowledge the support of time and facilities from National Key Laboratory of Digital Control and System Engineering (DCSELab), Ho Chi Minh City University of Technology (HCMUT), VNU-HCM for this study.

References

1. N. Council, D. Studies, O. Board, and C. Seas, Exploration of the Seas: Voyage Into the Unknown. Washington, DC, USA: Nat. Acad. Press, 2003.
2. R. B. Wynn et al., “Autonomous underwater vehicles (AUVs): Their past, present and future contributions to the advancement of marine geoscience”, Marine Geol., vol. 352, pp. 451–468, Jun. 2014.

3. J. Wang, W. Gu, J. Zhu, and J. Zhang, "An unmanned surface vehicle for multi-mission applications", in Proc. Int. Conf. Electron. Comput. Technol, pp. 358–361, Feb. 2009.
4. J. Yuh, "Design and control of autonomous underwater robots: A survey," Auton. Robots, vol. 8, no. 1, pp. 7–24, 2000.
5. Y. Yang, Y. Xia, F. Qin, M. Xu, W. Li, and S. Zhang, "Development of a bio-inspired transformable robotic fin", Bioinspiration Biomimetics, vol. 11, no. 5, 2016, Art. no. 056010.
6. Zhou, C., Low, K. H., "Design and Locomotion Control of a Biomimetic Underwater Vehicle With Fin Propulsion", IEEE/ASME Transactions on Mechatronics, vol. 17(1), pp. 25-35, 2011.
7. Low, K. H., & Junzhi, Y.: Development of Modular and Reconfigurable Biomimetic Robotic Fish with Undulating Fins. Proceedings of the 2007 IEEE International Conference on Robotics and Biomimetics, 2007.
8. Hu, T., Shen, L., Lin, L., & Xu, H.: Biological inspirations, kinematics modeling, mechanism design and experiments on an undulating robotic fin inspired by Gymnarchus niloticus. Mechanism and Machine Theory, vol. 44(3), pp. 633-645, 2009.
9. Benjamin, P., Roman, R., Wolfgang, F., Pradalier, C., & Siegwart, R. Y., "Design and Evaluation of a Fin-Based Underwater Propulsion System", Proceedings of the 2010 IEEE International Conference on Robotics and Automation (2010).
10. Shang, L., Wang, S., Tan, M., & Cheng, L.: Swimming locomotion modeling for biomimetic underwater vehicle with two undulating long-fins. Robotica, vol. 30(6), pp. 913-923, 2012.
11. Nguyen, V. D., Phan, D. K., Pham, C. A. T., Kim, D. H., Dinh, V. T., & Nguyen, T. T., "Study on Determining the Number of Fin-Rays of a Gymnotiform Undulating Fin Robot. AETA 2017 - Recent Advances in Electrical Engineering and Related Sciences: Theory and Application, Lecture Notes in Electrical Engineering 465. Springer, 2018.
12. Nguyen, V. H., Nguyen, V. D., Duong, V. T., Nguyen, H. H., Le, V. S., & Nguyen, T. T., "Experimental Study on Kinematic Parameter and Undulating Pattern Influencing Thrust Performance of Biomimetic Underwater Undulating Driven Propulsor", International Journal of Mechanical & Mechatronics Engineering, vol. 20(5), 2020.
13. A. Amory and E. Maehle, "Modelling and CFD Simulation of a Micro Autonomous Underwater Vehicle SEMBIO", Proceedings of OCEANS 2019, MTS/IEEE, pp. 1–6, 2019, doi: 10.1109/OCEANS.2018.8604768.
14. G. Pan, B. Hu, X. Du, and Y. Wang, "Research on hydrodynamic characteristics of underwater gliding UUV based on the CFD technique", Adv. Mater. Res., vol. 479–481, pp. 729–732, 2012, doi: 10.4028/www.scientific.net/AMR.479-481.729.

[O-1-9] Mechanical Modular Design of Photovoltaic Panel Cleaning Robot

Tan Tien Nguyen[1,3,†], Van Binh Duong Nguyen[2], Sang Bong Kim[4]

[1] National Key Laboratory of Digital Control and System Eng. (DCSELab), 268 Ly Thuong Kiet Street, District 10, Ho Chi Minh City, Vietnam.
[2] Faculty of Mechanical Eng., Ho Chi Minh City University of Technology (HCMUT), 268 Ly Thuong Kiet, District 10, Ho Chi Minh City, Vietnam.
[3] Vietnam National University Ho Chi Minh City, Linh Trung Ward, Thu Duc District, Ho Chi Minh City, Vietnam.
[4] Pukyong National University, Busan, Korea.

Abstract

In this paper, the Mechanical Modular Design of the PV Panel Cleaning Robot is based on the old version of DCSELab's solar battery cleaning robot. First, the article gives an overview of modularity in mechanical design. Secondly, modularization of the body and brush assembly aims to adapt to the variety of sizes of solar panels. Finally, the article proposes the structure of the solar battery cleaning system and Solar Cleaning Robot's family

Keywords: *Modular design, Photovoltaic Panel (PV) cleaning robot*

1. Introduction

Solar energy has surpassed wind energy as the leading alternative energy source in terms of its contribution to power production. In order to boost productivity during the day, it is crucial to clean the surface of solar cells because solar energy only functions during the day and is halted at night. Additionally, the demand for solar energy is increasing, resulting in a growing market for the solar panel industry and a variety of solar array systems. Therefore, creating a system for cleaning solar panels is essential to constantly maintaining the efficiency of the panels. However, the solar panel cleaning method must be diverse in order to match the diversity of the panel installation system. This study presents the family of products with the goal of ensuring that each component of the system meets the aforementioned variety.

About the variety of solar panel systems, thanks to advancements in technology, a solar panel array may now support up to 4 vertically mounted solar panels and 8 horizontally installed solar panels for ground-mounted systems, and a solar panel system on a factory roof can have up to 5 horizontally placed solar panels in a row. Thus, a solar panel cleaning system is considered effective when the cleaning performance is sufficient and able to cover the full surface of the system, also known as the system's working surface. The graphic below depicts the working surface of Vietnam's solar panel cleaning system in accordance with the previous survey.

About the solar cleaning robot's family, is a collection of robots with each robot will fit each type of size *W*

of the work surface. In the world, Solar cleaning robots typically use a combination of water, brushes, and sometimes a mild detergent to clean the solar panels. They are usually equipped with sensors and GPS technology to navigate around the solar panels and avoid obstacles. Some solar cleaning robots are also equipped with cameras, which allow operators to monitor the cleaning process remotely. Solar cleaning robots come in a range of sizes and configurations to suit different types of solar panels and environments. Some are designed for use on ground-mounted solar panels, while others are designed for use on rooftop solar panels. Some solar cleaning robots are fully autonomous, while others require human operators to control their movements and cleaning functions. The Solar cleaning robot' family is designed with modularity in mind, which means that the robots can transform into each other.

The paper presents a solution to modularize the outdated solar panel cleaning technology for future development and expansion in order to address the aforementioned issue, which is divided into 4 parts, and section 2 illustrates the modularity design in solar cleaning robot system and how the solar cleaning robot family is constructed. A summary of the result of the mechanical modularization is provided in Section 3. Ultimately, the issues with the system's modularization will be covered in section 4.

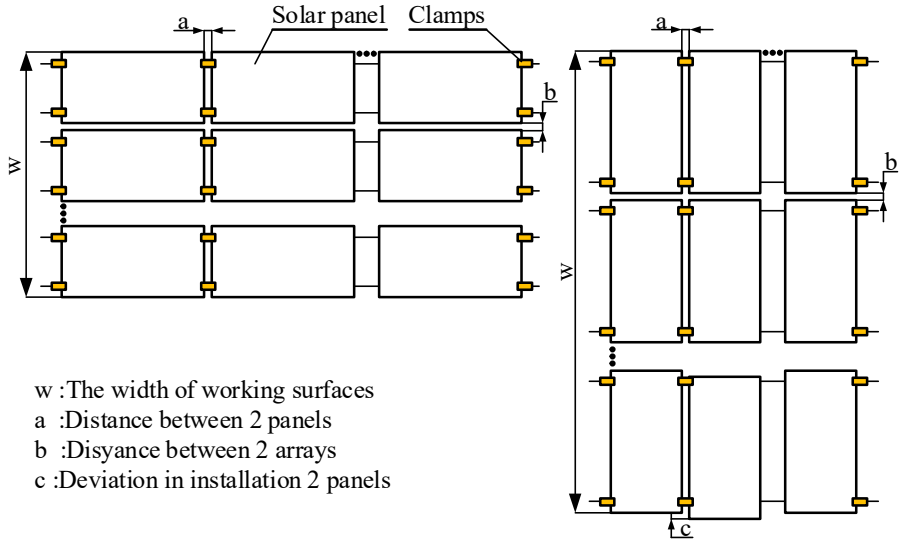

Figure 1. Working surface of the solar cleaning robot's family in Vietnam

2. Modularization in the mechanical system of the solar panel cleaning system

About the modular design and categories of modularity

The result of the modular design is a modular product that performs various common functions through the combination of independent building blocks or modules. The general function performed by the product can be broken down into sub-functions performed by the various modules or components. Therefore, an important aspect of modular is the creation of a basic core unit to which different components (modules) can be attached, thereby allowing the manufacture of multiple versions of the same module. Based on those properties and the types of interactions between modules which are analyzed based on the types of interaction between the different modules within a product, there are 4 categories of modularity: Component-swapping, component-sharing, bus

and fabricate-to-fit.

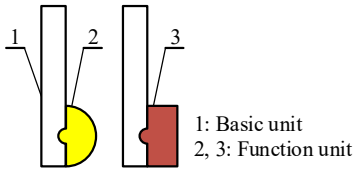

Figure 2. Component-Swapping Modularity

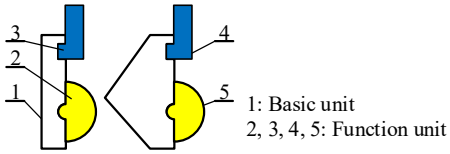

Figure 3. Component-Sharing Modularity

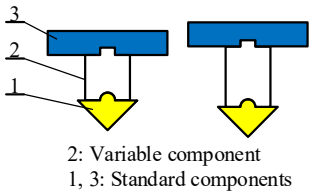

Figure 4. Fabricate-to-Fit Modularity

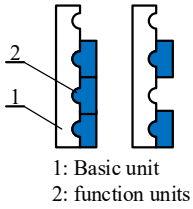

Figure 5. Bus modular

Component-Swapping Modularity, this type of modularity method allows creating the product family, which different product variants belong to, by combining alternative types of components with the same basic component or product. *Component-Sharing modularity*, this type of the modularity figures out that the product families are created by combining different modules with the same basic component.

Fabricate-to-Fit Modularity, in the product, there is a combination between standard components and one or more variable components, which the physical dimension of that component can be modified or adjusted. *Bus modularity*, this property is applied when there are several function units match with a basic unit. Bus modularity allows these function units to vary in number and locations.

About solar cleaning robot's family

Solar cleaning robot's family is a set of robots that have the same function, which is cleaning the surface of the solar panels. It contains 2 types of robots which are mobile robots and autonomous robots; depending on the type of condition of working surface, there will be compatible robots working on there. For example, the mobile robot will work on the working surface which has a small number of solar panels in 1 array and the type autonomous robot will work on the large solar mounting, specially in the solar farm. This product's family is constructed by 2 main modules which are the body, brush modules; these module are designed in the direction of modularity, which means each module is designed to have ability to transform into a new state in order to match with a new element in the product's family. And this function will be described in detail in the section below.

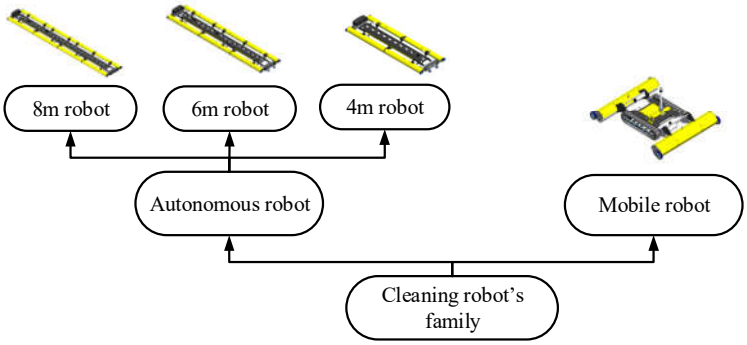

Figure 6. Solar cleaning robot's family

About the body module

The body module's 2 primary functions are to create a framework for attaching the brush module and to assist the robot in moving around the work surface. The belt-tracked module and the chassis module are the 2 main clusters that make up the body module, which serves the aforementioned functions. Moreover, the belt-driven tracked module includes a suspension system in addition to a belt drive. The belt drive is made to be able to work at inclination angles between 12° ÷ 20° as shown in the following diagram.

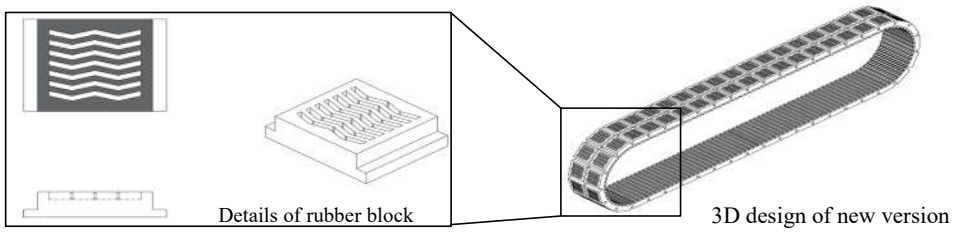

Figure 7. Belt track design

In contrast, adding extra support wheels to an autonomous robot's ends will also help it function well at high degrees of inclination. This approach highlights the modular bus's design and perceives the addition of extra wheels as an add-on feature. However, belt-tracked modules play a significant role in modularity in addition to functioning on huge sloped surfaces. The body module's function is to be able to meet all working surface requirements, including the working surface's width. In order to tackle the preceding difficulty, the article suggests an approach that uses the component-sharing modularity type and treats the belt-tracked module as a function unit and the chassis module as the basic unit. Due to the nature of component-sharing modularity, the belt-tracked module can be freely installed, which implies that there will be a corresponding chassis module for each width of the working surface, and those chassis modules can be placed with the belt-tracked module.

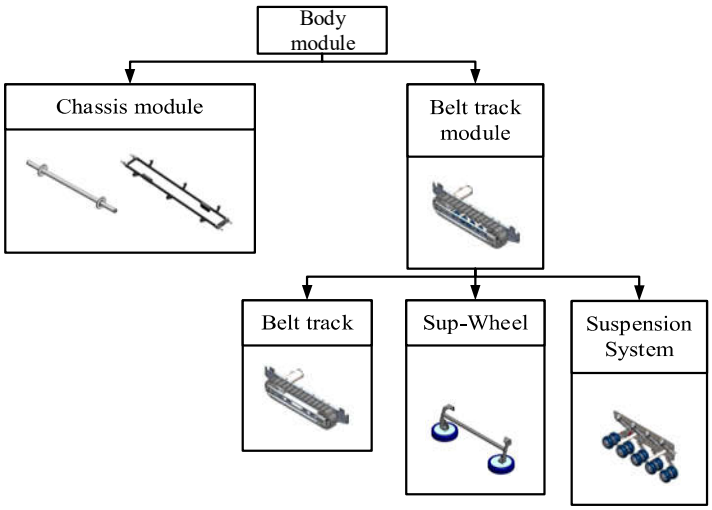

Figure 8. Body module modulization

In addition to using component-sharing modularity to be able to shift from a mobile robot to an autonomous type, fabricate-to-fit modularity will be an ideal additional option in designing a family of solar cleaning robots. Specifically, the creation of 6-meter and 8-meter solar cleaning robots begins by extending the chassis module of the 4-meter solar cleaning robot. It is clear that in mechanical design, component-sharing modularity and fabricate-to-fit modularity complement each other very effectively.

As demonstrated by the utilization of the two types of modularity discussed above, modularity gives us the ability to adapt in order to meet the requirements of the situation. However, a closer examination reveals that the extension of the chassis module will make the mechanical structure heavier and result in the body module's loss of stability.

About the brush module

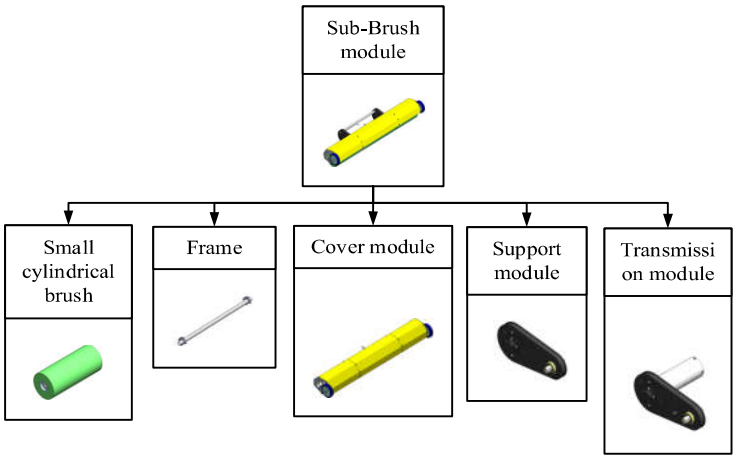

Figure 9. Sub-brush module modulization

The primary function of the brush module is to clean the work area with water using a cylindrical brush made of hard fibers. It is clear that this module is crucial for assessing the system's overall efficacy. Only when the entire work surface is cleaned does the system's cleaning performance reach its peak. Thus, the length of the brush assembly plays a crucial role and must be long enough to cover the entire work surface. As a result, a long cylindrical

brush cannot be produced since the manufacturing costs are too high. This article suggests a technique for incorporating a modular bus into the brush module's design. In other words, we divided the brush module into a smaller, cyclical brush-based sub-brush module. This segmentation offers us two benefits. The first advantage stems from the sub-brush modules' adaptability, which can be changed by adjusting the length of the small cylindrical brush. This feature is ideal for the multi-factor-sized format of solar panels in Vietnam. The brush module's construction from sub-modules provides a second advantage by allowing us to maximize the number of small cylindrical brushes bridged into the brush module.

As can be seen, the brush modules of mobile and autonomous are fully comparable in texture but different in size for small cylindrical brushes, which are similar to the sub-brush textures of modules I, II, and III. More specifically, the 4-meter, 6-meter, and 8-meter solar cleaning robots' brush module structures are all made up of 3 sub-brush modules, I, II, and III. Hence, adding the sub-brush II module between the sub-brush modules I and III will result in the transformation of a 6-meter solar cleaning robot into an 8-meter solar cleaning robot, similar to converting the brush module of a 4-meter solar cleaning robot into a 6-meter solar cleaning robot. All of those categories illustrate the properties of bus modular type.

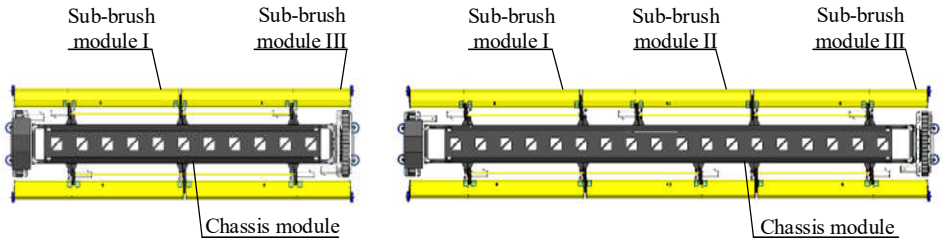

Figure 10. Bus modular in Autonomous robot type

3. Results and Discussion

About the result

This study demonstrates the conceptual results of applying modularity designs to the DCSELab-developed solar panel cleaning system in context of the previously mentioned possibilities. The chassis module is the single component that separates the 2 solar panel cleaning robots, which were built from 2 separate primary assemblies - the track module and the brush module - as shown in the graphs below. The solar cleaning robot will be used and operated in different ways for each type of chassis module, as a result, the article suggests a family of solar cleaning robots.

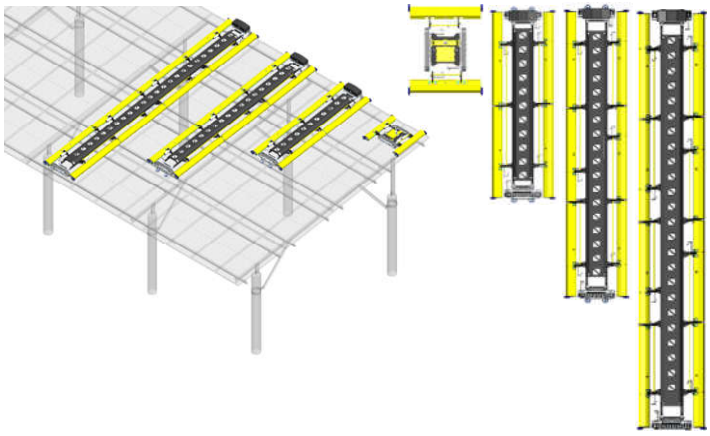

Figure 11. Modular design in Solar panel cleaning robot

Regarding the experimental part, DCSELab has completed and tested the body module and in the future, will complete the solar cleaning robot 4m.

About the discussion

Modularization gives us the freedom to adapt, but this will make the mechanical structure complicated, leading to an explosion in the number of installation parts, leading to increased costs. work increased. On the other hand, on the electrical side, we note that, when installing an additional brush module, more motors must be installed, resulting in a larger need for the same power supply, and the battery box will change.

Figure 12. Solar panel cleaning robot, experimental body module

4. Conclusion

It is clear that modularity in design leads to new approaches and innovative ways of thinking about creating a family of products to satisfy functional requirements. Modularization still has several flaws, which magnify the cluster's complexity and level of detail. Because design for modularity strives to simplify details and effectively produce family products, it must be accompanied by design for assembly and design for manufacture in order to be exceptional.

Acknowledgment

This research is supported by DCSELAB and funded by Vietnam National University Ho Chi Minh City (VNU-HCM) under grant number TX2023-20b-01. We acknowledge the support of time and facilities from Ho Chi Minh City University of Technology (HCMUT), VNU-HCM for this study.

References

1. Nguyen Van Binh Duong, Phan Hoang Long, and Nguyen Tan Tien, *Survey on the Current Status of Common Type Solar Panel Mounting Structure in Vietnam*, Vietnam Mechanical Engineering Journal, Vol. 299 (2023).

2. Le Nhut Thang, Phan Hoang Long, and Nguyen Tan Tien, *Survey on the Cleaning Method for Solar Photovoltaic Panel*, Vietnam Mechanical Engineering Journal, Vol. 299 (2023).

3. Amit Kumar Mondal and Kamal Bansal, *A Review of Dust Accumulation and Cleaning Methods for Solar Photovoltaic Systems*, Journal of Cleaner Production, pp. 1–22, Vol. 276 (2020).

4. Amit Kumar Mondal and Kamal Bansal, *Survey Paper – A Brief History and Future Aspects in Automatic Cleaning Systems for Solar Photovoltaic Panels*, Advanced Robotics, pp. 515–524, Vol. 29, No. 8 (2015).

5. Levin, M. S., *Modular System Design and Evaluation*, Springer International Publishing (2015).

6. Ito, Y., *Modular Design for Machine Tools,* McGraw-Hill Education (2008).

7. Kamrani, A. K., & Sa'Ed, M. S., *Product Design for Modularity*, Springer Science & Business Media (2002).

[O-1-10] Modeling of Parallel Power MOSFETs in Steady-state

Minh Nhat Huynh[1, *], Minh Khoi Nguyen Tien[1], Cong Toai Truong[1, 2, 3], Quoc Dan Le[4], Van Tu Duong[1, 2, 3], Huy Hung Nguyen[4, †], Tan Tien Nguyen[1, 2, 3]

[1] National Key Laboratory of Digital Control and System Engineering (DCSELab), Ho Chi Minh City University of Technology (HCMUT), 268 Ly Thuong Kiet Street, District 10, Ho Chi Minh City 700000, Vietnam

[2] Faculty of Mechanical Engineering, Ho Chi Minh City University of Technology (HCMUT), 268 Ly Thuong Kiet, District 10, Ho Chi Minh City 700000, Vietnam

[3] Vietnam National University Ho Chi Minh City, Linh Trung Ward, Thu Duc District, Ho Chi Minh City 700000, Vietnam

[4] Faculty of Electronics and Telecommunication, Saigon University, Ho Chi Minh City 700000, Vietnam

[†] Leading - Corresponding author: nhhung@sgu.edu.vn

[*] Presenting author: nhat.huynh1905758@hcmut.edu.vn

Abstract

In high-power applications, multiple power MOSFETs are connected in parallel and treated as a single soft switch in order to conduct much larger total load currents. However, the intrinsic parameters of power MOSFETs are different which leads to the unbalanced current of each power MOSFET, in turn, results in the overburden of the switch. In this paper, an equivalent circuit model of parallel power MOSFETs describing the dynamic current-sharing behaviors from the turn-off state to the conducting steady state has been studied. The equivalent circuit model represents the relationship between each power MOSFET's gate voltage with respect to the sharing current. The performance of the equivalent circuit model is validated through a comparison of the sharing current with respect to the gate voltage curve obtained from the proposed model and that of the experiment.

Keywords: *Unbalanced current, Parallel MOSFETs, Power MOSFETs, Silicon carbide semiconductors*

1. Introduction

The need for renewable energy sources to replace traditional fossil fuels, as well as the demand for high–power applications, is driving the advancement of battery technology and its applications in the present day [1]. The

utilization of high–voltage batteries in high–power applications has elevated the requirement for protection. As the discharge current increases, the discharge process becomes more hazardous. Overcurrent protection is essential in maintaining the safety of the batteries during operation. There are various methods for interrupting DC currents such as mechanical breakers or semiconductor devices [2].

In case there is a malfunction in the system, a circuit for interrupting the power source from the system is necessary. Both contactor and SiC MOSFET can be used as DC circuit breakers' main switches. Contactors can handle high currents, making them suitable for applications with high current loads. However, an arc might be created within the contactor when they trigger. In the worst–case scenario, they may experience welding or bouncing which shortens the lifespan of the contactor as a consequence. Besides, for protection purposes, the time it takes to restore and eliminate a fault in a security system is one of the most important parameters. The devices need to be fast enough to eliminate any fatal damage caused to battery cells and other electrical components. SiC power MOSFETs are ideal for applications that require fast protection against overcurrents or short circuits, as they can switch states quickly. Additionally, being an electronic component, MOSFETs do not produce arcs.

Nevertheless, power MOSFETs are not typically designed for handling hundreds of amperes on their own. As a result, the concept of paralleling multiple MOSFETs is unavoidable to achieve the required current ratings without breaking individuals' operating limits [3]. This method also reduces the equivalent on–state resistance which leads to a reduction in power dissipation.

This way, the current and power are expected to distribute equally between them, reducing the burden on each individual. In reality, because of various reasons, it is a key challenge to ensure the current sharing among power MOSFETs, which leads to unevenly distributed power loss and thermal dissymmetry. This paper focuses on the studying of uneven sharing current between paralleled SiC power MOSFETs.

2. Current imbalance

Paralleled power MOSFETs might experience unbalance in sharing current during two separate phases.

2.1. Dynamic current imbalance

One of them is dynamic current imbalance, which occurs during the MOSFETs' turn–on and turn–off process. Unbalanced current sharing throughout the state can cause high current spikes and overloading in certain MOSFETs, leading to reduced performance and potential thermal runaway. The imbalances stem from variations in switching time among the parallel power MOSFETs, which are affected by mismatches in threshold voltage (V_{TH}) and transconductance (g_{fs}). In addition to the device parameter mismatch, asymmetry in the cable design can also contribute to the uneven distribution of current [4]. Even though unequal current sharing during the state can have a significant impact on high–frequency applications, it only affects the DC circuit breaker for a brief moment during a fault occurrence.

2.2. Static current imbalance

On the other hand, static current imbalance directly affects the protection device's principle because most of the time, the paralleled power MOSFETs act as a conduction device. During on–state, the power MOSFETs can be considered as equivalent resistors with the values equal to their on–state resistance $(R_{DS(on)})$. For SiC power

MOSFETs, $R_{DS(on)}$ can obtain the value of hundreds or even tens of $m\Omega$ with the tolerance of $\pm 20\%$. These parallel MOSFETs all share the same drain–to–source voltage (V_{DS}), therefore the lower on – state resistance of a particular MOSFET, the higher the drain current (I_D) flowing through it, resulting in increased power dissipation. This can lead to reducing in reliability, device lifetime, and even device failure. Additionally, uneven heating of the devices can cause thermal stress, which can lead to permanent damage.

One way to mitigate the current unbalance in paralleled power MOSFETs is by relying on positive temperature coefficient (PTC) elements. A PTC element is a material that has a resistance that increases as its temperature rises, which can be used to suppress the uneven sharing current among the parallel devices to some extent. During normal operation, the MOSFETs with lower $R_{DS(on)}$ will dissipate more power and heat, causing their PTC elements to have a higher resistance and reducing the drain current flowing through them as a result. This helps equalize the drain current distribution among the paralleled MOSFETs, preventing thermal stress, hot spots, and prolonging the device's lifespan, which is called thermal self–stabilization.

While the positive temperature coefficient of SiC MOSFETs can help to balance current sharing to some extent, it may not always be sufficient for ensuring balanced current distribution in high current applications. In high current application, the total current passing through the system is large, and even small imbalances in the current distribution can cause significant power dissipation and temperature rise in one or more of the MOSFETs. Besides, the use of PTC elements to balance current in paralleled SiC MOSFETs may not always be effective if the current imbalance is too severe. The sensitivity of $R_{DS(on)}$ to temperature varies based on the type of MOSFET, as shown in the equation below [5]. Consequently, the higher temperatures can cause degradation of the MOSFETs over time, reducing their performance and lifespan. Therefore, relying exclusively on PTC for suppressing static current imbalance is inappropriate.

$$R_{DS(on)-t} = R_{DS(on)-25}\left(\frac{t + 273.15}{298.15}\right)^n \quad (1)$$

Where: $R_{DS(on)-t}$ is MOSFETs on–state resistance at temperature t (℃); $R_{DS(on)-25}$ is MOSFETs on-state resistance at 25℃; and n is the fitting parameter. This parameter varies depending on the type of MOSFET, which is particularly low in SiC devices compared to SI one [6].

2.3. Technique for active load balancing

Power MOSFETs are voltage–driven devices, in which their conductance ability is varied depending on the gate–to–source voltage (V_{GS}) applied to them. Based on [7], the model for simulating the drain current I_D of a SiC power MOSFET can be calculated by equations (2) and (3):

During linear region: $V_{GS} > V_{TH}; V_{DS} < V_{GS} - V_{TH}$

$$I_D = \mu_n C_{ox}\frac{W}{L}\left[(V_{GS} - V_{TH})V_{DS} - \frac{V_{DS}^2}{2}\right] \quad (2)$$

During saturated region: $V_{GS} > V_{TH}; V_{DS} \geq V_{GS} - V_{TH}$

$$I_D = \frac{1}{2}\mu_n C_{ox}\frac{W}{L}(V_{GS} - V_{TH})^2 \quad (3)$$

Where: μ_n is electron mobility; C_{ox} is oxide capacitance; W is width of the gate; L is length of the gate; V_{DS} is drain–to–source voltage; V_{GS} is gate–to–source voltage; and V_{TH} is gate threshold voltage.

Aforementioned, their resistance can obtain very small values of hundreds or even tens $m\Omega$, which leads to a much smaller V_{DS} compare to the difference between gate–to–source voltage and threshold voltage $(V_{GS} - V_{TH})$. Therefore, based on [8] and equation (4), the drain current during on–state period can be determined as shown:

$$I_D = \mu_n C_{ox}\frac{W}{L}(V_{GS} - V_{TH})V_{DS} \text{ for } \left(V_{DS} \ll (V_{GS} - V_{TH})\right) \quad (5)$$

As a result, the on–state resistance can be expressed as an equation depending on V_{GS}:

$$R_{DS(on)} = \frac{1}{\mu_n C_{ox}\frac{W}{L}(V_{GS} - V_{TH})} \quad (6)$$

Equation (5) shows that the power MOSFET can be considered as a voltage controll resistor within the steady–state region. In particular, $R_{DS(on)}$ can be varied depends on V_{GS}, which leads to a method for actively balance the sharing current.

3. Investigation of static current unbalance suppression

3.1. Overall system description

A system has been constructed to monitor the distribution of current among power MOSFETs when they are connected in parallel. Additionally, the system is designed to assess the effect of both temperature and V_{GS} on the current sharing. This is achieved by allowing the system to observe the current flowing through each MOSFET as well as their temperature, and by enabling the adjustment of the V_{GS} applied to each MOSFET separately. The system includes:

1. Two IRFP4688 MOSFETs.
2. Two ACS758 hall current sensors.
3. Two NTC Thermistor Sensors.
4. Dummy loader.

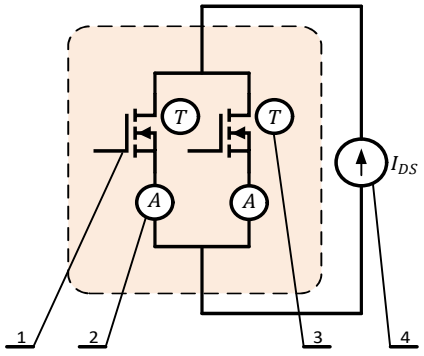

Figure 1. Principle of steady–state paralleled MOSFETs

3.2. Experiment model

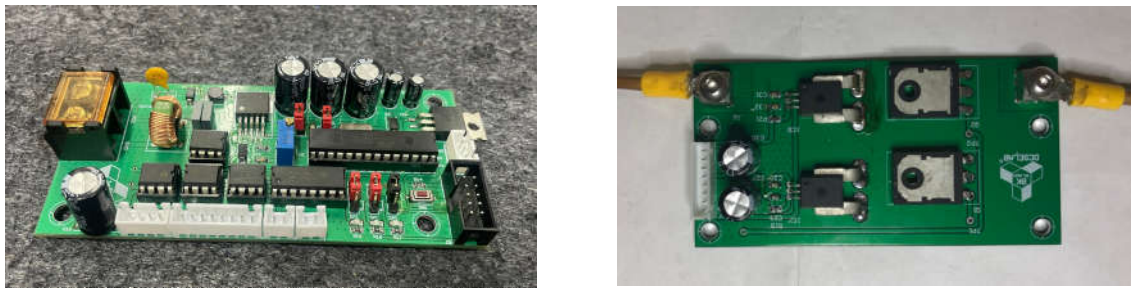

(a) Control circuit **(b) Power circuit**

Figure 2. Printed circuit board of steady – state paralleled MOSFETs

Fig. 2 depicts a printed circuit board (PCB) that is designed to conduct test cases with parallel MOSFETs. **Fig. 2a** is the control board, featuring an AVR chip at its core that guarantees the consistency of pulse width modulation and data collection. **Fig. 2b** displays an integrated circuit of two IRFP4688 MOSFETs connected in parallel, similar to the system description outlined earlier. The division of control and dynamic circuits into separate entities helps to minimize interference and ensures the accuracy of the experimental results by avoiding any potential errors.

Figure 3. Dummy loader for testing paralleled MOSFETs

Fig. 3 shows the Dummy loader used in this paper. The dummy load system consists of six connected load resistors, with their specific parameters outlined in **Table 1**.

Table 1. The parameters of the dummy loader

Parameter	Unit	Value
Overall size	mm	$600 \times 400 \times 150mm$
Mass	kg	10
Range	Ω	$[0-6]$
Resolutions	Ω	$1/3$

3.3. Experiment and results

Case 1: Using ARX Method to identification of one MOSFET.

First, individual experiments were performed on each MOSFET to find an equation representing the characteristics of the IRFP4688 MOSFETs. The condition experiment is shown in **Table 2**.

Table 2. The parameters of the resistance load

Parameter	Unit	Value
Power		LiFePO4 24V (20Ah – 5C)
Temperature	℃	25
Number of MOSFETs	pieces	10
Sampling time	s	0.05

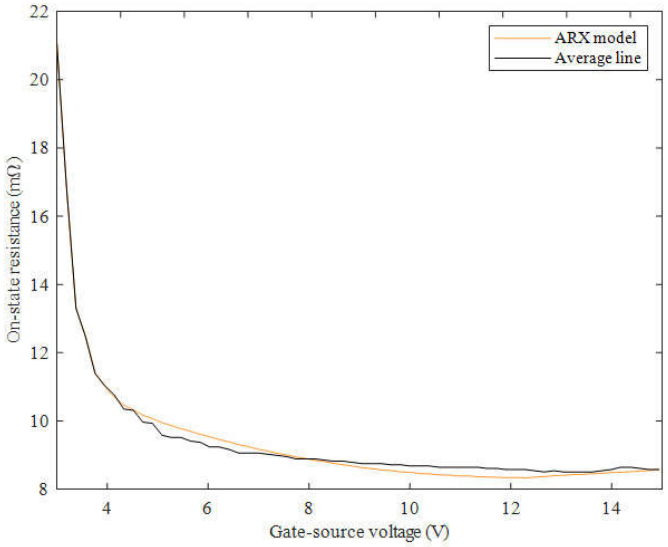

Figure 4. Average data and ARX model of 10 MOSFETs

The relationship between V_{GS}, and R_{DS}, is modeled using the ARX model. **Fig. 4** displays the average data line of 10 MOSFETs (represented by the black line) and the ARX model (represented by the orange line) of the system. The obtained discrete–time ARX model is:

$$A(z)y(t) = B(z)u(t) + e(t)$$

With:

$$A(z) = 1 - 0.955z^{-1} - 0.336z^{-2} + 0.218z^{-3} + 0.056z^{-4}$$

$$B(z) = -0.005z^{-6} + 0.054z^{-7} - 0.054z^{-8} + 0.016z^{-9}$$

Case 2: Test the model was founded with a different MOSFET from the previously obtained data set.

With the same experimental conditions as case 1, the data of the 11th MOSFET is collected and shown in **Fig. 5**. The test data line has a degree of compatibility with the model (error of about 3%).

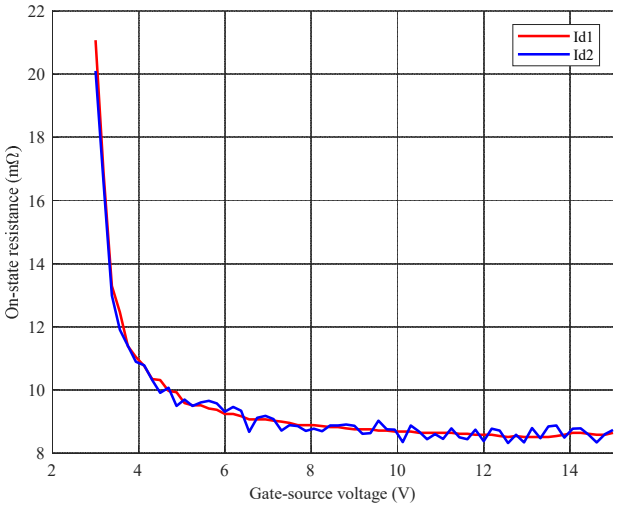

Figure 5. Evaluate ARX model

Case 3: The case of parallel MOSFETs connected.

Experimental conditions of the parallel MOSFET model are shown in **Table 3**.

Table 3. The parameters of the resistance load

Parameter	Unit	Value
Power		LiFePO4 24V (20Ah – 5C)
Temperature	℃	25^o
Time of experiment	min	20
Sampling time	ms	50

The process of observing the thermal and current balance through pulse width modulation (V_{GS}) is difficult to accomplish when working with a single MOSFET. To overcome this challenge, the experiment was conducted with two paralleled MOSFETs so that changes in temperature and current per MOSFET could be clearly observed. The progress is presented below.

An experiment is conducted to evaluate the capability of thermal self–regulation by applying a total current of 20A to the system. During the experiment, each MOSFET is activated with the maximum V_{GS} while recording both the temperature and the current flowing through each device.

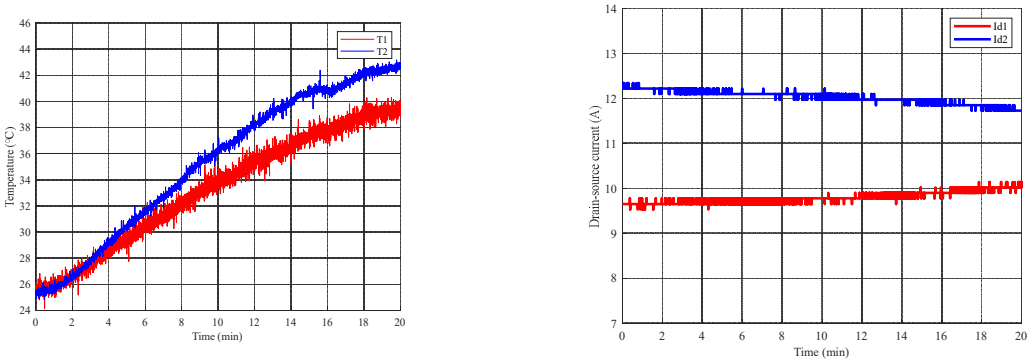

(a) Temperature of two MOSFETs **(b) Drain current of 2 MOSFETs**

Figure 6. Sharing drain current and thermal self–regulation of paralleled MOSFETs

The collected data reveals a constraint in relying solely on their PTC element to balance the discharge current, which is especially pronounced for SiC devices. The graph illustrates the temperature discrepancy between the two devices. Although the PTC element helps prevent the worst outcome – thermal runaway, it still negatively impacts the lifespan and reliability of the system, especially in high–power applications. As a result, in order to entirely suppress the uneven in sharing current, it is advisable to implement an active load balancing technique.

As aforementioned, MOSFETs' on–state resistance can be controlled by adjusting V_{GS} applied to each MOSFETs. By manipulating the gate–source voltage, it becomes feasible to regulate the current that flows through each MOSFET and achieve a balanced distribution of current among paralleled MOSFETs.

An experiment is performed to assess the viability of the method mentioned above. This involves applying the maximum gate voltage to one device and altering the gate voltage on the other device, while simultaneously monitoring the flow of current between two devices.

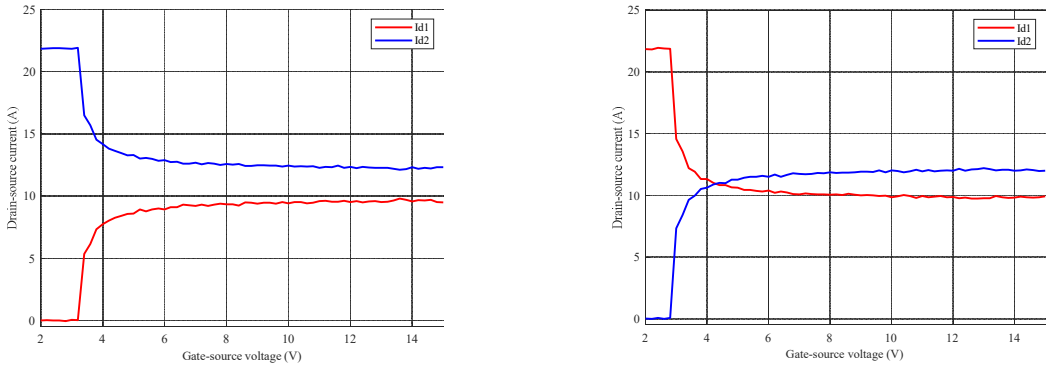

(a) Drain current with MOSFET 1's gate – source voltage varying **(b) Drain current with MOSFET 2's gate – source voltage varying**

Figure 7. Adjust sharing current between two MOSFETs

The results of the experiment (shown in **Fig. 7**) demonstrate that the division of current among the MOSFETs can be significantly altered. The figure highlights the presence of an intersection point where the shared current between the two MOSFETs reaches a state of balance. This outcome implies that the active balancing method,

facilitated by the adjustment of V_{GS}, can maintain a balanced load current even under varying conditions, further enhancing the reliability and efficiency of the system.

3. Conclusion

For the purpose of improving safety and reliability in high–power applications, a DC circuit breaker that utilizes parallel MOSFETs as the primary switch is an appropriate solution. This research examines the issue of unequal current division among these paralleled MOSFETs during steady–state and offers a means to resolve it. The results reveal that a balanced state among MOSFETs can be achieved more effectively and safely through the adjustment of their $R_{DS(on)}$ values by means of active balancing instead of solely relying on PTC element.

Acknowledgements

This research is funded by Vietnam National University Ho Chi Minh City (VNU-HCM) under grant number TX2023-20b-01. We acknowledge the support of time and facilities from National Key Laboratory of Digital Control and System Engineering (DCSELab), Ho Chi Minh City University of Technology (HCMUT), VNU-HCM for this study.

References

1. X. Pu *et al.*, “Recent Progress in Rechargeable Sodium-Ion Batteries: toward High-Power Applications”, *Small*, vol. 15, no. 32. Wiley-VCH Verlag, Aug. 01, 2019. doi: 10.1002/smll.201805427.

2. G. Papadopoulos, “State-of-the-art DC Current Interruption Concept using SiC MOSFETs”.

3. IEEE Power Electronics Society, Annual IEEE Computer Conference, IEEE Industry Applications Conference, Annual IEEE Energy Conversion Congress and Exposition 5 2013.09.15-19.

4. H. Wang and F. Wang, “Power MOSFETs Paralleling Operation for High Power High Density Converters”, 2006.

5. J. Jose, A. Ravindran, and K. K. Nair, “Study of Temperature Dependency on MOSFET Parameter using MATLAB”, *International Research Journal of Engineering and Technology*, 2016, [Online]. Available: www.irjet.net

6. Z. Zeng, X. Zhang, and Z. Zhang, “Imbalance Current Analysis and Its Suppression Methodology for Parallel SiC MOSFETs with Aid of a Differential Mode Choke”, *IEEE Transactions on Industrial Electronics*, vol. 67, no. 2, pp. 1508–1519, Feb. 2020, doi: 10.1109/TIE.2019.2901655.

7. T. Sakurai and A. R. Newton, “A Simple MOSFET Model for Circuit Analysis”, 1991.

8. J. Fu, “Fundamentals of On-Resistance in Load Switches Application Report Fundamentals of On-Resistance in Load Switches”, 2016. [Online]. Available: www.ti.com

[O-1-11] Optimal Central Pattern Generator for Swimming Gait of Robotic Fish Using Mutant Particle Swarm Optimization

Quoc Tuan Vu[1, *], Ba Ngoc Pham Tran[1], Van Tu Duong[1, 2, 3, †], Huy Hung Nguyen[4], Thien Phuc Tran[1, 2, 3], and Tan Tien Nguyen[1, 2, 3]

[1] National Key Laboratory of Digital Control and System Engineering (DCSELab), Ho Chi Minh City University of Technology (HCMUT), 268 Ly Thuong Kiet Street, District 10, Ho Chi Minh City 700000, Vietnam

[2] Faculty of Mechanical Engineering, Ho Chi Minh City University of Technology (HCMUT), 268 Ly Thuong Kiet, District 10, Ho Chi Minh City 700000, Vietnam

[3] Vietnam National University Ho Chi Minh City, Linh Trung Ward, Thu Duc District, Ho Chi Minh City 700000, Vietnam

[4] Faculty of Electronics and Telecommunication, Saigon University, Ho Chi Minh City 700000, Vietnam

[†] Leading - Corresponding author: dvtu@hcmut.edu.vn

[*] Presenting author: quoctuanvu@hcmut.edu.vn

Abstract

Due to the fast swimming and excellent maneuverability, bio-robotic fish have a significant influence on the development of underwater vehicles. In the paper, a black knifefish-inspired robot with an elongated undulating fin is investigated for locomotion control using an improved CPG model. The proposed CPG network has sixteen fin rays connected Hopf oscillators for creating fish-like swimming gaits. To identify a set of optimal parameters for the modified CPG network, mutant particle swarm optimization (MPSO), an improved form of particle swarm optimization (PSO), is introduced. The MPSO replaces the worst particles with a mutant particle with an improved velocity vector so that particles can get a big thrust to escape from the local optimum in order to enhance the propulsive force of robotic fish. Additionally, a comparison of MPSO with the traditional PSO and genetic algorithm (GA) has been performed in tuning the parametric values of CPG model to prove the superiority of the introduced method. The obtained results show that the average propulsive force of the untested material is risen 5.92%, as compared to the straight CPG model.

Keywords: *Mutant particle swarm optimization, Hopf oscillators, Genetic algorithm, Fish swimming modes*

1. Introduction

Researchers are paying attention to robotic technologies, particularly in the hard-to-reach domains of space exploration and oceanography. Autonomous underwater vehicles (AUVs), which use various propulsion mechanisms such as jets, axial propellers, and bodies or fins, have made significant advancements in the field of ocean science [1]–[3]. Among AUVs, bionic fish robots using fin propulsion systems have been widely developed due to their minimal noise, great maneuverability, and quick speed. Recently, various researchers have studied how to enhance the motion performance of bio-robotic fishes, with an emphasis on dynamic modeling, locomotion control, and optimization.

In terms of motion control, the CPG network is often used to produce the rhythmic movements of fish robots [4]–[6]. Biological CPGs include neural networks in the spinal cord that generate cyclic muscle activation patterns such as respiration, chewing, or leg movement during walking [7]. CPGs are capable of producing rhythmic movement without stimulus signals generated by sensory feedback or higher control centers. To increase the movement efficiency of the fish robot, a set of CPG characteristic parameters must be chosen because the differential equations in the CPG model involve many uncertain parameters. Brown suggested a CPG model involving two different types of the mutually inhibiting neuron [8]. Grillner [9] offered a lamprey biological model for a minimal robot. A multi-objective genetic algorithm built on a CPG model was used by Ryota et al. to manage the gait of quadruped robots [10]. In order to simulate coupled Hopf-based CPG oscillator chains, Hu et al. created a novel numerical approach that implemented online swimming gait learning for two robotic fish[11]. Recently, heuristic search is widely applied for tuning the parameters of the CPG network. In paper [12], the genetic algorithm (GA) is used for the rhythmic generation based on CPG models by establishing the weight values of the coordination between oscillators. The authors in [13] use particle swarm optimization (PSO) to find the optimal characteristic parameters of the Hopf oscillators-based CPG for improved propulsive performance. Although these meta-heuristic algorithms have well-resulted in seeking the CPG parameters, they are often trapped in local optima. In this brief, a new variant of PSO, namely Mutant Particle Swam Optimization (MPSO) is investigated to overcome this problem. The proposed MPSO-based CPG not only increases the average propulsive force of the undulating fin robot for purpose of making a faster movement but also exactly finds the global optimal.

2. Related Problems

2.1. Elongated Undulating Fin Robot

A self-propelled, sixteen-jointed robotic fish has been created and is used as the controlling system, as shown in Fig. 1.

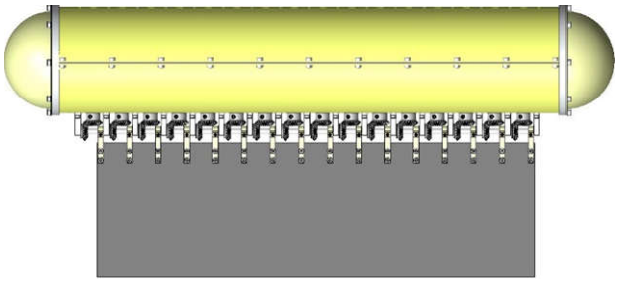

Figure 1. The 3D design diagram of the undulating fin

The morphology of the artificial robotic fish was simulated based on black knifefish. However, its bionic fins are not entirely like those of a natural black knifefish. It features sixteen fins and a flexible membrane that is mounted on the straight-axis base of underwater vehicles. Sixteen servo motors, each for one fin-ray, are utilized to simulate fish-like 3D swimming. The main controller is an ARM-based STM32 microcontroller that gathers data from sensors like the gyroscope and depth sensor. The distance between the adjacent link is 45mm and the length of the fin-ray is 150mm.

2.2. Hopf Oscillator-based CPG Model

Many efforts have been made to construct CPG models, many of which were inspired by CPG-based brain control mechanisms such as the Matsuoka model, the Kimura oscillator model, and the Ijspeert phase oscillator model [28]. In this article, a CPG model based on Hopf oscillators is used, as given in Eq. (1):

$$\begin{cases} \dot{p_i}(t) = \delta(A_i^2 - p_i^2(t) - q_i^2(t))p_i(t) - 2\pi f q_i(t) \\ \dot{q_i}(t) = \delta(A_i^2 - p_i^2(t) - q_i^2(t))q_i(t) - 2\pi f p_i(t) \end{cases} \quad (1)$$

where $\boldsymbol{p}$ and $\boldsymbol{q}$ present state variables of the non-linear oscillator; $\boldsymbol{A}$ and $\boldsymbol{f}$ are known as the amplitude and the intrinsic frequency of the oscillator and $\boldsymbol{\delta}$ is the convergence speed.

It can be observed from Eq. (1), the CPG model adopts the topology of a chain of weakly coupled Hopf oscillators. Each CPG unit will regulate a joint of a bionic robotic fish as seen in Fig. 2. The many components of robotic fish may be coordinated as a whole through the mutual inhibition and nearby coupling between CPG units. By adjusting characteristic parameters $\boldsymbol{f}$ and $\boldsymbol{A}$, it can control the oscillator frequency and amplitude of each joint of the robotic fish.

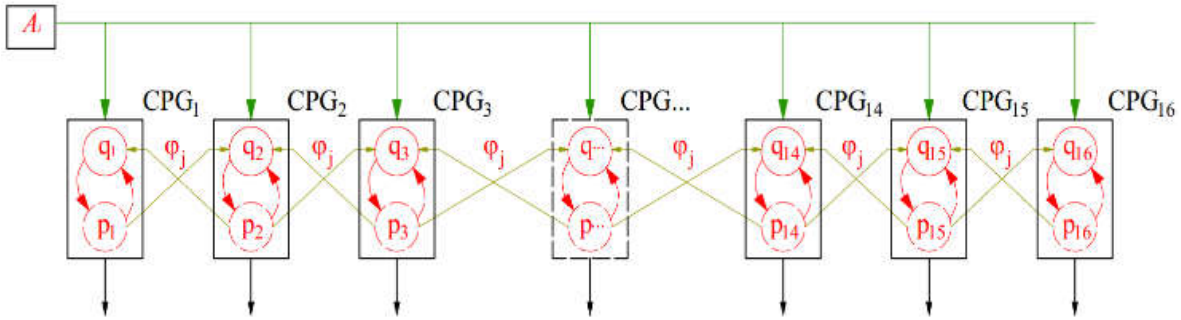

Figure 2. Structure of the CPG network with bidirectional couplings

3. Proposed M-PSO methods for optimizing the parameters of CPG

3.1. Proposed M-PSO

PSO simulates the social behavior of some species like flocks of birds and schools of fish to exploit the best solution in a non-linear search space [14], [15]. Each particle updates its next positions by three following values, including the current velocity of that particle, its previous best position (P_{best}) and the best fitness value (G_{best}). Mathematically, the updated positions of each particle in the search space can be expressed using the two equations as follows:

$$V_{i,j}^{k+1} = \omega \ \ V_{i,j}^{k} + c_1 r_1 (P_{best}{}_{i,j}^{k} - X_{i,j}^{k}) + c_2 r_2 (G_{best}{}_{j}^{k} - X_{i,j}^{k}) \quad (2)$$

$$X_{i,j}^{k+1} = X_{i,j}^{k} + V_{i,j}^{k+1} \tag{3}$$

where c_1 and c_2 are two acceleration factors, r_1 and r_2 are two random numbers generated between [0 1]; whereas w is the inertia weight of the current movement of the population. In Eq. (2), ${P_{best}}_{i,j}^{k}$ represents the personal best j^{th} component of the i^{th} individual, whereas ${G_{best}}_{j}^{k}$ represents the j^{th} component of the best individual of the population up to the iteration k. The initial P_{best} of each particle is their initial position, whereas the initial G_{best} is the initial best particle position among the randomly initialized population. The P_{best} and G_{best} of each particle are updated as follows:

$$\text{If } f(X_i^{k+1}) < f(P_{best_i}^{k}) \; then \; P_{best_i}^{k+1} = {X_i}^{k+1} \; else \; P_{best_i}^{k+1} = P_{best_i}^{k} \tag{4}$$

$$\text{If } f(X_i^{k+1}) < f(G_{best}^{k}) \; then \; G_{best}^{k+1} < X_i^{k+1} \; else \; G_{best}^{k+1} = G_{best}^{k} \tag{5}$$

where $f(X)$ is the objective function.

Due to the presence of inertia weight that is less than one (between 0.4 and 0.9), the velocity of each particle becomes very small after a certain number of iterations. This makes each particle unable to change its position considerably and pushes particles into a local optimum minimum. To overcome this problem, a novel M-PSO is proposed to replace the worst particles with a mutant-particles called as M_{best} in order to improve the velocity vector of each particle, so that particles can get a big thrust to push them out of the local optimum. For a population of $N \times D$, where N is the size of the swarm and D is the dimension of each particle, M_{best} can be generated as follows:

for $n = 1{:}\, D$

$$M_{best_n} = P_{best}(randi(N, 1), n)$$

End

where $randi(N, 1)$ is a function uniformly generating an integer between 0 and N. Thus, in the above for-loop, a total of D integers is generated and the corresponding component from each column is selected from the matrix P_{best} to form a vector M_{best}. Once M_{best} is generated, and the corresponding objective function is also evaluated. Also, the objective function corresponding to the worst particle is evaluated. If the mutant particle has the better value of the objective function, then the worst particle is replaced by M_{best}. It can be expressed as follow;

$$If \; f\left(M_{best}^{k+1}\right) < f\left(P_{best_{worst}}^{k}\right) then \; P_{best_{worst}}^{k} = M_{best}^{k+1} \tag{6}$$

3.2. MPSO-based CPG model

As mentioned above, the amplitude of each joint of the robotic fish can be adjusted by the change of characteristic parameters A. In this sub-section, a novel MPSO is applied to obtain a set of optimum amplitudes by maximizing the average propulsive force called the objective function. The optimization problem of CPG model can be posed in the following way:

$$\text{Maximizing:} \quad F = \frac{1}{\Delta t}\int_0^{\Delta t} F(t)dt \tag{7}$$

$$\text{Subject to:} \quad \begin{cases} A_{min} \le A \le A_{max} \\ A_r < A_{r+1}, r = 1 \div 16 \end{cases} \tag{8}$$

The optimization process of MPSO-based CPG model is performed as shown in Fig. 3.

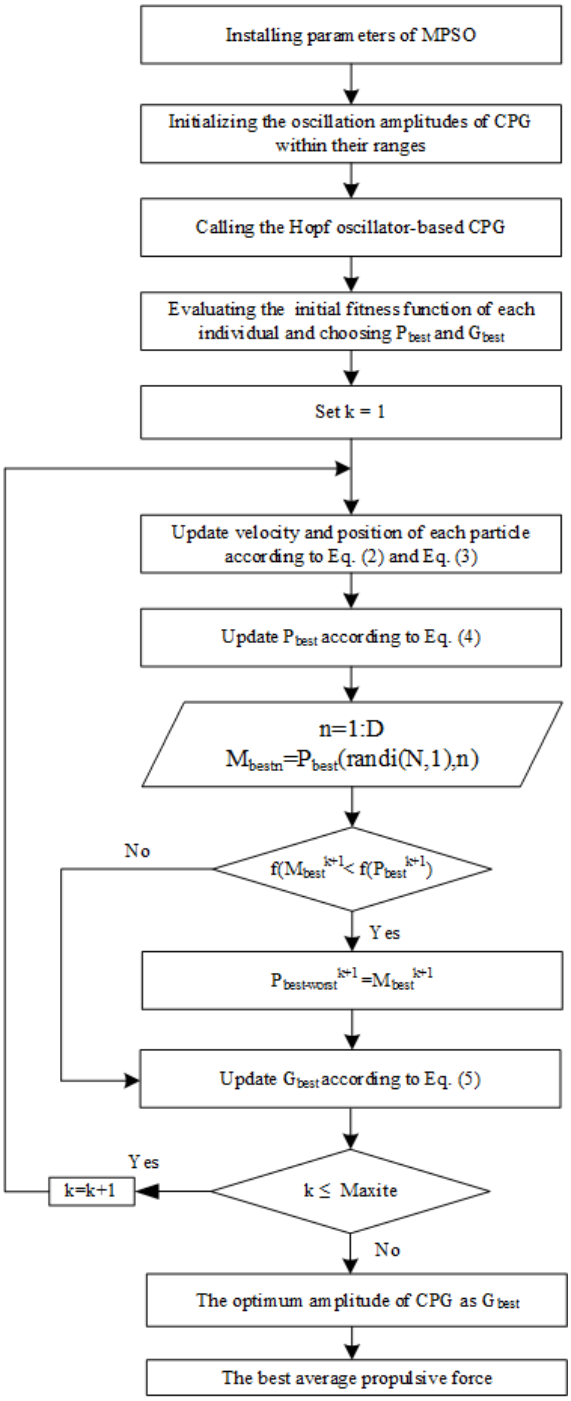

Figure 3. Flowchart of the proposed method

4. Results and Discussions

The proposed MPSO-based CPG method is performed on the elongated undulating fin model simulated in MATLAB. Each joint is driven by a CPG unit, whose amplitude values are randomly chosen in the range of [0 40] degree based on the actual mechanical structure. The output of the CPG model is presented in Fig. 4a and the thrust curve obtained by the Hopf-based CPG outputs is illustrated in Fig. 4b.

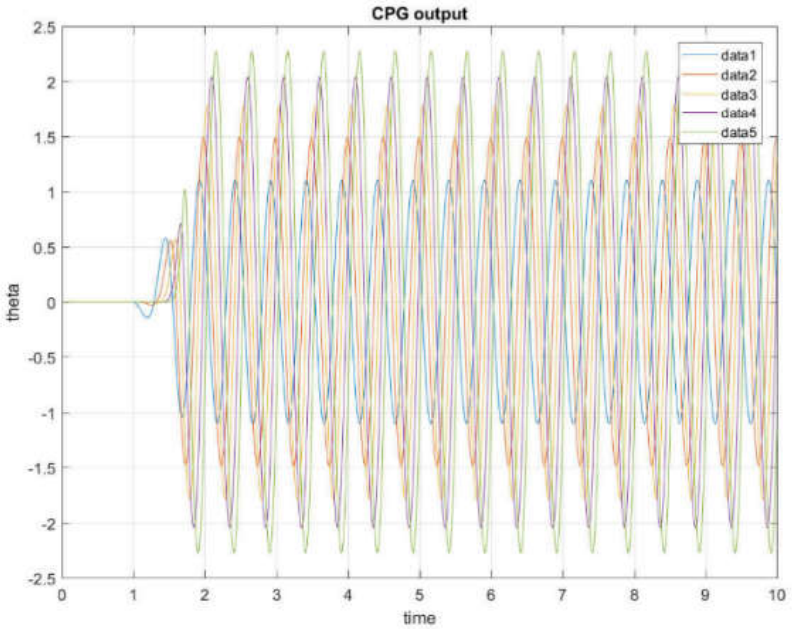

a. The CPG outputs

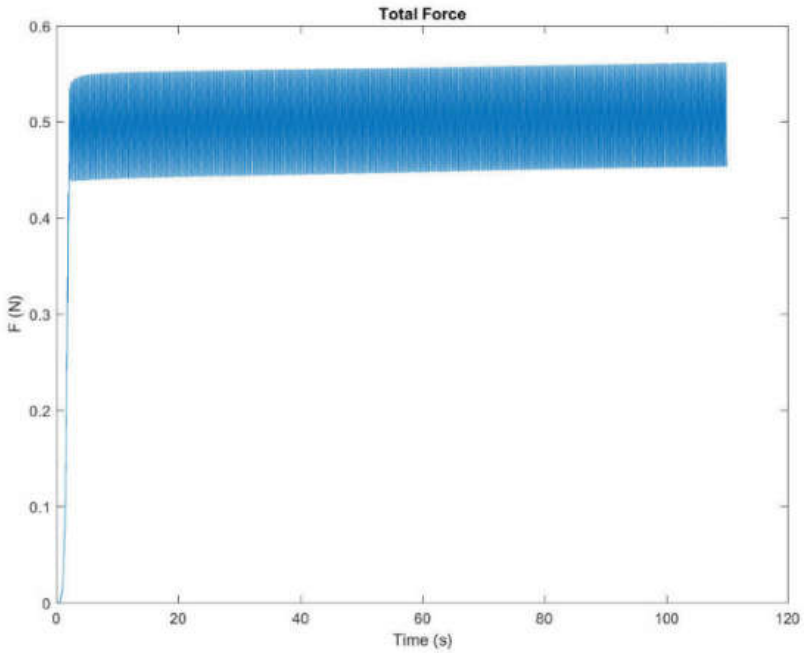

b. The characteristic curve of average thrust

Figure 4. Simulation results with the random values of amplitude

It can see from Fig. 4b that the average push force of sixteen fin-ray systems can reach 0.52 N; however, there is an oscillation around a steady state.

To reach the best performance of CPG units, a new MPSO algorithm is governed for the first time to increase average propulsive force. It is noted that MPSO performed with the swarm size of 10, with the best acceleration coefficients as 2 in the maximum iteration of 1000.

Table 1 gives the average propulsive force of the undulating fin robot with the dynamic model driven by Hopf oscillator-based CPG unit in the case of using Standard CPG and MPSO-based CPG.

Table 1. Optimization results of CPG model with/without MPSO algorithm

Model	A_1	A_2	A_3	A_4	A_5	A_6	A_7	A_8	A_9	A_{10}	A_{11}	A_{12}	A_{13}	A_{14}	A_{15}	A_{16}	F (N)
Standard CPG	1	2	3	4	5	6	7	8	9	10	11	12	13	14	15	16	0.52
MPSO-CPG	1.893	4.625	10.946	15.734	20.447	20.998	21.341	22.443	24.005	26.021	28.834	30	31.923	35	37.253	40	3.61

It can be observed from Table 1 that the average push force before optimization with the randomly chosen parameters is 0.52 N, whereas this value is increased to 3.61 N after using the DPSO-based CPG. According to the constant values of the intrinsic frequency of 2 Hz, the best amplitude parameters of A1-A16 as given in Table 1.

A comparison of fitness curves between PSO-based and MPSO-based CPG during the training process is shown in Fig. 5.

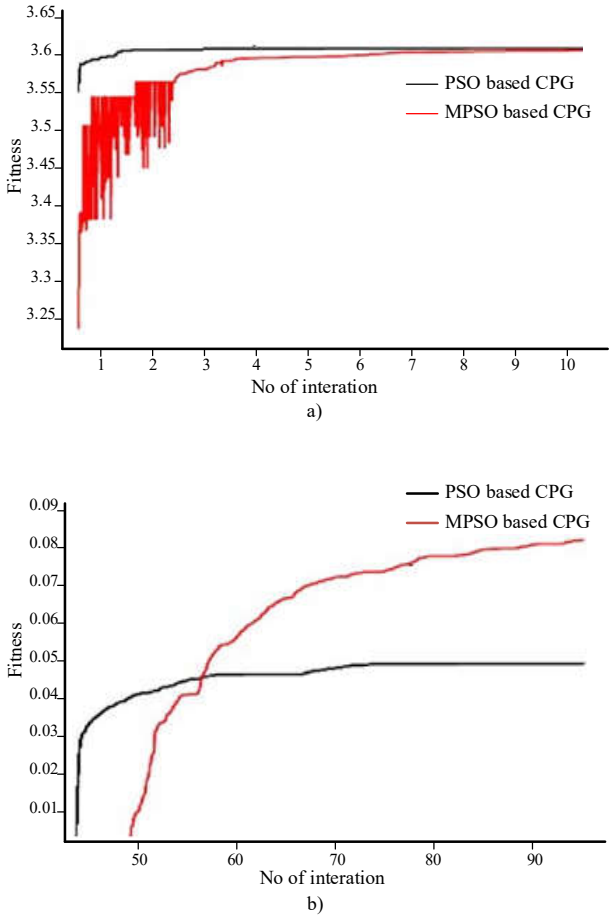

Figure 5. The fitness curves of MPSO-based and PSO-based CPG during training process

From Fig. 5a, it can be seen that some parts of the fitness curve of MPSO-based CPG obviously vibrate but the fitness curve of PSO-based CPG does not, which indicates that the MPSO-based CPG accepted worse solutions sometimes during training and shows its better ability to escape from a local optimum. From Fig. 5b, we find that the MPSO-based CPG finally got a better fitness than the PSO-based CPG, and at the end of the iteration, the MPSO-based CPG still had a tendency to reach better solutions. This was caused by the MPSO technique applied to replace the worst particles. In the other words, the proposed MPSO based-CPG is the ability to achieve the global best position better than the PSO-based CPG.

5. Conclusion

In this paper, a bi-directionally coupled sixteen Hopf oscillator-based CPG network is used to generate the rhythmic movement of the elongated undulating fin robot inspired by the black knifefish. In addition, a novel variant of PSO, namely MPSO has been developed to improve the performance of a modified CPG networks. The MPSO-based CPG model outperforms the classical PSO in both the value of propulsive force and the ability to avoid the local maxima.

Acknowledgment

This research is funded by Vietnam National University Ho Chi Minh City (VNU-HCM) under grant number TX2023-20b-01. We acknowledge the support of time and facilities from National Key Laboratory of Digital Control and System Engineering (DCSELab), Ho Chi Minh City University of Technology (HCMUT), VNU-HCM for this study.

References

1. Low, K. H. Maneuvering of biomimetic fish by integrating a buoyancy body with modular undulating fins. *Int. J. Humanoid Robot* **2007**, *4 (4)*: pp. 671–695.
2. Ren, C. et al. A multi-scale UAV image matching method applied to large-scale landslide reconstruction. *Math. Biosci. Eng* **2021**, *18 (3)*: pp. 2274–2287.
3. Sprague, C. I.; Ozkahraman, O.; Munafo, A.; Marlow, R.; Phillips, A.; Ogren P. Improving the Modularity of AUV Control Systems using Behaviour Trees. AUV 2018 - 2018 IEEE/OES Auton 2018, Underw. Veh. Work. Proc., **2018**.
4. Yu, J.; Ding, R.; Yang, Q.; Tan, M.; Zhang, J. Amphibious pattern design of a robotic fish with wheel-propeller-fin mechanisms. *J. Field Robot* **2013**, *30 (5)*: pp. 702–716.
5. Bliss, T.; Iwasaki, T.; Bart-Smith, H. Central pattern generator control of a tensegrity swimmer. *IEEE/ASME Trans. Mechatronics* **2013**, *18 (2)*: pp. 586–597.
6. Crespi, A.; Lachat, D.; Pasquier, A.; Ijspeert, A. J. Controlling swimming and crawling in a fish robot using a central pattern generator. *Auto. Robots* **2008**, *25 (1–2)*: pp. 3–13.
7. J. Cristiano, D. Puig, M. A. Garcia, Generation and control of locomotion patterns for biped robots by using central pattern generators, Journal of Physical Agents 2017 8(1) pp. 40-47.
8. T. G. Brown, On the nature of the fundamental activity of the nervous centres; together with an analysis of the conditioning of rhythmic activity in progression, and a theory of the evolution of function in the nervous system, J. Physiol. 48 (1) (1914) 18–46.

9. N. Paulose, M. Krishna, S. Purwar, Implementation of CPG based locomotion controller on minimule robot, Int. J. Robot. Mechatron. 1 (1) (2014) doi:10. 21535%2Fijrm.v1i1.80.
10. R. Hagiwara, K. Ishihara, T. Horiuchi, CPG-based locomotion learning of four– legged robot by multi-objective GA, ICIC Express Lett. Part B: Appl. 5 (1) (2014) 103–109.
11. Y. Hu, J. Liang, T. Wang, Parameter synthesis of coupled nonlinear oscillators for CPG-based robotic locomotion, IEEE Trans. Ind. Electron. 61 (11) (2014) 6183–6191.
12. Jose, H. B. Z. Two-phase GA parameter tunning method of CPGs for quadruped gaits. The 2011 International Joint Conference on Neural Networks **2011**.
13. Wang, M.; Dong, H.; Li, X.; Zhang, Y.; Yu, J. Control and Optimization of a Bionic Robotic Fish Though a Combination of CPG and PSO. *Neurocomputing* **2019**, *337*: pp. 144-152.
14. Kennedy, J.; Eberhart, R. C.; Shi, Y. Swarm Intelligence. Morgan Kaufmann, San Francisco, USA, **2001**.
15. Cho, M. Y.; Hoang, T .T. Feature Selection and Parameters Optimization of SVM Using Particle Swarm Optimization for Fault Classification in Power Distribution Systems. *Computational Intelligence and Neuroscience* **2017**.

[O-1-13] Torque Balance of Coaxial BLDC Motor Using Feedback Linearization in Presence of Cogging Torque

Lam Cuong Quoc Thai[1, 2, 3,*], Hoang Long Phan[1, 2, 3], Van Tu Duong[1, 2, 3], Huy Hung Nguyen[4, †], Dae Hwan Kim[5] and Tan Tien Nguyen[1, 2, 3]

[1] National Key Laboratory of Digital Control and System Engineering (DCSELab), Ho Chi Minh City University of Technology (HCMUT), 268 Ly Thuong Kiet Street, District 10, Ho Chi Minh City, Vietnam

[2] Faculty of Mechanical Engineering, Ho Chi Minh City University of Technology (HCMUT), 268 Ly Thuong Kiet, District 10, Ho Chi Minh City, Vietnam

[3] Vietnam National University Ho Chi Minh City, Linh Trung Ward, Thu Duc District, Ho Chi Minh City, Vietnam

[4] Faculty of Electronics and Telecommunication, Saigon University, Vietnam

[5] Realmaker.Inc, R304 B23 Sinseon-ro, Nam-gu, Busan, KS012, Republic of Korea

[†] Leading-Corresponding author: nhhung@sgu.edu.vn

[*] Presenting author: tlcquoc.sdh20@hcmut.edu.vn

Abstract

Ensuring the stability of the coaxial BLDC motor in torque-balance applications is still challenging due to the effects of cogging torque caused by the natural interaction between the permanent magnet and the teeth of stator slot, especially at low speed. This paper presents a solution to mitigate the influences of oscillations without the modification of the electric drives based on the utilization of the nonlinear control technique known as feedback linearization. The advantages of the proposed control method are low cost and straightforward to implement with the microcontroller unit. The effectiveness and robustness of this proposed control are verified through the analysis of simulation results and the comparison with PI control.

Keywords: *Torque balance control, Coaxial BLDC motor, Feedback linearization, Cogging torque*

1. Introduction

The BLDC motor has a great opportunity to become a prevailing force in the market of industrial applications thanks to its inherent outstanding advantages compared to other types of motors such as large torque-speed

characteristic, low noise, high reliability… In applications of thruster for underwater vehicles, this type of motor is designed associated with the dual rotors structure to create the coaxial BLDC motor, which has higher propulsion performance and maintains the stability of system. To obtain the best efficiency of mentioned advantages of the coaxial BLDC motor, two torques produced by two rotors need to be canceled each other. However, one of the disadvantages of BLDC motors is cogging torque, which exists even there is no stator current flowing into the stator windings and is measured based on the reaction torque on stator [1]. This torque is considered as noise because it causes undesirable drawbacks such as audible noise and vibration by which the torque balance control strategy faces the challenge. Therefore, a method need to be considered as a solution to improve the stability of coaxial BLDC motor.

There are two main methods to reduce the effects of cogging torque in BLDC motor operation: hardware and software. Hardware is a reduction method of cogging torque while designing a BLDC motor such as increase of air gap, larger number of slots/pole, thicker tooth tips to prevent saturation, minimizing slot opening, magnetic slot-wedge usage, magnet skewing, magnet pole shaping, addition of dummy slots, and lower magnet flux density [2]–[5]. The comparison of all methods mentioned above is presented in [6] by means of finite element method. The cogging torque reduction by software means that the use of control algorithm is applied to mitigate these drawbacks of cogging torque, and the current controller in field oriented control (FOC) technique is focused to develop. A control method of the phase current proposes a modified current wave form, which is composed of main and auxiliary currents. The auxiliary current is determined by the negative cogging torque at the given rotor position, and the duty ratio is determined by the phase current. Time-stepping finite element analysis of the BLDC motor and a DSP-based BLDC motor controller are performed, and it shows that the proposed method can reduce the cogging torque by approximately 36% as compared with the conventional method [7]. Another method adds dominant harmonics of the cogging torque profile estimated by Fourier series into the q-axis current reference. However, this method can only be sufficient for reduction of cogging torque at low speed, so the current PI controllers in FOC structure are extended by CHC algorithm, which is placed parallel to d-q currents PI controllers [8]. Through the experiment and FFT analysis, the effectiveness of this proposed control technique is experimentally verified by vibrations and acoustic noise measurements.

In this paper, a feedback linearization speed controller based on FOC technique is performed to apply for the torque balance control strategy called master-slave speed tracking. A cogging torque mathematical model by Fourier series is defined to compensate into speed controller and coaxial BLDC motor for reduction of cogging torque in section 2. In section 3, the controller design procedure is implemented. The effectiveness of proposed control technique is verified via the simulation in Matlab in section 4. Finally, some achievement is summarized in section 5.

2. Cogging Torque and Coaxial BLDC Modelling

2.1. Cogging Torque Modelling

In order to minimize the effects of cogging torque, the behavior of cogging torque needs to be considered. [9] A Fourier harmonic analysis is exploited against the mathematical model of cogging torque gained with FEM analysis as the following equation.

$$T_{\text{cog}} \cong \sum_{k=1}^{m} T_k \sin(kZ\omega_m + \alpha_k) \quad (1)$$

where T_k and the α_k are the coefficients of the Fourier harmonic development, Z is the number of stator teeth, ω_m is the angular (mechanical) position of the rotor, and m is the number of harmonics that are used to approximate the actual shape of the cogging torque, T_{cog}.

There are many cogging torque curves corresponding to the number of harmonics m. Figure 6 shows the interpolation results of coefficients shown in Table from the simulation data with $m = 4$, which is sufficient to describe the accuracy and complexity of cogging torque [10]. Coefficients of the cogging torque model shown in Table are used as the cogging term for the coaxial BLDC motor.

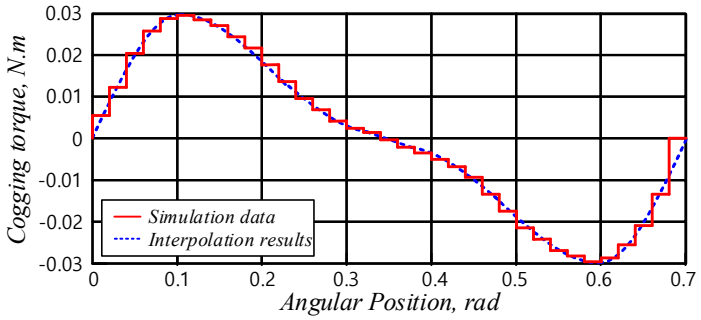

Figure 6. The cogging torque curve with m=4

Table 1. Coefficients of equation (1) from interpolation results

Coefficients	Value	Coefficients	Value
T_1	0.025	α_1	0.009
T_2	0.01	α_2	0.01
T_3	0.001	α_3	0.015
T_4	0.0003	α_4	0.02

2.2. Coaxial BLDC Motor Modeling

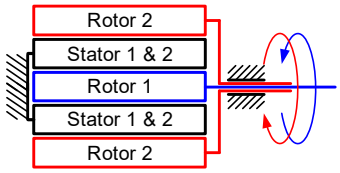

Figure 7. Principle diagram of coaxial BLDC motor

The coaxial BLDC motor has a principle diagram as shown in Figure 7, which has two independent rotors and a common stator. This common stator consists of two windings excited independently by two other inverters. A mathematical model of coaxial BLDC motor can be found by using physical laws [11], [12]. The addition of cogging torque model and the coordinate transformation is necessary for the FOC technique; the mathematic model of one rotor is expressed as follows:

$$\begin{bmatrix} u_d \\ u_q \end{bmatrix} = \begin{bmatrix} R_s & -L_q p\omega_m \\ L_d p\omega_m & R_s \end{bmatrix} \begin{bmatrix} i_d \\ i_q \end{bmatrix} + \begin{bmatrix} L_d & 0 \\ 0 & L_q \end{bmatrix} \begin{bmatrix} \frac{di_d}{dt} \\ \frac{di_q}{dt} \end{bmatrix} + \begin{bmatrix} 0 \\ p\omega_m k_e \end{bmatrix} \quad (2)$$

$$J_m \dot{\omega}_m + \beta\omega_m = T_e + \sum_{k=1}^{m} T_k \sin(kZ\theta_m + \alpha_k) \quad (3)$$

where u_d, u_q are the voltage component in the d-q frame; i_d, i_q are the current components in the d-q frame; L_d, L_d are the inductance transformed; θ_m is the mechanical angular position; $T_e = \frac{3}{2} p k_e i_q$ is the electromagnetic torque.

3. Feedback Linearization Speed Controller

Let $x_1 = i_d, x_2 = i_q, x_3 = \theta_m, x_4 = \omega_m$ as state variables and $u_1 = u_d, u_2 = u_q$ as control variables, equations (2) and (3) are assumed in the state form as the following equation.

$$\dot{x} = \begin{bmatrix} \dot{x}_1 \\ \dot{x}_2 \\ \dot{x}_3 \\ \dot{x}_4 \end{bmatrix} = \begin{bmatrix} p x_4 x_2 - \frac{R_s}{L_{eq}} x_1 \\ -\frac{1}{L_{eq}} \left[R_s x_2 + p x_4 \left(L_{eq} x_1 + k_e \right) \right] \\ x_4 \\ \frac{1}{J_m} \left[\frac{3}{2} p k_e x_2 - \beta x_4 + \sum_{k=1}^{m} T_k \sin(kZ\theta_m + \alpha_k) \right] \end{bmatrix} + \begin{bmatrix} \frac{1}{L_{eq}} \\ 0 \\ 0 \\ 0 \end{bmatrix} u_1 + \begin{bmatrix} 0 \\ \frac{1}{L_{eq}} \\ 0 \\ 0 \end{bmatrix} u_2 \quad (4)$$

Because of speed control, control outputs $y_1 = x_1 = i_d, y_2 = x_4 = \omega_m$ are taken into account. Two control outputs are differentiated in which at least one element of the control vector appears and the linearization condition is inserted by imposing that the i-th derivative is equal to a component of the control vector for the new base $(\dot{y}_1 = v_1; \dot{y}_2 = v_2)$. The following control input is obtained:

$$\begin{cases} u_1 = L_{eq} v_1 + R_s x_1 - p L_{eq} x_4 x_2 \\ u_2 = \frac{2 J_m L_{eq}}{3 p k_e} \left\{ -\frac{1}{J_m} \left\{ \begin{matrix} \frac{3 p k_e}{2 L_{eq}} \left[-R_s x_2 - p x_4 \left(L_{eq} x_1 + k_e \right) \right] + Z x_4 \sum_{k=1}^{4} T_k \cos(Zk x_3 + \alpha_k) \\ -\frac{\beta}{J_m} \left[\frac{3 p k_e x_2}{2} + \sum_{k=1}^{4} T_k \sin(Zk x_3 + \alpha_k) - \beta x_4 \right] \end{matrix} \right\} \right\} + \frac{2 J_m L_{eq}}{3 p k_e} v_2 \end{cases} \quad (5)$$

For tasks involving the tracking of the desired output $[y_{1_d} \quad y_{2_d}]$, the control law is expressed as follows:

$$\begin{cases} v_1 = \dot{y}_{1_d} + k_1 e_1 \\ v_2 = \dot{y}_{2_d} + k_2 e_2 + k_3 \int e_3 dt \end{cases} \quad (6)$$

where $e_1 = i_d - i_{d_d}, e_2 = \omega_m - \omega_{m_d}$ are the tracking error of D-coordinate current and speed k_1, k_2, k_3 are positive constant.

Therefore, the tracking error of the closed-loop system is given by:

$$\begin{cases} \dot{e_1} + k_1 e_1 = 0 \\ \dot{e_2} + k_2 e_2 + k_3 \int e_3 dt = 0 \end{cases} \quad (7)$$

which represents an exponentially stable error dynamic. Therefore, if initially $\dot{e_1}(0) = e_1(0) = 0, \dot{e_2}(0) = e_2(0) = 0$, then $e_{1,2}(t) \equiv 0, \forall t \geq 0$, so the perfect tracking is achieved; otherwise, $e_{1,2}(t)$ converge to zero exponentially.

4. Simulation

4.1. Feedback Linearization Control

A simulation model has been performed to verify the effectiveness of reducing cogging torque of feedback linearization algorithm. These results are compared with PI controllers with coefficients shown in Table and the parameters of motor are referred from [10].

Table 2. Coefficients of controllers

Controller	Coefficients
PI speed and D, Q current	$k_{P_s} = 1, k_{I_s} = 100, k_{P_q} = 10, k_{I_q} = 1,$ $k_{P_d} = 10, k_{I_d} = 1$
Feedback linearization	$k_1 = 1000; k_2 = 2000; k_3 = 40000$

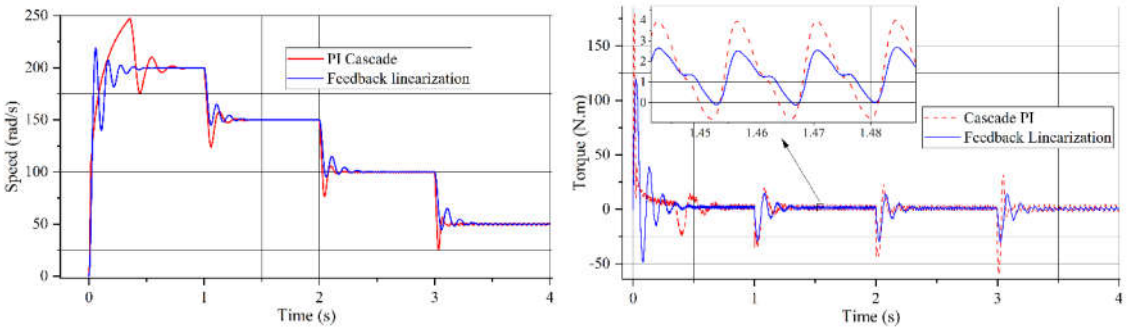

Figure 8. Simulation results of speed (left) and torque (right)

The speed tracking results show that the settling time of two controllers are the same, but the PI controller has larger overshoot of about 25 (rad/s).

In terms of torque, at the time of 1.5 (s) in stable period with the reference speed of 150 (rad/s), the cogging torque of the PI controller has two peaks from -1 to 4 (N.m), while this figure is from 0 to 2.5 (N.m) for the feedback linearization control. It means that this proposed algorithm can reduce about 50% magnitude of the cogging torque for BLDC motor.

4.2. Torque Balance Control

After the verification of effectiveness of the feedback linearization control in reducing the cogging torque, this algorithm is applied for torque balance control applications which have block diagram presented in [12]. The main goal is that the torques produced by two rotors are canceled each other with the opposite direction moving of the main rotor as rotor 2 and the auxiliary rotor as rotor 1.

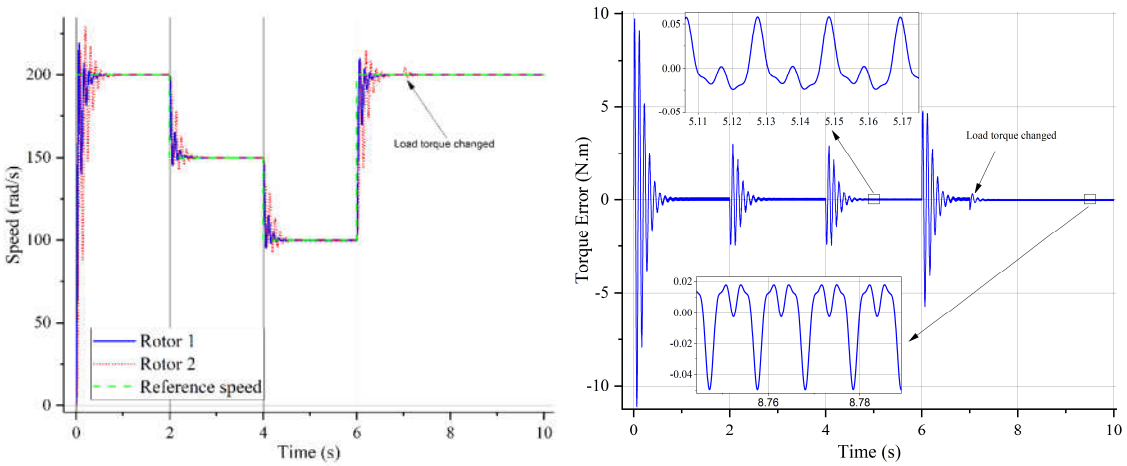

Figure 9. The simulation results of the torque balance strategy, speed (right) and torque error (left)

The simulation result of speed tracking as shown in Figure 9 shows that the speed of rotor 2 has a larger amplitude of fluctuation when compared to that of rotor 1. At the time of 7 (s), when the load torque changed, the speed of rotor 2 has a small oscillation but it tracked the reference speed back quickly.

Because of the oscillation of speed in the start-up period of two rotors, it also causes vacillation of torque in this period. In the stable period, the torque error maintains a small oscillation around equilibrium point with the range of 0.07 (N.m).

5. Conclusion

In this paper, a speed controller based on feedback linearization algorithm is presented to reduce cogging torque and contributes to improving the stability in torque balance applications. The simulation results have proved the effectiveness of 50% cogging torque reduction when compared to PI cascaded controller. Similar to another control algorithm, however, the disadvantage of this algorithm is that the parameters of coaxial BLDC motor, as well as cogging torque model need to be estimated accurately. To conclude, a feedback linearization speed control algorithm is one of feasible method to enhance stability in torque balance applications.

Acknowledgments

This research is funded by Vietnam National University Ho Chi Minh City (VNU-HCM) under grant number TX2023-20b-01. We acknowledge the support of time and facilities from National Key Laboratory of Digital Control and System Engineering (DCSELab), Ho Chi Minh City University of Technology (HCMUT), VNU-HCM for this study.

References

1. Z. Q. Zhu, “A simple method for measuring cogging torque in permanent magnet machines”, *2009 IEEE Power Energy Soc. Gen. Meet. PES ’09*, bll 3–6, 2009, doi: 10.1109/PES.2009.5275665.
2. D. Hanselman, *Brushless permanent magnet motor design*. 2003.
3. J. R. Hendershot en T. J. E. Miller, *Design of Brushless PM motors*, vol 46, no 11. 2016.

4. N. Bianchi en S. Bolognani, “Design techniques for reducing the cogging torque in surface-mounted PM motors”, *IEEE Trans. Ind. Appl.*, vol 38, no 5, bll 1259–1265, 2002, doi: 10.1109/TIA.2002.802989.
5. T. Li en G. Slemon, “Reduction of cogging torque in permanent magnet motors”, *IEEE Trans. Magn.*, vol 24, no 6, bll 2901–2903, 1988, doi: 10.1109/20.92282.
6. T. Srisiriwanna en M. Konghirun, “A study of cogging torque reduction methods in brushless DC motor”, *ECTI Trans. Electr. Eng. Electron. Commun.*, vol 10, no 2, bll 138–144, 2012.
7. G. H. Jang en C. J. Lee, “Design and control of the phase current of a brushless dc motor to eliminate cogging torque”, *J. Appl. Phys.*, vol 99, no 8, bll 3–5, 2006, doi: 10.1063/1.2165603.
8. M. Sumega, P. Rafajdus, en M. Stulrajter, “Current harmonics controller for reduction of acoustic noise, vibrations and torque ripple caused by cogging torque in PM motors under FOC operation”, *Energies*, vol 13, no 10, 2020, doi: 10.3390/en13102534.
9. Tudorache, T., et al., “Improved mathematical model of PMSM taking into account cogging torque oscillations”, *Adv. Electr. Comput. Eng.*, vol 12, no 3, bll 59–64, 2012.
10. P. Dini en S. Saponara, “Cogging torque reduction in brushless motors by a nonlinear control technique”, *Energies*, vol 12, no 11, bll 1–20, 2019, doi: 10.3390/en12112224.
11. L. C. Q. Thai, V. T. Duong, H. H. Nguyen, en T. T. Nguyen, “Integral Action Finite Set Model Predictive Current Control for Brushless DC Motor”, *Lect. Notes Mech. Eng.*, no December, bll 271–285, 2022, doi: 10.1007/978-981-19-1968-8_22.
12. L. C. Q. Thai, V. T. Nguyen, C. T. Doan, V. T. Duong, H. H. Nguyen, en T. T. Nguyen, “Anti-torque Controller Using Sliding Mode Linear Quadratic Regulator Applied for Coaxial BLDC Motor BT - Advances in Engineering Research and Application”, 2023, bll 217–226.

[O-1-14] A Grey Predictor-based Feedforward Controller and Its Application to Force Control of Hydraulics System

Tran Nguyen Duy Phuong[1, *], Tran Duc Thien[2], Truong Quoc Thanh[1], and Dao Thanh Liem[3, †]

[1] Faculty of Mechanical Engineering, HCMC University of Technology, Ho Chi Minh City, 700000, Vietnam

[2] Faculty of Electrical and Electronics Engineering, HCMC University of Technology and Education, Thu Duc City – Ho Chi Minh City, 700000, Vietnam

[3] Faculty of Engineering and Technology, Nguyen Tat Thanh University, Ho Chi Minh City, 700000, Vietnam

[†] Leading - Corresponding author: liemdt@ntt.edu.vn

[*] Presenting author: tqthanh@hcmut.edu.vn

Abstract

Electro-Hydraulic Actuators (EHA) have a wide range of applications where force or position control with high accuracy is exceedingly necessary. However, EHA is a highly complex nonlinear system which made it a challenging and appealing system for modeling and control design. This study presents a force control approach for an EHA system using a combination of a feedforward-based PID (FPID) controller and a grey predictor (GP), shortened as grey predictor-based feedforward PID Controller (GPFPID). The FPID controller is used to drive the system to desired targets. Meanwhile, the GP predictor takes part in estimating the output in the near future to optimize the controller parameters in advance and to create a compensating control signal corresponding to the system perturbations, consequently, improving the control performance. The simulation results have been carried out to investigate the effectiveness of the proposed control approach.

Keywords: *Electro-hydraulic actuator, Feedforward control, Force control, Grey predictor*

1. Introduction

Today, hydraulic systems are considered as a potential option for modern industry due to their durability, high power-to-weight ratio, reliability, and very high power and torque. Due to its efficiency, many experimental systems using electro-hydraulic actuator (EHA) are designed for research purposes to control force or pressure with better performance. Among them, an EHA that switches from high-speed electric to powerful hydraulics, a more energy-efficient way of generating powerful forces has been developed. However, the control of EHA system is very complicated due to the highly complex nonlinearity and very large uncertainty in the system. To overcome the

control problem of complex nonlinear systems, several control strategies have been proposed. The aim of this paper is to design a novel adaptive control method named grey predictor-based feedforward controller (GPFC) for force control of an EHA system. The GPFC approach is constructed from the main control unit, feedforward PID (FPID), and the adaptive grey predictor (AGP) which was developed from the typical single variable first order grey model *GM*(1,1). During the operation, the parameters of PID controller are online optimized with respect to the control error minimization by using the learning mechanism. At the same time, an observation of the historical system responses is input to the AGP to estimate the system behavior in a near future which is different from the present *p* sampling period. Furthermore, this sampling period is online tuned by two fuzzy sets corresponding to the control error and then, called the fuzzy predictor step size. As a result, the overall control performance is significantly improved.

In this configuration, an electrohydraulic actuator, comprising a pump and an additional valve system, driven by a motor, was implemented in this case. The movement of the cylinder is regulated by the speed of the motor. Another EHA diagram is then built and connected to the end effector of the hydraulic cylinder, creating a load for the system. A linear sensor was included to measure the piston rod displacement of the cylinder. In addition, a force sensor was connected in series with the cylinder rod to measure the load force.

2. Controller Design

As presented in the Introduction, the general structure of the GPFC approach comprises two main blocks, the FPID and AGP. The AGP is designed to estimate the system actuation in a near future, $\hat{y}(k+p)$ on which the FPID bases generate the control input signal, for the system to track a desired target. Furthermore, an additive control signal is also provided to compensate for the effects of the noises and disturbances in the next working period.

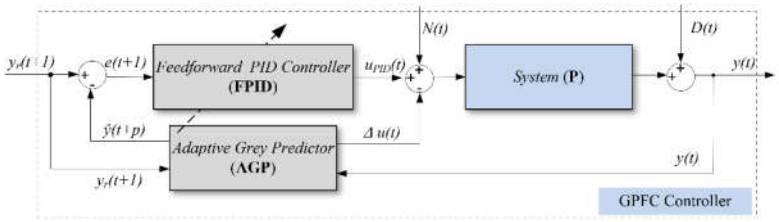

Figure 1. Structure of the GPFC

A. FPID controller design

As mentioned above, the FPID controller consists of two main parts: the neural network-based PID control algorithm to derive the system control input. The control problem is taken into account in a single input and single output system. The main control signal of the system can be obtained in the time domain as below:

$$u(t) = u(t-1) + u_{NN}(t) \tag{1}$$

The $u_{NN}(t)$ can be described as follows:

$$u_{NN}(t) = f(x(t)) = \frac{2\left(1-e^{-x.Y_g}\right)}{Y_g\left(1+e^{-x.Y_g}\right)} \tag{2}$$

where x is the input of the sigmoid function which is computed using the PID algorithm:

$$x(t) = u_{PID}(t) = K_p(t)e_p(t) + K_i(t)e_i(t) + K_d(t)e_d(t) \tag{3}$$

These coefficients K_p, K_i, and K_d are tuned using the back propagation learning algorithm. The PID parameters are updated as below:

$$K_p(t+1) = K_p(t) + \eta_p e_p^2(t)\Delta\frac{4e^{-x.Y_g}}{\left(1+e^{-x.Y_g}\right)^2}; K_i(t+1) = K_i(t) + \eta_i e_p(t) e_i(t)\Delta\frac{4e^{-x.Y_g}}{\left(1+e^{-x.Y_g}\right)^2}; K_d(t+1) = K_i(t) + \eta_d e_p(t) e_d(t)\Delta\frac{4e^{-x.Y_g}}{\left(1+e^{-x.Y_g}\right)^2} \quad (8)$$

Next in order to stabilize the control system, the robust updating rules are implemented into the updating algorithms of the control gains. For robust control approach, there are two control objectives: The first is closed-loop robust stability which must be checked with reasonable margins. The second is closed-loop disturbance attenuation [28].

B. *Adaptive grey predictor design*

In this section, the AGP is designed with two functions: to estimate the system response in a near future, $\hat{y}(t+p)$ which is sent to the FPID controller, and to compensate for the amount of system actuation due to noises and disturbances in the next working period. This AGP contains two inputs – the desired $y_r(t)$ and actual system response $y(t)$ and two outputs - the estimated system response in the near future $\hat{y}(t+p)$ and amount of compensating control signal $\Delta u(t)$. At the same time, the $GM_1(1,1)$ also carries out the predicted system response at present which is sent to the second grey model, $GM_2(1,1)$, to estimate the effect of system noises and disturbances and consequently, produce the corresponding compensating control signal, $\Delta u(t)$. The two outputs are then sent to the proposed control system to perform the closed control loop.

3. Control Performance

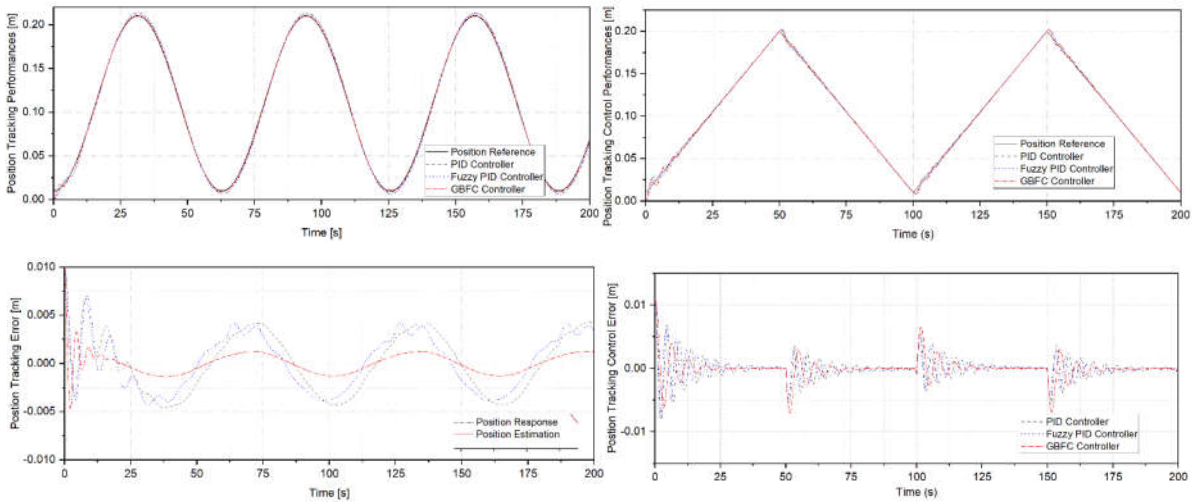

Figure 2. Position tracking performances and control errors with respect to sinusoidal and sawtooth excitation

Numerical simulation with the EHA model has been done to validate the GPFC control performance. Firstly, the comparison between proposed controller and PID and Fuzzy PID controller performances was done with respect to the same reference of sinusoidal signal as drawn in Figure 2. The comparison results as displayed in Figure 2 point out that the proposed controller could drive the cylinder to track the desired position much better than the conventional PID and Fuzzy PID controller. The tracking error is then depicted in Figure 3. The reason is that the

proposed controller possesses both the advantages of the GPFC controller and AGP. As a result, the precise tracking performances were enhanced by the proposed GPFC controller.

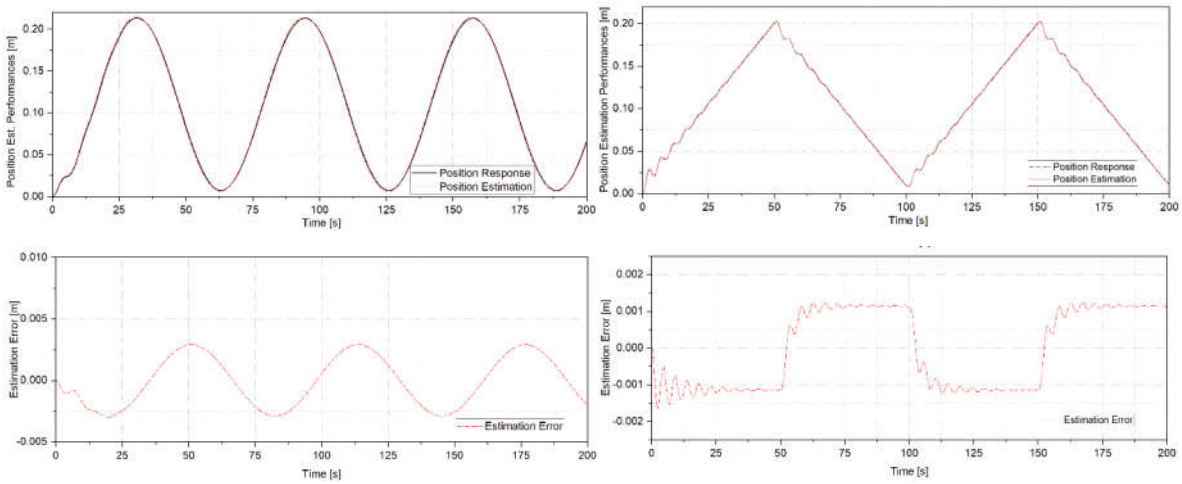

Figure 3. Prediction performance of GP with respect to sinusoidal and sawtooth excitation

4. Conclusion

This paper proposed a novel control method for application to force control of EHA systems. This is based on the modeling method using the adaptive technique, named feedforward neural network fuzzy grey predictor. The GPFC control approach is constructed from the feedforward neural network – based PID controller, and the fuzzy grey predictor. To validate the designed controller, the simulation model using the EHA was built to investigate the GPFC control performance. The comparison results by mean of real-time experiments proved convincingly that the best control performance could be always enhanced by the proposed controller. This method promises a feasible solution for force control of EHA in industrial applications.

References

[1] Tu, D. C. T. and Ahn, K. K., "Nonlinear PID control to improve the control performance of 2 axes pneumatic artificial muscle manipulator using neural network", Mechatronics, Vol. 16, No. 9, pp. 577-587, 2006.

[2] Truong, D. Q. and Ahn, K. K., "Wave prediction based on a modified grey model MGM(1,1) for real-time control of wave energy converters in irregular waves", Renewable Energy, Vol. 43, pp. 242-255, 2012.

[3] Ahn, K. K., Chau, N. H. T. and Truong. D. Q., "Robust force control of a hybrid actuator using quantitative feedback theory", J. of Mechanical Sci. and Technology, Vol. 21, pp. 2048-2058, 2007.

[4] Liem, D. T., Truong, D. Q., Park, H. G., "A feedforward neural network fuzzy grey predictor-based controller for force control of an electro-hydraulic actuator", Int. J. Precis. Eng. Manuf. 17, 309-321, 2016.

[O-1-15] Designing a Meal Support System for the Elderly MSS2023

Nguyen Quang Minh[1, *], Nguyen Duy Phuong Tran[1, †], Duc Thien Tran[2], Thanh Liem Dao[3], Quoc Thanh Truong[1]

[1] Faculty of Mechanical Engineering, HCMC University of Technology, Ho Chi Minh City, 700000, Vietnam
[2] Faculty of Electrical and Electronics Engineering, HCMC University of Technology and Education, Thu Duc City – Hochiminh City, 700000, Vietnam
[3] Faculty of Engineering and Technology, Nguyen Tat Thanh University, Ho Chi Minh City, 700000, Vietnam

[†] Leading - Corresponding author: tnduyphuong@yahoo.com
[*] Presenting author: minh.nguyenquangvnu@hcmut.edu.vn

Abstract

Nowadays, many robots for in-house assistance of the elderly have been trialed and applied. However, these works have many restrictions and also remain unused in real-life scenarios. Hence, this study aims to improve and design a useful system to support the elderly. We will delve into the process of understanding and designing a system that uses robots or many hands to assist the elderly in eating and drinking and can be combined with personal protection, brushing teeth, etc. The system consists of parts such as robot arms, mechanical parts and sensors. The results take out some technical requirements, design-manufacturing and usage applications of the supporting robot for eddy in the near future.

Keywords: *Systems, Robotic arms, Sensors and health*

[O-1-16] Design and Simulation of a Linear-motion Compliant Mechanism

Hai Nhan Le[1, 2, *], Phuc Khanh Nguyen[1, 2], and Minh Tuan Pham[1, 2, †]

[1] Department of Machine Design, Faculty of Mechanical Engineering, Ho Chi Minh City University of Technology (HCMUT), 268 Ly Thuong Kiet Street, District 10, Ho Chi Minh City, Vietnam
[2] National University Ho Chi Minh City, Linh Trung Ward, Thu Duc City, Ho Chi Minh City, Vietnam

[†] Leading - Corresponding author: pminhtuan@hcmut.edu.vn
[*] Presenting author: nhan.le1901@hcmut.edu.vn

Abstract

This paper presents a compact design of compliant mechanism that produces single degree-of-freedom (DOF) for accurate linear motion and large stroke with low input force of below 10N from the linear actuators. Based on the stiffness matrices and relationships between beam-type flexure elements, the analytical model of the entire compliant mechanism is proposed and its mechanical property is clarified. Subsequently, the finite-element-analysis (FEA) is conducted via ANSYS software to verify the actual performance of the compliant mechanism. The good agreement between analytical and simulation results demonstrates the correctness of the proposed design, and it can be employed as a compliant bearing for a precise linear actuator. The obtained results also suggest some ideas to enhance the performance of the designed linear-motion compliant mechanism in terms of working range, stiffness characteristic and positioning accuracy.

Keywords: *Compliant mechanism, Compliant bearing, Linear actuator, Linear motion, Beam-type flexure*

1. Introduction

The linear motion is essential for the function of machines; it may be involved in the control unit, transmission unit, etc. of a device. Nowadays, there are different types of mechanisms - actuators that can provide linear motion. However, current linear actuators such as servo motor with screw shaft, hydraulic cylinder, pneumatic cylinder have poor accuracy with microscale/nanoscale displacement range. Therefore, compliant mechanism is an effective solution with frictionless and highly repeatable linear motions. By taking advantage of elastic deformation of material, the shortcomings of usual mechanisms such as dry friction, backlash, wear and assembly error can be overcome.

There are many types of compliant mechanisms that can be applied to design the compliant bearing such as 1-DOF rotating bearing [1], 2-DOF rotating - translating bearing [2], 3-DOF planar-motion [3-4] and 3-DOF spatial-motion [5-6], etc. For the 1-DOF compliant bearing in this paper, the basic beam structures are used so that the calculation would be simple and alike the actual model. The compliant bearing is constructed by multiple flexures and rigid bodies; their stiffness can be represented by a compound spring system (Peseudo-Rigid Body method). Then, with the input force from the actuator, the output is a pure translational displacement of the bearing; to achieve this, the compliant bearing must have high compliance in desired DOF and high stiffness in other DOFs.

To calculate the stiffness of the compliant bearing as well as to guarantee the correctness of calculated results, both the analytical method [7-8] and finite element analysis (FEA) [7] are used in this work. The remaining of this paper are as follows: Theoretical basis is demonstrated in section II while the bearing model is built up in section III; based on sections II-III, the bearing stiffness matric is calculated in section IV and compared to the simulation results conducted in section V; finally, the section VI will draw a conclusion for this paper.

2. Theoretical Basis

For Hooke's law, the beam element is considered as a spring structure and has the relationship:

$$F = k.x \tag{1}$$

F is Applied force (elastic force) (N)

k is Stiffness of element (Nm)

x is Displacement of element (m)

The inverse of the stiffness is the compliance c -displacement for specific force unit:

$$c = \frac{1}{k} \tag{2}$$

The stiffness matrix of a fixed-end beam element:

$$K_{beam} = \begin{bmatrix} \frac{AE}{L} & 0 & 0 & 0 & 0 & 0 \\ 0 & \frac{12EI_z}{L^3} & 0 & 0 & 0 & -\frac{6EI_z}{L^2} \\ 0 & 0 & \frac{12EI_y}{L^3} & 0 & \frac{EI_y}{L^2} & 0 \\ 0 & 0 & 0 & \frac{GJ}{L} & 0 & 0 \\ 0 & 0 & \frac{6EI_y}{L^2} & 0 & \frac{4EI_y}{L} & 0 \\ 0 & -\frac{6EI_z}{L^2} & 0 & 0 & 0 & \frac{4EI_z}{L} \end{bmatrix} \tag{3}$$

E is Young's modulus (MPa).

G is Shear modulus (MPa).

A is Cross-sectional area (m^2).

I_y is Inertia moment about y axis (m^4).

I_z is Inertia moment about z axis (m^4).

J is Torsion constant (m^4).

The compliance matrix of the beam element:

$$C_{beam} = {K_{beam}}^{-1} \tag{4}$$

When calculating the beam stiffness, the free end of each beam is the origin of a local coordinate system (Fig. 1); then, to calculate the stiffness matrices of many beams, it is necessary to transform all local coordinate systems into one global coordinate system. The global origin of a bearing's coordinate system is at the center point of the shaft hole. For each beam, the stiffness matrices can be different based on the transformation matrices: Rotating about Z axis, translating along X-Y-Z axis.

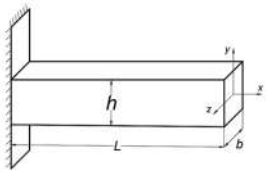

Figure 1. The model of fixed-end beam

The stiffness matrix after rotating about Z axis:

$$K_R = R_z K_{beam} {R_z}^{-1} \tag{5}$$

R_z is the rotation matrix about Z axis of beam element.

${R_z}^{-1}$ is the inverse matrix of R_z.

$$R_z = \begin{bmatrix} cos\theta & -sin\theta & 0 & 0 & 0 & 0 \\ sin\theta & cos\theta & 0 & 0 & 0 & 0 \\ 0 & 0 & 1 & 0 & 0 & 0 \\ 0 & 0 & 0 & cos\theta & -sin\theta & 0 \\ 0 & 0 & 0 & sin\theta & cos\theta & 0 \\ 0 & 0 & 0 & 0 & 0 & 1 \end{bmatrix} \tag{6}$$

θ is the rotating angle of beam about Z axis (rad).

The stiffness matrix after translating along X-Y-Z axis:

$$K_T = J_k K_{beam} {J_k}^T \tag{7}$$

J_k is the translation matrix of stiffness matrix.

${J_k}^T$ is the transposition matrix of J_k.

$$J_k = \begin{bmatrix} 1 & 0 & 0 & 0 & 0 & 0 \\ 0 & 1 & 0 & 0 & 0 & 0 \\ 0 & 0 & 1 & 0 & 0 & 0 \\ 0 & R_z & -R_y & 1 & 0 & 0 \\ -R_z & 0 & R_x & 0 & 1 & 0 \\ R_y & -R_x & 0 & 0 & 0 & 1 \end{bmatrix} \quad (8)$$

R_x is the displacement along X axis (m).

R_y is the displacement along Y axis (m).

R_z is the displacement along Z axis (m).

The synthesis for the serial beams and parallel beams is similar to the springs (Fig. 2) and expressed by the Table 1.

(a) *(b)*

Figure 2. Serial springs (a) and parallel springs (b)

Table 1. Stiffness matrices of serial-parallel beams

	Serial beams	**Parallel beams**
Stiffness matrix	$\frac{1}{k} = \frac{1}{k_1} + \frac{1}{k_2}$	$k = k_1 + k_2$
Compliance matrix	$c = c_1 + c_2$	$\frac{1}{c} = \frac{1}{c_1} + \frac{1}{c_2}$

3. Bearing Model

The actuator needs to use two compliant bearings for two ends. For each bearing, there are 4 legs (parallel relationship) so that the bearing has a symmetric structure (Fig. 3) and this results in a symmetric stiffness matrix. Each leg consists of basic beam elements that have serial relationship.

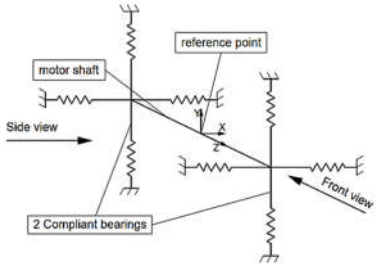

Figure 3. Two compliant bearings in global coordinate system

By considering the compliant mechanisms, desired DOF, machining method, size of workpiece, etc., the compliant bearing model structure is determined and expressed in Fig. 4.

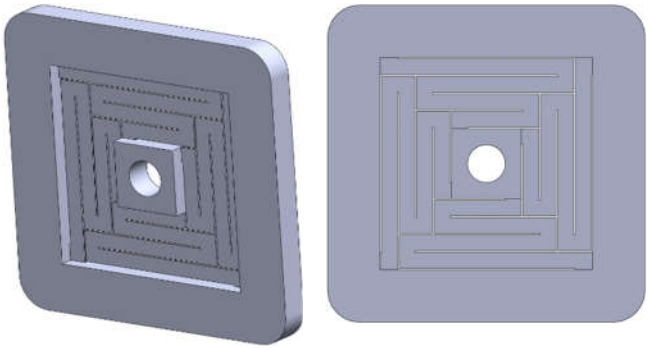

Figure 4. The 3D model of compliant bearing

For the bearing material, aluminum alloy 6061 is selected to have high yield strength for large deformation. Then, the physical parameters of material are listed in Table 2.

Table 2. Parameters of a6061 T6

Aluminum plate 6061 T6	
Young's modulus	$E = 69 \times 10^9$ N/m^2
Density	$D = 2700$ kg/m^3
Poisson coefficient	$p = 0.33$
Shear modulus	$G = 259 \times 10^8$ kg/m^3

For the thickness of the beam, the bearing will have higher deformation if each basic beam of one leg has smaller thickness; to be appropriate for the standard aluminum plate, the thickness of the beam would be: $b = 0.5$mm. For the width of the beam; this dimension would be: $h = 5$ mm.

For the length of each beam, to achieve the best deformation; the length of each beam is increased from the inner hole to the outer flange. Besides, the distance between two beams is determined by the machining method: EDM (Electrical Discharge Machining) wire cutting; therefore, the distance is $s = 0.5$mm. Overall, from the width of beams and the distance s, the length of each beam is determined: $L_1 = 53$mm, $L_2 = 44.5$mm, $L_3 = 33.5$mm, $L_4 = 22.5$mm, $L_5 = 3$mm.

The boundary dimensions of the bearing must be appropriate to the voice coil actuator: 100x100x100mm. Then, all of the bearing dimensions are expressed in Fig. 5.

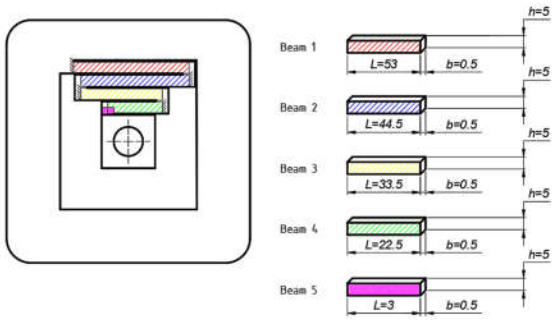

Figure 5. The calculation model for 1 leg

4. Stiffness Matrix Calculation

A. Leg calculation

The parameters that are similar for all 5 beams:

Cross-sectional area:

$A = b \times h = 0.0005 \times 0.005 = 0.0000025$ m^2

Moment of inertia about y axis:

$$I_y = \frac{b^3 \times h}{12} = \frac{0.0005^3 \times 0.005}{12} = 5.2083 \times 10^{-14} m^4$$

Moment of inertia about z axis:

$$I_z = \frac{b \times h^3}{12} = \frac{0.0005 \times 0.005^3}{12} = 5.2083 \times 10^{-11} m^4$$

Torsion constant:

$$I_y = \frac{b^3 \times h}{3} = \frac{0.0005^3 \times 0.005}{3} = 2.0833 \times 10^{-13} m^4$$

In this section, each beam of 1 leg is analysed. For the first beam, the length L_1 is substituted into the stiffness matrix of a fixed end beam element *(9)* to archive the matrix stiffness of this beam in local coordinate system. Then, to transform this matrix from local to global coordination, the translation distances along x-y-z axis are substituted into the translation matrix *(8)* and the formula *(7)*. For the remaining beams, the calculation process is similar; however, with beam 2-4-5, before translating the coordinate system, the local coordination must be rotated about z axis first by rotation matrix *(6)* and formula *(5)*. The translating distance and rotating angle for each beam is listed in Table 3.

Table 3. Translating distances and rotating angles about z axis

	R_x (m)	R_y (m)	R_z (m)	θ (°)
Beam 1	-0.0250	-0.0350	0	0
Beam 2	0.0195	-0.0250	0	180
Beam 3	-0.014	-0.0195	0	0
Beam 4	0.0085	-0.0140	0	180
Beam 5	0.0085	-0.0110	0	90

The corresponding compliance matrices of beams are also determined by the formula *(4)*. Every leg of the compliant bearing consists of 5 serial beams with one end fixed to the outer flange; then the compliance matrix of 1 leg:

$$C_{leg1} = C_{1c} + C_{2c} + C_{3c} + C_{4c} + C_{5c}$$

C_{ic} is the compliance matrix of beam i.

The stiffness matrix K_{1leg} of 1 leg would be achieved by the inverse matrix of compliance matrix:

$$\begin{bmatrix} 6.0816 \times 10^4 & 219.3424 & 0 & 0 & 0 & -1.4576 \times 10^3 \\ 219.3424 & 1.4661 \times 10^4 & 0 & 0 & 0 & -9.5170 \\ 0 & 0 & 126.6796 & 3.0182 & 0.0300 & 0 \\ 0 & 0 & 3.0182 & 0.1067 & 7.1428 \times 10^{-4} & 0 \\ 0 & 0 & 0.0300 & 7.1428 \times 10^{-4} & 0.0235 & 0 \\ -1.4576 \times 10^3 & -9.5170 & 0 & 0 & 0 & 37.2685 \end{bmatrix}$$

B. Bearing calculation

From the above calculated stiffness matrix K_{1leg}, the other 3 legs' stiffness matrices are determined by the rotational transformation about z axis of global coordinate system *(6)* and formula *(5)*. The first leg is assumed that it is at the position 0º; then the rotational angles for remaining legs are:

$$\theta_{leg2} = 90^o;\ \theta_{leg3} = 180^o;\ \theta_{leg4} = 270^o$$

After finding the stiffness matrix of each leg, with the parallel relationship of 4 legs, then the stiffness matrix of 1 compliant bearing will be:

$$K_{bearing1} = K_{leg1} + K_{leg2} + K_{leg3} + K_{leg4}$$

$$K_{bearing1} = \begin{bmatrix} 1.5095 \times 10^5 & 0 & 0 & 0 & 0 & 0 \\ 0 & 1.5095 \times 10^5 & 0 & 0 & 0 & 0 \\ 0 & 0 & 506.7184 & 0 & 0 & 0 \\ 0 & 0 & 0 & 0.2603 & 0 & 0 \\ 0 & 0 & 0 & 0 & 0.2603 & 0 \\ 0 & 0 & 0 & 0 & 0 & 149.0740 \end{bmatrix}$$

Then the compliance matrix for 1 bearing is:

$$C_{bearing1} = \begin{bmatrix} 1.5095 \times 10^5 & 0 & 0 & 0 & 0 & 0 \\ 0 & 1.5095 \times 10^5 & 0 & 0 & 0 & 0 \\ 0 & 0 & 506.7184 & 0 & 0 & 0 \\ 0 & 0 & 0 & 0.2603 & 0 & 0 \\ 0 & 0 & 0 & 0 & 0.2603 & 0 \\ 0 & 0 & 0 & 0 & 0 & 149.0740 \end{bmatrix}$$

C. Motor with two compliant bearings calculation

For the motor model, each end of it will have 1 compliant bearing fixed to the stator; based on the first bearing calculated, the second bearing stiffness matrix will be calculated by translating its coordination a distance L_{motor} = 67mm along z axis (length of the actuator). For the stiffness matrix of the whole motor, it will take the sum of the stiffness matrices of 2 bearings due to the parallel relationship:

$$K_{motor} = K_{bearing1} + K_{bearing2}$$

$$\begin{bmatrix} 3.0191 \times 10^5 & 0 & 0 & 0 & 1.0114 \times 10^7 & 0 \\ 0 & 3.0191 \times 10^5 & 0 & 1.0114 \times 10^7 & 0 & 0 \\ 0 & 0 & 1.0134 \times 10^3 & 0 & 0 & 0 \\ 0 & 1.0114 \times 10^7 & 0 & 6.7763 \times 10^8 & 1.1738 \times 10^8 & 0 \\ 1.0114 \times 10^7 & 0 & 0 & -1.1738 \times 10^8 & 6.7763 \times 10^8 & 0 \\ 0 & 0 & 0 & 0 & 0 & 298.1481 \end{bmatrix}$$

5. FEM Simulation - Comparison

For the simulation, the outer faces of the bearing flange are fixed, the forces are acted along x-y-z axis and the moments are about these axes. The magnitude for each force is 1N, moment is 1Nmm. The deformation in each case is also the corresponding compliance in the calculated compliance matrix of bearing. Displacement and maximum stress of desired DOF (translation along z axis) are expressed in Fig. 6 and Fig. 7.

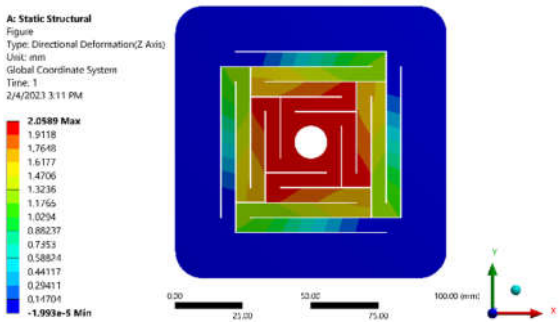

Figure 6. The bearing displacement under the acting of 1N force along z axis

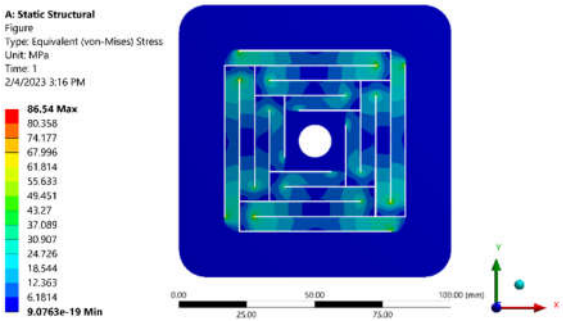

Figure 7. The bearing stress under the acting of 1N force along z axis

From the stress result in Fig.7, the allowable maximum load for 1 compliant bearing can be determined by:

$$F_{\text{max\_1bearing}} = 1\text{N} \times \frac{276\text{MPa}}{86.54\text{MPa}} = 3.1893\ \text{N}$$

Then for 2 bearings of a motor, the maximum load increases two times: $F_{\max} = 3.1893 \times 2 = 6.3785$ N

To identify the stroke of the bearing, it is equal to:

$$Stroke = 2.0589 \times \frac{276\text{MPa}}{86.54\text{MPa}} = 6.5664\ \text{mm}$$

From the simulation results and the compliance matrix, the comparison between FEM and analytical method is expressed in Table 4.

Table 4. The error between fem and analytical method

Compliance / Method	C_x (m/N)	C_y (m/N)	C_z (m/N)	$C_{\theta x}$ (rad/Nmm)	$C_{\theta y}$ (rad/Nmm)	$C_{\theta z}$ (rad/Nm)
Analytical model	6.62×10^{-6}	6.62×10^{-6}	1.97×10^{-3}	3.84×10^{-3}	3.84×10^{-3}	0.0067
FEM	7.23×10^{-6}	7.23×10^{-6}	2.06×10^{-3}	3.81×10^{-3}	3.81×10^{-3}	7.17×10^{-3}
Error (%)	**9.22**	**9.22**	**4.57**	**0.69**	**0.86**	**7.07**

6. Conclusion

From the Table 4, 9.22% is the highest error between two methods, which is acceptable. The difference between analytical model and FEM results is mainly caused by the principle of each method: For the analytical method, only the deformation for basic beam structures is considered while the rigid bodies are neglected; for the FEM, the compliant bearing model is calculated by computer and the accuracy of the calculation depends on the size of each element of the meshing model.

From the above stroke and load, the gain between input force and output displacement can be considered as linear characteristic with the slope ≈ 1; then, this characteristic can reduce the burden of linearization for control system.

Acknowledgment

We acknowledge Ho Chi Minh City University of Technology (HCMUT), VNU-HCM for supporting this study.

References

[1] Xu, Q.: Design of a large-range compliant rotary micropositioning stage with angle and torque sensing. IEEE Sensors Journal **15**, pp. 2419-2430 (2015).

[2] Minh Tuan Pham, Van Tu Nguyen, Minh Tuan Nguyen: Design of a compliant bearing for linear-rotary motor. Advances in Asian Mechanism and Machine Science, pp. 246-257 (2022).

[3] Kim, H., Gweon, D.: Development of a compact and long range XYθz nano-positioning stage. Review Scientific Instrument **83**, 085102 (2012).

[4] Bhagat, U., Shirinzadeh. B., Clark, L.: Design and analysis of a novel flexure-based 3-DOF mechanism. Mechanism and Machine Theory **74**, pp. 173-187 (2014).

[5] Tanikawa, T., Arai, T., Koyachi, N.: Development of small-sized 3 DOF finger module in micro hand for micro manipulation. In: Proceedings of IEEE/RSJ International Conference on Intelligent Robots and Systems, vol. 2, pp. 876-881 (1999).

[6] Xiao, X., Yangmin, L.: Development and control of a compact 3-DOF micromanipulator for high-precise positioning. In: 2014 IEEE/ASME International Conference on Advanced Intelligent Mechatronics, pp. 1480-1485 (2014).

[7] Xu, G., Qu, L.: Some analytical problems of high performance flexure hinge and micro-motion stage design. In: Proceedings of IEEE International Conference on Industrial Technology, China, pp. 771-776. IEEE (1996).

[8] Simaan, N., Shoham, M.: Stiffness synthesis of a variable geometry six-degrees-of-freedom double planar parallel robot. Int. J. Robot. Res. **22**, 757-775 (2003).

[O-2-1] Secure Wireless Communications at UVC Bands: A Review

Yeon Ho Chung[1, *, †], Sudhanshu Arya[2]

[1] Dept. of Information and Communications Engineering, Pukyong National University, Busan, Korea

[2] Artificial Intelligence Research Center, Pukyong National University, Busan, Korea

[†] Leading - Corresponding author: yhchung@pknu.ac.kr

[*] Presenting author: yhchung@pknu.ac.kr

Abstract

Optical wireless communications (OWCs) have gained much attention due to their capability of over 10Gbps data rate and a very low error rate of 3.8 $x10^{-3}$. As new deep ultraviolet LEDs have been developed together with solar-blind detectors, ultraviolet communications (UVC) is a driving force as a new paradigm of OWC. UVC relies mainly on scattering and reflection by the particles and aerosols floating in the air. The transmission distance can be up to a few kilometers. As such, UVC has an outstanding advantage of non-line-of-sight transmission capability by bypassing some obstacles. In particular, UV radiation is solar-blind at wavelengths of 200 to 280nm. Due to the significant power drop with the transmission distance, it can be an ideal option for short-range communication. Some potential applications are underwater communication, vehicular communication, and machine-to-machine communication. In addition, battlefield applications and aircraft guidance systems can be envisioned with UVC in the future.

In this report, we carefully take a close look at recent developments in UVC technologies and relevant implementations. First, we review some important channel models and their distributions to characterize atmospheric turbulence. To extend the transmission distance, some relay techniques are sought as the transmission power drops exponentially with increasing distance. With UVC, the first-of-its-kind application to indoor environments is introduced with an important constraint of the transmit power. Moreover, one important application can be considered vehicle-to-vehicle (V2V) communication. One experimental study was reported. We will closely look into the V2V application and its potential for UVC commercialization in a cost-effective manner. Finally, conclusions are drawn with future research directions on UVC technologies.

Keywords: *Ultraviolet wireless communications, Optical wireless communications, Non-line-of-sight, Secure communications*

[O-2-2] HMM with Hybrid Output Models in Geometric and Gamma Distributions

Bong-Kee Sin[†, *]

Pukyong National University, Yongsoro 45, Nam-ku, Busan, 48513, Republic of Korea

[†] Leading - Corresponding author: bkshin@pknu.ac.kr
[*] Presenting author: bkshin@pknu.ac.kr

Abstract

The standard HMM is given as a parameter triple $\lambda = (\pi, A, B)$, where each element describes a probability distribution: initial transition, state transition, and observation, respectively. This paper presents a novel variant of the discrete-output HMM that is particularly suited for online handwriting recognition where an input is given as a sequence of pen-down or 'inked' strokes and with intermediate pen-up moves. In the standard discrete HMM, an input sequence of symbols, $X = x_1,..., x_T$ is described as a sequence of segments of length, $\tau = (t_1, ..., t_K)$, where $K \leq T$, and t_k, $1 \leq k \leq K$, is the length of the k-th segment, a subsequence of symbols. This segment is then modeled as an independent random process ignorant of length variations, that is, a geometric distribution. When pen-up moves are also explicitly encoded into a sequence of symbols, each will be given as a simple repetition of a particular symbol, with its length following a characteristic distribution. In this paper, the length of pen-up segment is characterized by a gamma distribution. Since a set of gamma densities are assigned to only pen-up move features, the emission probabilities of the HMM are duly called 'hybrid'. This paper gives a theoretical presentation of the proposed HMM with a training algorithm based on expectation-maximization that is guaranteed to improve the model parameters. It is implemented and tested to exhibit improved performance in dealing with letter and character boundaries which usually correspond to pen-up moves.

Keywords: *Hidden Markov model, HMM, Gamma distribution, Training algorithm, Online handwriting recognition*

[O-2-3] Self-energy Recycling in AF Multi-relay Full-duplex Networks: Performance Analysis

Tan N. Nguyen[1, †, *], Phuong T. Tran[2], Lam Thanh-Tu[1]

[1] Communication and Signal Processing Research Group, Faculty of Electrical and Electronics Engineering, Ton Duc Thang University, Ho Chi Minh City, Vietnam
[2] Wireless Communications Research Group, Faculty of Electrical and Electronics Engineering, Ton Duc Thang University, Ho Chi Minh City, Vietnam

[†] Leading - Corresponding author: nguyennhattan@tdtu.edu.vn
[*] Presenting author: nguyennhattan@tdtu.edu.vn

Abstract

Full-duplex communication offers enhanced spectral efficiency for relay deployment, but suffers from the inherent self-interference from the strong transmit signal coupling to the sensitive receive chain. In this paper, we propose a self-energy recycling (S-ER) protocol for full-duplex multi-relay networks, in which the energy from self-interference is harvested back at the relay for future use. Furthermore, two amplify-and-forward (AF) relay selection algorithms, namely, partial relay selection (PRS) and full relay selection (FRS) are introduced to enhance the reliability of the proposed systems. For PRS, the best relay is selected based on just the knowledge of the channels from the source to all relays, while in FRS, the best relay is selected based on the end-to-end signal-to-noise ratio, which requires knowledge of all source-relay and relay- destination links. We provide a thorough analysis on the outage performance of the proposed algorithms in both cases: all channel gains are independently but non-identically distributed (i.n.d.) (case 1) or independently, identically distributed (i.i.d.) (case 2) Rayleigh random variables. It is shown that SER and FRS can significantly enhance the performance of FD networks and avoid the outage floor when the number of relays increases, while the outage probability (OP) in PRS case reaches an outage floor. In addition, the end-to-end signal-to-noise ratio in both cases can be minimized if an optimal power-splitting factor is selected. All analytical results are verified by Monte Carlo simulation.

Keywords: *Full-duplex, Full relay selection, Non-identically distributed, Outage probability, Partial relay selection, Self-energy recycling*

[O-2-4] Microwave and Millimeter-wave Reconfigurable Antenna for 5G Smart Wireless Applications

Truong Khang Nguyen[1, 2, †,*], Dao Tran Khanh Ninh[2], Cong Danh Bui[3]

[1] Division of Computational Physics, Institute for Computational Science, Ton Duc Thang University, Ho Chi Minh City, Vietnam

[2] Faculty of Electrical and Electronics Engineering, Ton Duc Thang University, Ho Chi Minh City, Vietnam

[3] CONNECT Centre, School of Computer Science and Statistics, Trinity College Dublin, Dublin, Ireland

[†] Leading - Corresponding author: nguyentruongkhang@tdtu.edu.vn

[*] Presenting author: nguyentruongkhang@tdtu.edu.vn

Abstract

Frequency bands for 5G New Radio are separated into two different frequency ranges which include sub-6 GHz frequency band and frequency bands from 24.25 GHz to 52.6 GHz, i.e., millimeter-wave (mmWave) band. In sub-6 GHz band, Cognitive Radio (CR) has emerged as an enabling technology for dynamic, efficient, and flexible spectrum utilization. Particularly, Reconfigurable Antenna (RA) designs in CR system architecture are crucial for either sensing/monitoring or transmitting/communicating functions that can effectively switch its operation between two operating modes. In another hand, mmWave band typically demands exchanging a huge amount of data with small latency while still having reduced size and improved energy efficiency. In addition, reconfigurability in radiation and/or polarization is essential to improve the D2D (device-to-device) communication quality which has to be handled specially in dynamically changing and harsh industrial environments. Therefore, MIMO (multi-input-multi-output) RA in mmWave band has recently attracted the interest of researchers in both academics and industry fields. In this talk, I will present the RA techniques used in microwave and mmWave bands which aims to propose a mmWave MIMO Reconfigurable Antenna based on SIW (Substrate-Integrated-Waveguide) cavity to solve the above-mentioned challenges.

Keywords: *Microwave, Millimeter-wave, Reconfigurable antenna, 5G, Wireless communication*

[O-2-5] A Study of Artificial Neural Network for Fault Location on Power Distribution Grids

Dang Luu Ngo[1, *], Hoang Dung Nguyen[1], Duc Thang Nguyen[2], Hung Nguyen[3], Long Dinh Nguyen[4], Anh Duc Le[4], Dae Hwan Kim[5], Thinh Nguyen Tran[6]

[1] Ho Chi Minh City University of Technology, 268 Ly Thuong Kiet Street, District 10, Ho Chi Minh City, 700000, Vietnam

[2] Ho Chi Minh City University of Science, 227 Nguyen Van Cu Street, District 5, Ho Chi Minh City, 700000, Vietnam

[3] HUTECH University, 475A Dien Bien Phu, Binh Thanh District, Ho Chi Minh City, 700000, Vietnam

[4] Dong Nai University, 9 Le Quy Don, Bien Hoa, Dong Nai, 810000, Vietnam

[5] Realmaker.Inc, R304 B23 Sinseon-ro, Nam-gu, Busan, KS012, Republic of Korea

[6] People's Committee of Thu Duc City, 168 Truong Van Bang, Thu Duc City, Ho Chi Minh City, 700000, Vietnam

[†] Leading - Corresponding author: dangluungo2019@gmail.com

[*] Presenting author: dangluungo2019@gmail.com

Abstract

A smart grid is an electrical grid system that makes use of information technology and digital communication to optimize the transmission and distribution of electricity. Smart grid technology has been applied in many countries around the world but has not been widely deployed in Vietnam. The main reason is that locating an electrical grid fault is done manually, which takes a long time and leads to high costs and difficulty in implementation. In this paper, we conduct a study on automation fault isolation and smart grid recovery by applying Artificial Intelligence (AI) as a support tool. A smart grid model is built to predict load and loading station fault RTU, and then the troubleshooting measures are given based on the data received from the model. The experiment is performed on a typical loop, using PSCAD software to simulate the operation and troubleshooting of the grid. The proposed model guarantees reliable loop operation. Simultaneously, it helps to process, isolate the fault, and restore grids faster than the old model, so it ishighly applicable. Our approach has obtained the exact results of the proposed model, which is considered to apply to the electric distribution grids of Thu Duc Corporation.

Keywords: *Smart grid, Typical loop, Fault location, Fault isolation, Fault recovery, RTU, Artificial intelligence*

[O-2-6] On the Physical Layer Security of RIS-assisted Dual-hop Asymmetric Networks

Lam-Thanh Tu[1, †, *], Tan N. Nguyen[1], Phuong T. Tran[2]

[1] Communication and Signal Processing Research Group, Faculty of Electrical and Electronics Engineering, Ton Duc Thang University, Ho Chi Minh City, Vietnam

[2] Wireless Communications Research Group, Faculty of Electrical and Electronics Engineering, Ton Duc Thang University, Ho Chi Minh City, Vietnam

[†] Leading - Corresponding author: tulamthanh@tdtu.edu.vn

[*] Presenting author: tulamthanh@tdtu.edu.vn

Abstract

Recently, physical-layer security (PLS) has emerged as one of the most effective technologies to achieve information-theoretic security against eavesdropping attacks. The main idea of PLS is to exploit the physical characteristics of the wireless channel for securely transmitting messages and was pioneered by Prof. Wyner in 1975. Besides, another novel technology named reconfigurable intelligent surface (RISs) technology is regarded as one of the promising ways to scale up both spectral efficiency (SE) and energy efficiency (EE) of wireless networks. More precisely, RISs consists of near-passive elements that are able to reconfigure the incident signal through passive beamforming, which controls the phase of the signal. As a result, this unveils an efficient way to control the radio waves to extend the coverage area by overcoming physical obstacles and increasing the data rate by taking advantage of the scaling law of RIS received power.

In the present paper, we ameliorate the PLS performance with the assistance of a RIS. Particularly, the main contributions and novelties of this manuscript are summarized as follows:

i) We consider a dual-hop asymmetric wireless network with the help of a RIS.

ii) We address the performance of the secrecy outage probability (SOP) and the average secrecy rate (SR). The SOP is defined as the probability that the SR is below a predefined rate while SR is the maximal achievable rate that is securely transmitted.

iii) We investigate the impact of the number of phase-shift of RIS on the performance of both SOP and SC.

iv) The behavior of the SOP and SC with respect to the transmit power is figured out as well.

Keywords: *Asymmetric channels, Physical layer security, Reconfigurable intelligent surface, Secrecy outage probability, Secrecy rate*

[O-2-7] A Modified Kalman Speed Observer for Sensorless Control of Induction Motor

Nguyen Quang Dung[*, †], Vo Huu Hau

Faculty of Electrical and Electronics Engineering, Ton Duc Thang University, 19 Nguyen Huu Tho street, Tan Phong Ward, District 7, Ho Chi Minh City, 70000, Vietnam

[†] Leading - Corresponding author: nguyenquangdung@tdtu.edu.vn
[*] Presenting author: nguyenquangdung@tdtu.edu.vn

Abstract

In high-performance controls of AC motors, speed measurement is an important factor in achieving precise control of the rotor speed. Generally, in the sensored control strategy, the rotor speed is obtained by tachometers, encoders or other position sensors. However, the system's durability and reliability suffers due to the installation of mechanical position sensors, which also increases the cost of the drive system. The removal of speed sensors, mounted on the motor shaft, provides low cost of the electric drive as a whole, higher security when operating in a hostile environment (high pressure, high temperature, humidity, etc.), compactness, easier maintenance of the electric drive system, as well as very high speeds. Furthermore, additional installation space is required in the AC motor drive system. In addition, estimating speed and other working parameters of a running induction motor plays an important role in the fault diagnostics. Therefore, sensorless control is a promising way to solve these problems. In this research, a modified Kalman observer is proposed for the speed estimation of induction motor. The paper also will carry out the application of proposed modified Kalman observer in comparison to a classical Adaptive Luenberger speed observer and their performances of sensorless control of induction motor.

Keywords: *Induction motor, Modified Kalman speed observer, Luenberger speed observer, Sensorless control*

[O-2-8] Direct Torque Controlled PMSM Drive with Space Vector PWM and Fuzzy Logic

Quang Thanh Nguyen[1, *], Trung Van Nguyen[2], Hau Huu Vo[3, †],

Chau Si Thien Dong[3], Duy Hoang Vo[3]

[1] Faculty of Electrical and Electronics Engineering, Ton Duc Thang University, 19 Nguyen Huu Tho Street, Tan Phong Ward, District 7, Ho Chi Minh City, 70000, Vietnam

[2] Department for Facility Management, Ton Duc Thang University, 19 Nguyen Huu Tho Street, Tan Phong Ward, District 7, Ho Chi Minh City, 70000, Vietnam

[3] Modeling Evolutionary Algorithms Simulation and Artificial Intelligence, Faculty of Electrical and Electronics Engineering, Ton Duc Thang University, 19 Nguyen Huu Tho Street, Tan Phong Ward, District 7, Ho Chi Minh City, 70000, Vietnam

[†] Leading - Corresponding author: vohuuhau@tdtu.edu.vn

[*] Presenting author: nguyenthanhquang@tdtu.edu.vn

Abstract

The paper deals with application of space vector pulse-width-modulation (SVPWM) scheme and fuzzy logic in permanent magnetic synchronous motor drive using direct torque control (DTC) structure. The first part is mathematical description for the control structure of PMSM drive in stationary reference frame. Hysteresis-band controllers and switching table in DTC structure are replaced by proportional integral (PI) controllers and SVPWM scheme. Parameters of speed controller are tuned by fuzzy logic theory. The performance of fuzzy speed controller is confirmed by simulation results with a wide range of motor speed and load torque.

Keywords: *Permanent magnetic synchronous motor (PMSM), Direct torque control (DTC), Pulse width modulation (PWM), Fuzzy logic*

[O-3-1] Analysis of Ductile-to-brittle Transition Temperature on DH36 High-strength Steel Using Charpy V-Notch Test and Nonlinear Finite Element Method

Haris Nubli[1, *], SangJin Kim[2], Jung Min Sohn[1, 3, †]

[1] Department of Marine Convergence Design Engineering, Pukyong National University, 45 Yongso-ro, Nam-gu, Busan, 48513, Republic of Korea

[2] Department of Marine Environment and Engineering, National Sun Yat-sen University, 70 Lienhai Road, Kaohsiung, 80424, Taiwan

[3] Department of Naval Architecture and Marine Systems Engineering, Pukyong National University, 45 Yongso-ro, Nam-gu, Busan, 48513, Republic of Korea

[†] Leading - Corresponding author: jminz@pknu.ac.kr

[*] Presenting author: harris@pukyong.ac.kr

Abstract

Carrying and handling LNG fuel has a higher safety level than conventional diesel fuel. LNG is stored inside special storage such as Type-C independent tank at the cryogenic temperature that can reach -163ºC. This cryogenic liquid could cause damage to the ship's structure if an accidental gas release happened. Steel brittleness could be increased after excessive exposure to LNG flow. Thus, steel with higher strength and cryogenic temperature resistance must be applied as a mitigation response against accidental LNG release on the LNG-fueled ship.

This study aims to analyze DTBTT (ductile-to-brittle transition temperature) on DH36 high-strength steel used as the ship's structural steel. The Charpy V-Notch test based on ASTM was conducted to obtain the toughness of DH36 steel, by acquiring the energy amount absorbed by a material during fracture. Twenty-one specimens were provided for the Charpy V-Notch test which 20.0ºC to -196.0ºC were applied. In addition, NLFEA (nonlinear finite element analysis) was performed as a numerical prediction for the Charpy V-Notch test. Mesh sensitivity analysis was also provided to ensure the consistency of NLFEA results. Furthermore, the procedure of the Charpy V-Notch test and NLFEA, as well as the DTBTT result of DH36 steel are presented and discussed.

Keywords: *Brittle fracture, Ductile-to-brittle transition temperature, Charpy V-Notch test, Cryogenic temperature, Nonlinear finite element analysis*

[O-3-2] Properties of Cement Paste Using Silica Functionalized MWCNT Dispersed by Polycarboxylate Ester

Aidyn Tugelbayev[1], Ji-Hyun Kim[2], Chul-Woo Chung[3, †, *]

[1] Division of Architectural and Fire Protection Engineering, Pukyong National University, Yongso-ro 45, Nam-gu, Busan, 48513, Republic of Korea

[2] Multidisciplinary Infra-Technology Research Laboratory, Pukyong National University, Yongso-ro 45, Nam-gu, Busan, 48513, Republic of Korea

[3] Division of Architectural and Fire Protection Engineering, Pukyong National University, Yongso-ro 45, Nam-gu, Busan, 48513, Republic of Korea

[†] Leading - Corresponding author: cwchung@pknu.ac.kr

[*] Presenting author: cwchung@pknu.ac.kr

Abstract

In this work, properties of cement paste using multi-walled carbon nanotube (MWCNT) solution dispersed by polycarboxylate ester (PCE) have been discussed. To provide better dispersion of MWCNT in water as well as to facilitate bond between cement paste and MWCNT, the process to achieve silica functionalization on MWCNT was applied using tetraethyl orthosilicate (TEOS). Properties of cement paste with pristine and silica functionalized MWCNT were analyzed using rheology, isothermal calorimetry, and mechanical strength. Silica functionalized MWCNT provided better bonding between MWCNT and cement hydration products to increase mechanical strength of cement paste. This work also provides in-depth discussion on optimal content of PCE required for dispersion of MWCNT with respect to the effect of redundant PCE on properties of cement paste.

Keywords: *Multi-walled carbon nanotube, Cement paste, Polycarboxylate ester, Silica functionalization, Mechanical strength*

[O-3-3] Multi-criteria Decision-making Model for Reverse Logistics in E-commerce

Van-Hau Nguyen[1, 2, *], Mai-Ha Phan[1, 2, †]

[1] Department of Industrial Systems Engineering, Faculty of Mechanical Engineering, Ho Chi Minh City University of Technology (HCMUT), 268 Ly Thuong Kiet Street, District 10, Ho Chi Minh City, Vietnam
[2] Vietnam National University Ho Chi Minh City, Linh Trung Ward, Ho Chi Minh City, Vietnam

[†] Leading - Corresponding author: ptmaiha@hcmut.edu.vn
[*] Presenting author: hau.nguyen0364290224@hcmut.edu.vn

Abstract

After the boom in online shopping during the Covid-19 pandemic, E-commerce has grown rapidly, causing many businesses to face an increase in the rate of product recalls because customers do not have direct access to goods as in traditional commerce. Therefore, the handling of returned products is considered an inevitable problem, which can lose all cost-saving opportunities, negatively affect the environment and reduce the level of customer service of e-commerce businesses. Besides, as competitive pressure continues to increase in E-commerce, E-commerce corporations have begun to implement more efficient, sustainable and reliable Reverse Logistics (RL) strategies by considering factors such as: cost, environment and society to solve that problem. RL in E-commerce refers to the sequence of activities necessary to collect and process returned products from customers, of which there are 3 important decisions for returned goods: Fix/Refurbish or Resell or Disposal of the product. In that context, the aim of this study is to develop a multi-criteria decision support model to assist businesses in evaluating and selecting the above decisions for returned products using Activity-Based Costing (ABC) method. Then, this paper proposes Analytic Hierarchy Process (AHP) model to evaluate and select the best decision based on criteria related to economic, environmental and social factors. This study will provide a fuller and more robust assessment process to help E-commerce businesses and any organizations involved in reverse logistics management in making decisions on how to handle Returned products more efficiently, reducing costs, positively impacting the environment, and increasing customer service.

Keywords: *Activity-based costing, Analytic hierarchy process, E-commerce, Reverse logistics, Sustainability*

[O-3-4] Aggregate Planning in Manufacturing Industry: ACase Study in Vietnam

Thanh-Thuy Truong Pham[1, 2, *], Mai-Ha Phan[1, 2, †]

[1] Department of Industrial Systems Engineering, Faculty of Mechanical Engineering, Ho Chi Minh City University of Technology (HCMUT), 268 Ly Thuong Kiet Street, District 10, Ho Chi Minh City, Vietnam
[2] Vietnam National University Ho Chi Minh City, Linh Trung Ward, Ho Chi Minh City, Vietnam

[†] Leading - Corresponding author: ptmaiha@hcmut.edu.vn
[*] Presenting author: phamtruongthanhthuy0@gmail.com

Abstract

The competition in the market is becoming more and more fierce, so it is very important to effectively use resources, and minimize costs but still meet customer demands to create a competitive advantage. Therefore, a strategic movement is needed. Aggregate planning aims at meeting demand over a specified time horizon in a way that maximizes profit through optimal levels of production, capacity, subcontracting, inventory, and stockouts. Although aggregate planning is very popular at international level, especially in large companies, most Vietnamese companies are unfamiliar with it. This study introduces complete aggregate planning for a leading plastic manufacturing company in Vietnam. The data are gathered from the company and are used to calculate the aggregate planning strategies, such as optimal strategy, level strategy, and mixed strategy using the POM QM application. Results obtained in those three strategies then are compared to find which strategy has the least cost of production. The outcome of this study is that the mixed strategy calculated using transportation model has the least cost of production. Having effective aggregate planning will help the company to utilize its potential to meet customer needs even when demands fluctuate widely while reducing production costs. Moreover, this study provides a standardized model for integrating aggregate planning that could be applied by other companies as well.

Keywords: *Aggregate planning, Transportation model, Cost of production*

[O-3-5] Effect of Pavement Structure-cover Soil System on Behavior of Buried Precast Box Culverts under Vehicle Live Loading

Nguyen Van Toan [*, †], Nguyen Vinh Sang

Thuyloi University Southern Campus, 02 Truong Sa street, Ward 17, Binh Thanh district, Ho Chi Minh City, 72321, Vietnam

[†] Leading - Corresponding author: toannv@tlu.edu.vn

[*] Presenting author: toannv@tlu.edu.vn

Abstract

Buried precast concrete box culverts are vital in connecting road networks of transportation systems. Live load from vehicle above culverts transmits to the culvert structures through pavement structures and cover the soil system. The study's objective is to investigate the influence of pavement structure-cover soil system on the behavior of buried precast concrete box culverts (spans smaller than 6 m) under vehicle live loading (truck loads). Firstly, this study presents an overview of the problems of buried precast concrete box culverts under the impact of passing vehicles. Secondly, a sophisticated 3D finite element model is simulated to verify and evaluate the propagation effect of vehicle load on the culvert structure. Results of the study indicate that as the vehicle moves through the culvert, the responses of the culvert structure change. Therefore, the behavior of the culvert also changes to adapt to the vehicle's load position on the culvert changes. Each time the vehicle passes, the behavior of the culvert structure has almost experienced a cycle of impact from the vehicle load. The pavement structure and soil cover play the vehicle impact dispersion and attenuation role. Therefore, the properties of the embankment structure, the thickness and stiffness, and the flexural resistance of these layers affect the behavior of the buried culvert structure.

Keywords: *Buried precast box culverts, Live loads, Pavement structure, Soil cover*

[O-3-6] Numerical Analysis of Local Scour of the Offshore Wind Turbines

Thi-Hong-Nhi Vuong[1, 4, *, †], Thi-Hong-Hieu Le[1, 4], Thanh-Long Le[2, 3, 4]

[1] Faculty of Transportation Engineering, Ho Chi Minh City University of Technology (HCMUT), 268 Ly Thuong Kiet Street, District 10, Ho Chi Minh City, Vietnam
[2] Faculty of Mechanical Engineering, Ho Chi Minh City University of Technology (HCMUT), 268 Ly Thuong Kiet Street, District 10, Ho Chi Minh City, Vietnam
[3] National Key Laboratory of Digital Control and System Engineering (DCSELab), HCMUT, 268 Ly Thuong Kiet Street, District 10, Ho Chi Minh City, Vietnam
[4] Vietnam National University Ho Chi Minh City, Linh Trung Ward, Thu Duc City, Ho Chi Minh City, Vietnam

[†] Leading - Corresponding author: hongnhi1017@gmail.com
[*] Presenting author: hongnhi1017@gmail.com

Abstract

Rapid expansions of the offshore wind industry have stimulated a renewed interest in the behavior of offshore wind turbines. Most offshore wind turbines are supported by mono-pile, tripod, and jack-up wind turbines. These foundations are sensitive to scour, reducing their ultimate capacity and altering their dynamic response. However, the existing approaches ignore the sea bed's rheological properties in the scour process. This study sheds light on the post-equilibrium sea bed scour mechanism around a wind turbine. The simulation results explain the influence of different hydrodynamic mechanisms on the local scours in a cohesive fluid, such as periodic waves, random waves, and constant currents. The conventional Bingham model is adopted as the fundamental model. However, due to the intrinsic characteristic, the Bingham model cannot illustrate the stratified material satisfactorily. Therefore, the Bingham model is extended by introducing the discontinuous rheology relationship between the plug and sheared zone. A newly non-Newtonian fluid model, Discontinuous Bi-viscous Model (DBM), is invented to reproduce closet mud material nature without many empirical coefficients and an empirical formula. This new rheology model is integrated and coupled into the Splash3D model, which resolves the Navier-Stokes equations with PLIC- VOF surface-tracking algorithm. The results indicate that the scour hole can be more stable by using DBM. The backfilling and deformation of the scour hole are exhibited around the wind turbines. The complex vortex systems around the wind turbine are described as well.

Keywords: *Offshore wind turbines, Local scour, Rheology, Bingham model, Non-Newtonian fluid model*

1. Introduction

Today, wind energy, especially offshore wind energy (OWE), has received much attention. This is also a significant renewable energy alternative to fossil fuels in the future. Wind power has grown rapidly since 2000, driven by R&D, supportive policies and falling costs [1]. In Vietnam, offshore wind energy is a relatively new industry with great potential and prospects in the context of combating the impact of global climate change. According to the World Bank Group, more than 8% of the area of Vietnam ranked as having very good wind power potential (high wind speed about 7-8 m/s at the high of 65 m) can generate more than 110 GW, especially in the southern region, where the depth is 30 – 60 m [2]. Vietnam now has nearly 4 GW of wind power [3]. According to the World Bank Group, Vietnam has the capability to develop as much as 10 GW of offshore wind by 2030 [2].

Offshore wind turbines are impacted by waves and currents that will exert force on them. The seabed surrounding the supporting structure will also be partially scrubbed. Offshore wind turbines must not only withstand the impact of ocean currents and typhoon waves but also resist the threats caused by the local scour of the seabed around the foundation piles. As for the wave field, this study will construct a random wave field under Jonswap wave analysis. Preparations for local scour of the foundation pile caused by the waves in the painting.

2. Methodology

The conventional Bingham model is adopted as the fundamental model. However, due to the intrinsic characteristic, the Bingham model cannot illustrate the stratified material satisfactorily. Therefore, the Bingham model is extended by introducing the discontinuous rheology relationship between the plug and sheared zone. A newly non-Newtonian fluid model, Discontinuous Bi-viscous Model (DBM), is invented to reproduce closet mud material nature without many empirical coefficients and an empirical formula. Figure 1 shows the sketch of Newtonian, Bingham, Bi-viscous, and Discontinuous Bi-viscous fluid. For Discontinuous Bi-viscous model, the rheological viscosity is defined as:

$$\mu_r(\dot{\gamma}) = \begin{cases} \mu_A \gg \dfrac{\tau_y}{\dot{\gamma}_y} & if\ \dot{\gamma} < \dot{\gamma}_y \\ \mu_B + \dfrac{\tau_y}{\dot{\gamma}} & if\ \dot{\gamma} \geq \dot{\gamma}_y \end{cases}$$

where μ_A is the viscosity of the un-yield region, μ_B is the viscosity of the yield zone, τ_y is the yield stress, and $\dot{\gamma}_y$ is the yield strain rate, $\dot{\gamma}_{ij} = \frac{\partial \dot{u}_i}{\partial x_j} + \frac{\partial \dot{u}_j}{\partial x_i}$. The symbol $\dot{\gamma}$ is the second invariant of the $\dot{\gamma}_{ij}$, which is defined as $\dot{\gamma} = \sqrt{\frac{1}{2}\dot{\gamma}_{ij}\dot{\gamma}_{ij}}$.

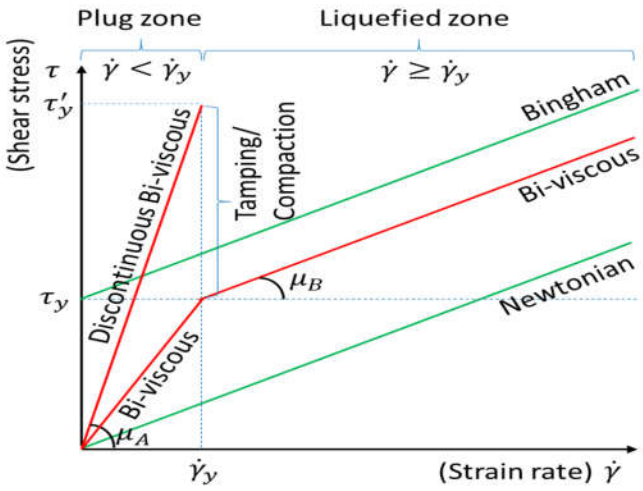

Figure 1. Sketch of Newtonian, Bingham, Bi-viscous, and Discontinuous Bi-viscous fluid

The viscoplastic models, DBM, were coupled with the Splash3D model. The Splash3D model was renovated from the open-source software, Truchas, which was originally developed by Los Alamos National Laboratory. The original program can simulate the incompressible flows with multi-fluid interfaces. The code solves three-dimensional continuity and Navier-Stokes equations by adopting the projection method and the finite volume discretization method. The Splash3D model was enhanced with several hydrodynamic modules such as the large eddy simulation (LES) turbulence module, and the moving-solid module to deal with breaking waves and wave-obstacle interaction problems.

3. Results and Discussion

Figure 2 shows the maximum value of negative and positive velocity near the bottom when the waves pass the tripod wind turbine in the case without current. One interesting thing is that the maximum absolute value of negative velocity is 2.0 m/s, while the maximum absolute value of positive velocity is 1.0 m/s. That causes the local scour downstream of both vertical and horizontal piles, which can be seen in Figure 3.

In the case of waves, the horseshoe vortex and the lee-wake vortex govern the scouring. These two processes are primarily described by the Keulegan-Carpenter number, KC, which is defined:

$$KC = \frac{u_m T_p}{D}$$

where u_m is velocity near the bottom, T_p is the peak wave period and D is the cylinder diameter.

When $KC < 6$, no scour hole formed. The physical explanation for this is that no horseshoe vortex develops for $KC < 6$. The scour hole develops when $KC \geq 6$. The empirical expression for the equilibrium scour depth S due to waves may be used:

$$\frac{S}{D} = 1.3\{1 - \exp[-0.03(KC - 6)]\}$$

In case 1, the maximum absolute velocity near the bottom $u_m = 2.0\ m/s$, the peak wave period $T_p = 8.0\ s$, and the cylinder diameter $D = 3.0\ m$. So, $KC = 5.3$. In theory, no scour hole is formed in this case. In the simulation results, we only witness the development of local scour around the horizontal pile the downstream.

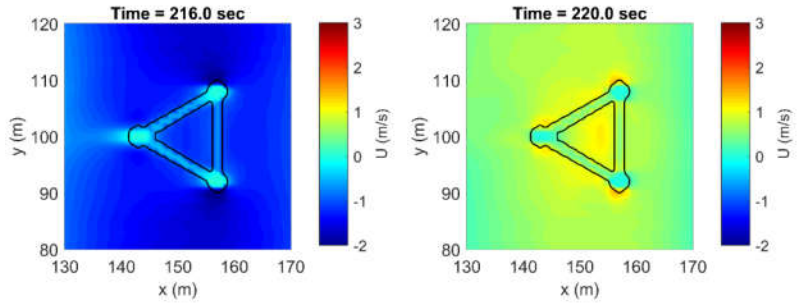

Figure 2. The minimum and the maximum velocity near the bottom in the case of random wave affecting tripod wind turbine

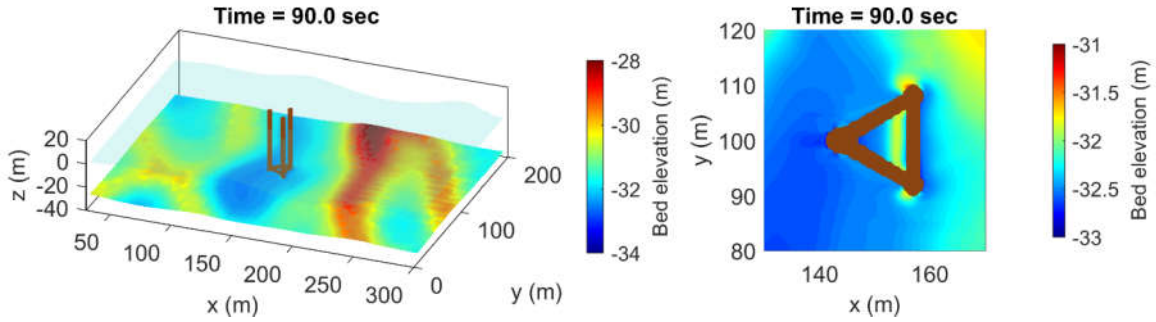

Figure 3. The 3D and the top view of the case random wave affecting tripod wind turbine

4. Conclusion

Local scour under the effect of the current, wave, and wave-current coupling is discussed in this study. Both regular and irregular waves are generated and propagated to the domain using the internal source model. The irregular waves are formed by JONSWAP spectral formulation. Three configurations of wind turbines are revealed in this study. The results show that the local scour is created around the wind turbine under the effect of both regular waves and irregular waves. In addition, the random wave and current coupling case witnesses a bigger and wider scour hole than the case of the irregular waves.

References

[1] International Renewable Energy Agency. https://www.irena.org/Energy-Transition/Technology/Wind-energy

[2] Offshore Wind Roadmap for Vietnam, World Bank, 2021.

[3] Southeast Asia: 10 Things to Watch in 2022, BloombergNEF; GWEC Market Intelligence.

[O-3-7] Numerical Study of Modeling and Hydrodynamic Characteristics of the Automated Hand-washing System

Thanh-Long Le[1, 2, 5, †], Nguyen Tan Tien[2, 5], Thi-Hong-Nhi Vuong[4, 5], Tran Thien Hau[3, 5], Tran Quang Lam[4, 5], Trung Tin Kieu[1, 5], Mach Ngoc Han[1, 5], Phung Tran Hanh[1, 5, *]

[1] Faculty of Mechanical Engineering, Ho Chi Minh City University of Technology (HCMUT), 268 Ly Thuong Kiet Street, District 10, Ho Chi Minh City, Vietnam
[2] National Key Laboratory of Digital Control and System Engineering (DCSELab), HCMUT, 268 Ly Thuong Kiet Street, District 10, Ho Chi Minh City, Vietnam
[3] Faculty of Applied Science, Ho Chi Minh City University of Technology (HCMUT), 268 Ly Thuong Kiet Street, District 10, Ho Chi Minh City, Vietnam
[4] Faculty of Transportation Engineering, Ho Chi Minh City University of Technology (HCMUT), 268 Ly Thuong Kiet Street, District 10, Ho Chi Minh City, Vietnam
[5] Vietnam National University Ho Chi Minh City, Linh Trung Ward, Thu Duc City, Ho Chi Minh City, Vietnam

[†] Leading - Corresponding author: ltlong@hcmut.edu.vn
[*] Presenting author: hanh.phungcokhi.19_3@hcmut.edu.vn

Abstract

In this study, numerical computation is used to develop a physical model of the hand-washing chamber and investigate this device's bactericidal effect. It needs to design a hand-washing chamber system to serve people working in areas affected by COVID-19, also ensure safety, and limit the spread of this pandemic. This paper gives an illustration of using the computational fluid dynamics approach to investigate the movement of the solution inside the hand-washing chamber. The numerical results obtained from the numerical simulation demonstrate the hydrodynamic values, streamlines, and density of the solution. The ability to predict the hand-washing chamber's hydraulic and cleaning performance efficiencies is essential for evaluating the operability and improving the further design.

Keywords: *Numerical computation, Computational fluid dynamics, Hydrodynamic values, Hand washing chamber*

1. Introduction

In 2019, the SARS-CoV-2 appeared to spread around the world at a rapid pace. It caused overwhelming health systems, damaging economies, spreading fear and claiming lives [1]. At the time, it seemed that the entire science of the world focused on finding and improving devices to fight the spread of COVID-19 and a cure to treat them. One of the common methods is to use an automatic hand-washing machine. The World Heathy Organization (WHO) recommends performing handwashing rather than hand rubbing with an alcohol-based-solution after contact with a patient with Clostridium difficile infections (CDIs), especially in the context of outbreaks [2]. According to the research paper of Joan G.Turner. and the fortifications used of image analysis to measure handwashing effectiveness. The result illustrated manual hand-washing removed 72,5% of the particles, whereas the automated hand-washing just removed 23,5% [3]. In the study by Jolan Baccay Sy and his friends, they stated that multi-station automatic hand wash provides complete and hygienic hand washing activities with soap and water [4]. So the combination of both automatic hand-washing and the WHO hand-washing technique, which is suitable [2, 4].

CFD is also useful technology for the knowledge of hydro-aerodynamics in many areas such as evaluating fluid motion and hydrodynamic characteristics (pressure, velocity, etc.) in a microchannel, sterilization chamber unit in operating rooms [5-7]. In the present, CFD is very rare to use CFD approach to analyze the hydrodynamic characteristics of the flow in hand washing machines. Therefore, it is very interesting that we used the CFD analysis to improve the cleaning performance of hand washing machines.

This paper aims to improve hydrodynamic performance of automated hand-washing system. In the paper, the value velocity of the inlet and value pressure of the outlet are proposed to represent the configuration of the automatic hand-washing system; the presented values are optimized to improve its cleaning performance. The CFD analysis is went on assesst the configuration's performance at certain sample points of design space.

2. Physical model and Numerical method

2.1. Physical model

In this study, we built construction of the hand-washing chamber with the important feature of this chamber in real life. The model ensures to be used suitably for Vietnamese people with an average arm length of 0.6 meters or more. The chamber has a diameter of 0.2 m and a height of 0.32 m. The hand-washing machine has entry and exit points, chemical tank and sprinkler system. In the following design of the chamber, the liquid flow is estimated that sprayed full of the chamber after 12 seconds.

The CleanTech Automated Hand-Washing System (CTAHS) ensures complete control of hand hygiene. The system has a compact design with a turnstile that automatically opens at the end of each 12-second wash and rinse cycle, and uses 75% less soap and water than manual washes. It also removes 99.98% of dangerous pathogens from bare skin and gloved hands. The CleanTech Automated Hand-Washing System is designed for high-use areas and can wash hands of up to 4 - 5 users per minute. Ideal for environments such as food processing, cleanroom, and pharmaceutical manufacturing where effective hand hygiene is critical. This study used a combination of Computational Fluid Dynamics (CFD) and Fluent module of Ansys Workbench to give predictions about the behavior and movement of disinfection solution in this hand-washing rotating chamber. The main purpose of this paper was to examine the dispersion within the hand-washing cage. It means some solid parts of this chamber are reduced (Figure 1).

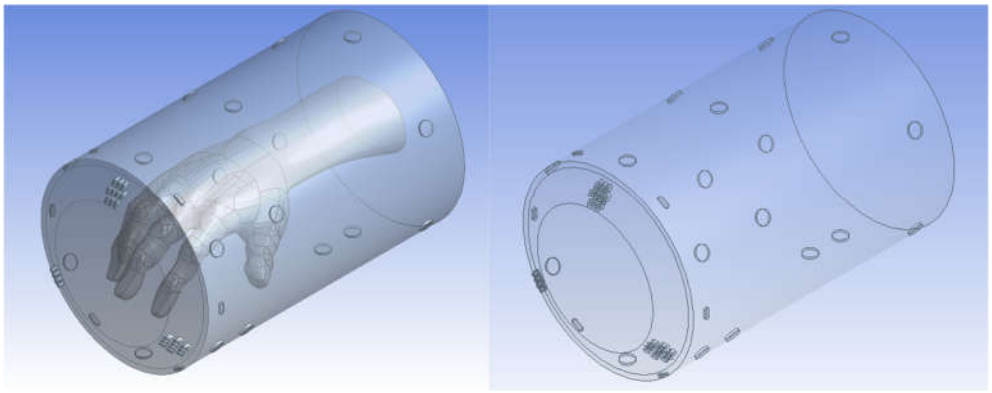

Figure 1. A model of the hand washing chamber

With the design of the rotating washroom, the solution is sprayed through nozzles installed in the room. For the purpose of obtaining simulation results in this study, the Navier-Stokes equations and some related equations are used to analyze the flow of fluids in 3-D dimensions.

Navier-Stokes equation:

$$\rho\left(\frac{\partial \mathbf{u}}{\partial \mathrm{t}} + \mathbf{u}.\nabla\mathbf{u}\right) = -\nabla \mathrm{p} + \nabla.\mathbb{T} + \mathbf{F} \quad (1)$$

The conservation of mass:

$$\frac{\partial \rho}{\partial t} + \nabla.(\rho.\mathbf{u}) = 0 \quad (2)$$

where:

ρ is the density (SI unit: kg/m^3)

$\mathbf{u}$ is the velocity vector (SI unit: m/s)

p is the pressure (SI unit: Pa)

$\mathbf{F}$ is the volume force vector (SI unit: N/m^3)

Turbulence always seems to be a problem when simulating with CFD. In this study, the sterilization chamber was analyzed using the achievable k-ε module. According to T.-H Shin et al., this module is known for computing turbulent flow by evaluating the kinetic energy equation (k) and the turbulent dissipation equation (ε). The achievable k-ε modulus is widely used in turbulence models in research or industrial applications due to better results and reduced number of computations in turbulent flow [8].

The kinetic energy equation (k):

$$\frac{\partial}{\partial t}(\rho k) + \frac{\partial}{\partial x_j}(\rho k u_j) = \frac{\partial}{\partial x_j}\left[\left(\mu + \frac{\mu_t}{\sigma_k}\right)\frac{\partial k}{\partial x_j}\right] + P_k + P_b - \rho\epsilon - Y_M + S_k \quad (3)$$

The turbulent dissipation equation (ε):

$$\frac{\partial}{\partial t}(\rho\epsilon) + \frac{\partial}{\partial x_j}(\rho\epsilon u_j) = \frac{\partial}{\partial x_j}\left[\left(\mu + \frac{\mu_t}{\sigma_\epsilon}\right)\frac{\partial \epsilon}{\partial x_j}\right] + \rho C_1 S_\epsilon - \rho C_2 \frac{\epsilon^2}{k+\sqrt{\nu\epsilon}} + C_{1\epsilon}\frac{\epsilon}{k}C_{3\epsilon}P_b + S_\epsilon \quad (4)$$

where:

$$C_1 = max\left[0.43, \frac{\eta}{\eta+5}\right]$$

$$\eta = S\frac{k}{\epsilon}$$

$$S = \sqrt{2S_{ij}S_{ij}}$$

$C_\mu = 0.09, \sigma_k = 1$

$$\sigma_\epsilon = 1.3, \qquad C_{1\epsilon} = 1.44$$

u_j is velocity component in corresponding direction

μ_t is eddy viscosity, $\mu_t = \rho C_\mu \frac{k^2}{\epsilon}$

2.2. Numerical method

Numerical method are used to simulate of motion and hydrodynamic properties of objects in a fluid environment. To analyze various fluid flows, we can use continuity equations, momentum equations, and energy equations. So CFD was applied to speed up the calculation process. In this study, the use of CFD to predict the cleaning performance and motion of liquid flow is suitable.

After having the physical model, the meshing is generated. In the case hand inside the chamber, there are 449018 nodes and 2392611 elements in total. All of the surface, including the human hand is set as walls; the inlets are located in the sprinkler which speeds at 2m/s.

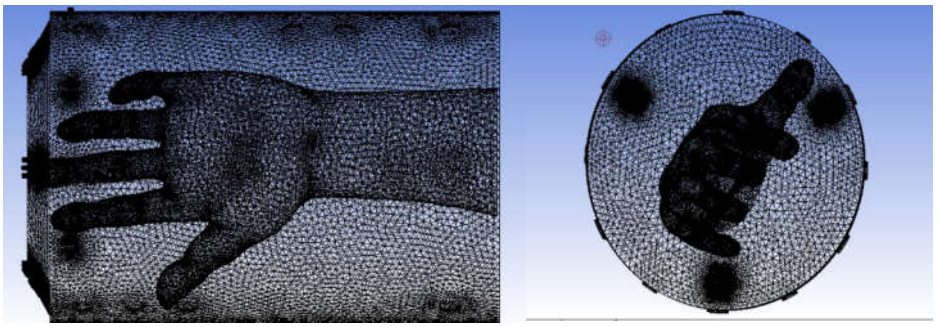

Figure 2. Typical mesh used in the computational domain for the hand-washing rotating chamber

3. Results and Discussion

Figure 3 illustrates the distribution of fluid flow through the entire rotating chamber during operation. The results obtained from the simulations show that the flow is evenly spread throughout the chamber and the human hand. The areas of the hands are filled with a dense stream of solution, which is good because these parts can easily become infected with viruses. Figures 4 and 5 give illustrations of the fluid flow and its velocity during operation. The maximum speed (2m/s) occurs at the nozzle and the minimum speed occurs in the middle of the chamber (hand position). This is entirely appropriate as there should be a hand washing vortex in the middle of the chamber to remove the virus on the hands.

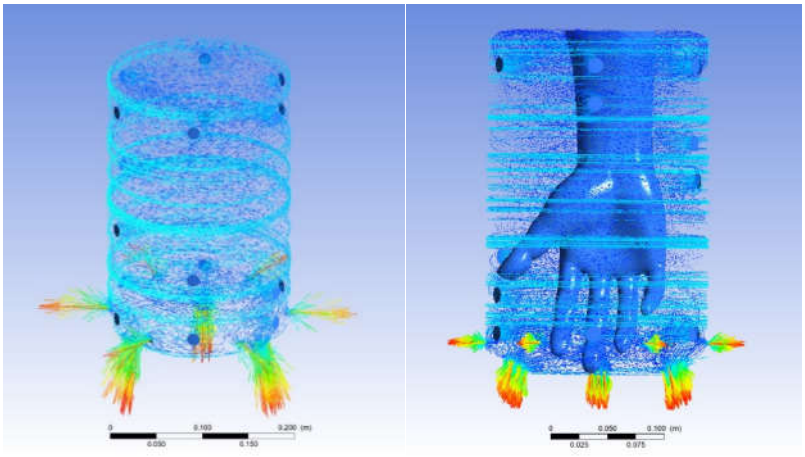

a) b)

Figure 3. The flow distributions of the chamber (a) Without human; (b) With human

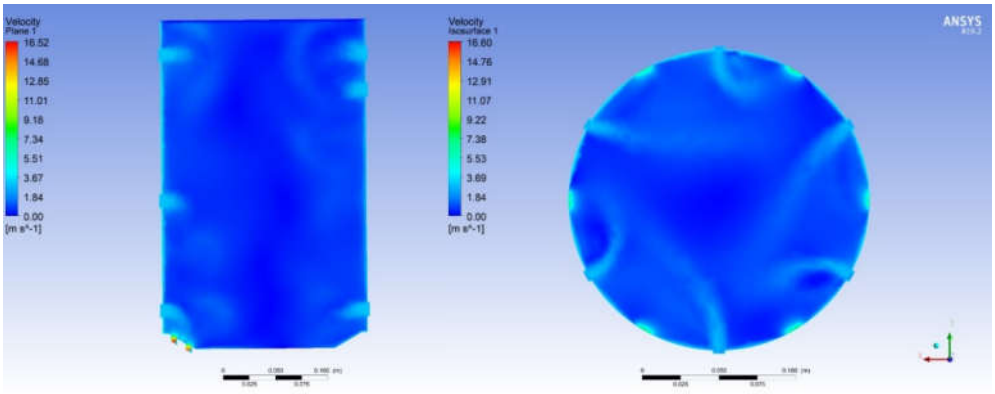

Figure 4. The velocity field of the chamber

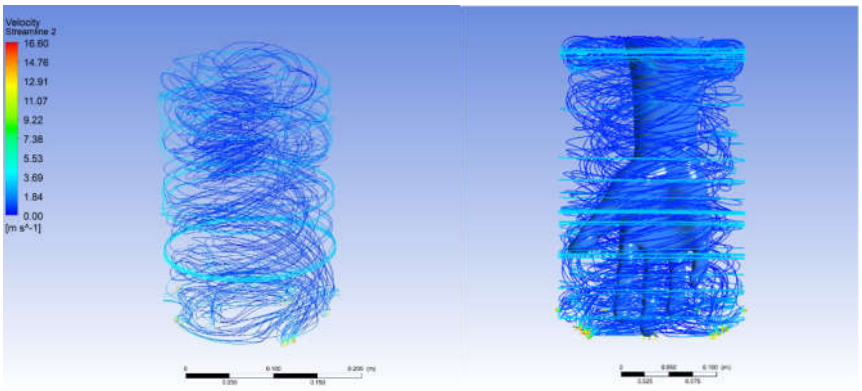

(a) (b)

Figure 5. The streamlines of the chamber (a) Without hand; (b)With hand

4. Conlusion

In this study, the design of the hand washing chamber was modeled, meshed and analyzed to obtain characteristics such as water volume distribution, liquid flow. The results show that this chamber is suitable for practical applications. It also offers the ability to upgrade and optimize new designs in the future.

Acknowledgment

This research is supported by DCSELAB and funded by Vietnam National University Ho Chi Minh City (VNU-HCM) under grant number TX2023-20b-01. We acknowledge the support of time and facilities from Ho Chi Minh City University of Technology (HCMUT), VNU-HCM for this study.

References

[1] A. Wickramatillake, C. Kurukularatne, SARS-CoV-2 human disinfection chamber: a critical analysis, Occupational Medicine 70 (2020) 330-334.

[2] P. Deschênes, F. Chano, L. Dionne, D. Pittet, Y. Longtin, Efficacy of the World Health Organization–recommended handwashing technique and a modified washing technique to remove Clostridium difficile from hands, American Journal of Infection Control 45 (2017) 844-848.

[3] J. G. Turner, D. K. Gauthier, J. R. Roby, E. Larson, J. J. Gauthier, Use of image analysis to measure handwashing effectiveness, American Journal of Infection Control 22 (1994) 218-223.

[4] J. Baccay Sy, M. G. Rojo, E. R. Calibara, A. V. Comendador, W. Degife, A. S. Yimer, Multi-Station Automated Hand Washing System, International Journal of Recent Technology and Engineering 9 (2020) 36-43.

[5] T. L. Le, T. D. Hong, Computational fluid dynamics study of the hydrodynamic characteristics of a torpedo-shaped underwater glider, Fluids 6 (2021) 252.

[6] T.-L. Le, J.-C. Chen, and H.-B. Nguyen, Numerical study of the thermocapillary droplet migration in a microchannel under a blocking effect from the heated wall, Appl. Thermal Eng. 122 (2017) 820-830.

[7] T.-L. Le, J.-C. Chen, and H.-B. Nguyen, Numerical investigation of the forward and backward thermocapillary motion of a water droplet in a microchannel by two periodically activated heat sources, Numerical Heat Transfer, Part A: Applications 79 (2021) 146-162.

[8] T-H. Shih, W.W. Liou, A. Shabbir, Z. Yang, J. Zhu, A new k-ε eddy viscosity model for high Reynolds number turbulent flows 24 (1995) 227-238.

[O-3-8] Design of the Smart Cranial Molding Helmet for Infant SCMH2023

Minh Khoi Phan[1], Nguyen Duy Phuong Tran[1, †], Quang Minh Nguyen[1], Bao Vy Phan[1, *], Duc Thien Tran[2], Thanh Liem Dao[3], Fakhri Yagob[4], Thien My Dao[4], Chu Tan Phan[1]

[1] Faculty of Mechanical Engineering, HCMC University of Technology, Ho Chi Minh City, 700000, Vietnam

[2] Faculty of Electrical and Electronics Engineering, HCMC University of Technology and Education, Thu Duc City – Ho Chi Minh City, 700000, Vietnam

[3] Faculty of Engineering and Technology, Nguyen Tat Thanh University, Ho Chi Minh City, 700000, Vietnam

[4] Département de génie mécanique, École de technologie supérieure, 1100 Notre-Dame St W, Montreal, H3C 1K3, Canada

[†] Leading - Corresponding author: tnduyphuong@yahoo.com

[*] Presenting author: pbv153@gmail.com

Abstract

This paper introduces the plagiocephaly condition in infants and the treatment method with smart cranial orthopedic helmets. Applying photogrammetry to 3D scanning of infants' heads to design orthopedic helmets. It is designed specifically for each infant so it will help them feel comfortable. The orthopedic helmet has ultrasonic distance sensors to monitor head growth. Moreover, it has a sensor to monitor temperature and humidity when infants are wearing this helmet. Using CAE in the optimization of the orthopedic helmet helps to reduce the weight and cost. The helmet made by 3D printing technology with PLA material is very popular and is not harmful to health.

Keywords: *Photogrammetry, Smart helmet, Plagiocephaly, CAE, 3D printing*

Poster Presentation

[P-1-1] Comparison of Transport Property Predictions of Supercritical Hydrocarbon Aviation Fuels

Sung-rok Hwang and Hyung Ju Lee[†, *]

Department of Mechanical Engineering, 45 Yongso-ro, Nam-gu, Busan, 48513, Republic of Korea

[†] Leading - Corresponding author: hj.lee@pknu.ac.kr

[*] Presenting author: hj.lee@pknu.ac.kr

Abstract

Hydrocarbon aviation fuels are known to have excellent cooling capacities through heat-absorbing chemical reactions such as thermal cracking or pyrolysis, and thus regenerative heat sink cooling systems have been studied worldwide using hydrocarbon fuels as a coolant in order to deal with aero-thermodynamic heating and to realize efficient supersonic combustion in a scramjet-powered hypersonic cruise vehicle. When the hydrocarbon fuel is heated and pressurized to above its critical point and pyrolyzed into multiple components in a regenerative cooling system, its thermophysical properties change drastically, which subsequently influences the overall flow and heat transfer characteristics inside the cooling channels. In order to assess precisely the performance characteristics of a regenerative cooling system and a scramjet combustor, it is substantial to obtain the thermodynamic and transport properties of hydrocarbon aviation fuels and the mixtures of their decomposed products accurately over a wide range of temperature and pressure conditions. In the current study, therefore, predictions of transport properties including viscosity and thermal conductivity of typical hydrocarbon aviation fuels and their decomposed products have been carried out by using a couple of transport property prediction methodologies, and their prediction performance has been compared with the NIST database in terms of relative deviation as well as with each other. The viscosity and thermal conductivity of representative fuels and some of their products are predicted in the range of temperatures from 300 to 1,000 K and pressures from 0.1 to 5.0 MPa, and it has been shown that the extensive transport property data can be obtained by using those methods over a wide range of temperature and pressure conditions. In addition, it has been found that Chung et al.'s method and Brule and Starling method are the most accurate in predicting viscosity while the modified Propane-based TRAPP method is the best for thermal conductivity. It is, therefore, expected that they would be applied effectively in a variety of design, modeling, and simulation studies for developing highly efficient regenerative cooling systems and scramjet combustors of a hypersonic flight vehicle.

Keywords: *Hypersonic vehicle, Regenerative cooling system, Thermal cracking, Viscosity, Thermal conductivity*

[P-1-2] Smart Nanotransfer Printing Process with High Resolution at Eight-inch Wafer Scale

Tae Wan Park, Hee Lack Choi, Woon Ik Park[*, †]

Department of Materials Science and Engineering, Pukyong National University (PKNU), 45 Yongso-ro, Busan 48513 Republic of Korea

[†] Leading - Corresponding author: thane0428@pknu.ac.kr
[*] Presenting author: thane0428@pknu.ac.kr

Abstract

Nanotransfer printing (nTP) is one of the promising nanopatterning methods due to its simple process, effective processing cost, and excellent scalability for various nanostructures. Here, we show a facile and useful thermally assisted nanotransfer printing (T-nTP) process that can effectively generate highly ordered ultra-fine nanostructures at 8-inch wafer scale by the use of a heat-rolling-press system that can provide uniform heat and pressure. We show reliable pattern generation of a variety of functional materials, such as Pt, Pd, Ag, NiO, WO_3, and $Ge_xSb_yTe_z$. Furthermore, we show the formation of ultrafine three-dimensional (3D) complex nanostructures via the combined process of T-nTP and directed self-assembly (DSA) of block copolymers (BCPs). Moreover, we show how to obtain a high-density NiO_x/Pt memristive crossbar structure, showing excellent unipolar resistive switching behavior. We expect that this novel and smart T-nTP method will be applicable to wafer-scale nanofabrication combined with many other patterning techniques.

Keywords: *Nanotransfer printing, Nanostructures, Wafer scale, Resistive memory*

[P-1-3] Development of Diesel Particulate Filter on 100kw Diesel Engine for Coastal Ship

Min-A Je[1, *], Sang-Won Kim[1], Sung-Chul Hwang[2], Sukho Jung[3, †]

[1] Pukyong national university, 45 Yongso-ro Nam-gu, Busan, 48513, Korea
[2] Get-SCR, 854-3 Muan-ro Bubuk-myoen, Miryang, 50404, Korea
[3] Pukyong national university, 45 Yongso-ro Nam-gu, Busan, 48513, Korea

[†] Leading - Corresponding author: sukhojung@pknu.ac.kr
[*] Presenting author: jm4513@naver.com

Abstract

Particulate matter which is contained in a large amount in the exhaust gas of diesel engines is the main cause of fine dust pollution, and regulations on emissions on land have already been implemented. However, regulations on emissions from ships have not yet been enforced, but will soon be enforced in a coastal area. Therefore, it is necessary to develop Particulate matter reduction technology that can be applied to small coastal vessels. In this research, a conceptual design was performed for the development of diesel particulate filter, a Particulate matter reduction system for a 100kW diesel engine. Flow analysis through a commercial software was performed by changing the length of the reducer around the catalyst in 5 steps (Case 1 to Case 5) in the shape of the diesel particulate filter. It was found that Case 3 was most suitable based on the distribution of flow velocity and pressure in the diesel particulate filter by adjusting the particle size so that it could pass through the porous region, which is the reduction part, and using the particle tracking technique. The diesel particulate filter was fabricated through detailed design and tested in a 100kW diesel engine. As a result, it was confirmed that Particulate matter emissions were reduced by more than 90%.

Keywords: *Particulate matters, Diesel particulate filter, Computational fluid dynamics, Diesel engine, Coastal ship*

This work was supported by the Technology development Program(S3282183) funded by the Ministry of SMEs and Startups (MSS, Korea)

[P-1-4] Hydrophobically Crosslinked PDMS-coated PVDF Composite Membrane for the Pervaporation of Isopropanol /1.5 Pentanediol Feed Solution

Shivshankar Chaudhari, Youngeup Jin, Seokhwan.Seo, Minyoung Shon[†, *]

Department of Industrial Chemistry, Pukyong National University, 45, Yongso-ro, Nam-Gu, Busan 48513, Korea

[†] Leading - Corresponding author: myshon@pknu.ac.kr

[*] Presenting author: myshon@pknu.ac.kr

Abstract

Energy efficient pervaporation facile approach was intended for the removal of isopropanol from 1, 5, and 1, 2pentanediol diols production process. In order to do that, a series of Polydimethylsiloxane (PDMS) membranes were prepared by tuning their surface chemistry through the trifunctional (PFTES and OTMS) and traditional tetra functional (TEOS) crosslinkers and casting on the polyvinylidene fluoride (PVDF) membrane. Additional hydrophobic tail enrichment on the membrane surface due to alkyl (OTMS) and fluoroalkyl groups (PDFTES) from trifunctional crosslinker was confirmed from the FTIR, XPS, and DSC studies. TGA and XRD studies revealed that tetra crosslinking sites promote dense structure across the membrane compared to the trifunctional crosslinker. In water contact angle measurement of different series of the membrane, the contact angle was proportional to the hydrophobic site was observed. The PDMS- PVDF composite membrane morphology was observed from the FESEM study. All the membranes exhibited excellent compatibility of both polymers with a PDMS layer thickness that was ca. 10 μm accounted. When the PDMS series of membranes were tested for pervaporation of novel feed PDO/IPA (90/10 w/w) system, the highest flux delivered from the fluoroalkyl type crosslinked membrane attributed to the superior hydrophobicity and amorphous nature of membrane with excellent IPA selectivity from all the membranes was observed. As the best result, the PDMS crosslinked by PFTES membrane resulted in the stabilized flux of 0.30 LMH and excellent separation factor (IPA content in permeated >99.95%) in 40 h continuous pervaporation test observed.

Keywords: *Pervaporation, 1,5 Pentane diol (PDO), Polydimethylsiloxane (PDMS), Polyvinylidene fluoride (PVDF), Fluoroalkyl groups*

[P-1-5] Alloy Development and Property Evaluation on High-temperature Structural Materials for Advanced Nuclear/Fusion Reactor Components

Sanghoon Noh[1, †, *], Sung-Dae Kim[1], Yong-Sik Ahn[1], Bu-An Kim[1], Jihwa Roh[2]

[1] Department of Materials Science and Engineering, Pukyong National University, 45 Yongso-ro, Nam-gu, Busan, 48513, Korea

[2] Division of Architecture and Design, Pukyong National University, Address, 45 Yongso-ro, Nam-gu, Busan, 48513, Korea

[†] Leading - Corresponding author: nohssang@pknu.ac.kr

[*] Presenting author: nohssang@pknu.ac.kr

Abstract

Korea has put in a huge effort to develop advanced nuclear/fusion systems such as a sodium-cooled fast reactor, molten salt reactor, and fusion reactor. As the realization of such nuclear/fusion systems relies heavily on the performance of structural materials, the high-temperature materials laboratory (HTML) in Pukyong National University has made persistent efforts to develop advanced structural materials that can withstand extremely harsh operating conditions. New alloy development and property evaluation have been carried out in Ni-based superalloy, refractory metals, and ferritic/martensitic steels. Intensive work has been performed to evaluate the feasibility of developing Ni-based oxide dispersion strengthened (ODS) alloys for MSR applications. Finely dispersed nano-oxide particles with a high number density in homogeneous grains can be very attractive to achieve superior mechanical properties at elevated temperatures. Microstructural observation indicated that the refinement and homogeneity of grain structures were considerably increased and these led excellent mechanical properties at elevated temperatures. Reduced activation ferritic/martensitic (RAFM) steel is a structural material for blankets and diverters in the fusion reactor. Since 2011, korean-typed RAFM steel has been successfully developed for Korean HCCR ITER-TBM components. To evaluate irradiation resistance of RAFM steels, heavy ion beam irradiation test is essential, which can simulate in high dose rate of neutron irradiation and nuclear fusion complex environment in a short period of time. In this presentation, R&D results and activities in HTML are introduced on high-temperature structural materials in domestic and international collaborative research works.

Keywords: *Microstructure, Mechanical property, Nuclear/fusion reactor, Structural materials*

[P-1-6] Non-lead Radiation Shielding Materials Using Metal Salts and Polymer Composites

Junghwan Kim[*, †], Sung-Gyoo Kim, Won-Chan Seo, Han-Sang Kwon, Young-soo Lim

Department of Materials System Engineering, Pukyong National University, 45, Yongso-ro, Nam-Gu, Busan, 48513, Republic of Korea

[†] Leading - Corresponding author: junghwan.kim@pknu.ac.kr
[*] Presenting author: junghwan.kim@pknu.ac.kr

Abstract

Lead (Pb) is the most widely used shielding material against X-rays, but it is very heavy and toxic to be used. Here, we aim to develop non-lead shielding materials against X-rays by using polydimethylsiloxane (PDMS) and metal salt composites. We found that the uniform dispersion of the metal salts in PDMS was inhibited due to the miscibility problem. By preforming the porous PDMS matrix, we successfully incorporated the metal salts into the PDMS matrix. The X-ray shielding ratios of the PDMS-metal composites were investigated by modulating the thickness and adsorption amount.

Keywords: *X-ray, Radiation, Shielding, Metal compounds, PDMS*

[P-1-7] Vibration-isolator Design for Electric Power Generator System under Consideration of Multi-excitation Events

Inpil Kang, Chan-Jung Kim[*, †]

School of Mechanical Engineering, Pukyong National University, 45 Yongseo-ro, Nam-gu, Busan, 48513, South Korea

[†] Leading - Corresponding author: cjkim@pknu.ac.kr
[*] Presenting author: cjkim@pknu.ac.kr

Abstract

The electric power generator has considerable excitations from the internal combustion engine, so the use of vibration-isolators is mandatory to prevent vibration transmissibility to the surrounding building. The proper selection of the mechanical properties of the vibration-isolator is important to promise quiet situation under operation. To evaluate the dynamic variations for different vibration-isolator cases, the theoretical linear power generator model is built by assuming the vibration-isolator as the linear mechanical element with both a spring and a damping coefficient. The first performance index is introduced to evaluate the vibration control capability over the self-excitation and the second performance index is used for the transmissibility from the basement to the electric power generator. Mechanical properties of the vibration-isolator beneath the mass block were selected to find the best condition over the four combinations of mechanical coefficients. The best case of vibration-isolator can be derived to decrease the second performance index even though the first performance index is increased up to the allowable limit so that the compromised vibration-isolator can be robust to multi-excitation events.

Keywords: *Vibration-isolator, Multi-excitation events, Electric power generation system, Viscous damping coefficient, Stiffness coefficient*

[P-1-8] A Study on the Recovery of Copper from Leachate of Solar Cells and PV Ribbon

Jei-Pil Wang[1, †, *], Jung-Hoon Lee[2], Seong-Mook Cho[2], Jae-Wung Bae[2],

Min-Seong Ko[2], Ki-Woo Nam[3]

[1] Divison of Convergence Materials Engineering, Major of Metallurgical Engineering, Department of Marine Convergence Design Engineering(Advanced Materials Engineering), Pukyong National University, Busan 48547, Republic of Korea
[2] Division of Convergence Materials Engineering, Major of Metallurgical Engineering, Pukyong National University, Busan 48547, Republic of Korea
[3] Division of Convergence Materials Engineering, Major of Materials Engineering, Pukyong National University, Busan 48547, Republic of Korea

[†] Leading - Corresponding author: jpwang@pknu.ac.kr
[*] Presenting author: jpwang@pknu.ac.kr

Abstract

As the eco-friendly energy demanded and greenhouse gas problems have recently emerged, the solar power market is growing rapidly around the world. Accordingly, a large amount of solar waste is also generated due to an increase in the installation amount of solar modules, and problems such as an increase in landfill costs and acceleration of global warming cannot be ignored. Therefore, by collecting alternative materials necessary for manufacturing solar modules, this study recovered valuable metal copper from solar cells and PV ribbons of solar waste modules to contribute to economic and environmental problems by reducing landfill costs and greenhouse gases generated when raw materials are collected etc. First, before recovering copper, the solar cell and PV ribbon attached to the surface of the solar cell were leached using a 3M nitric acid solution, and the leachate was recovered through vacuum filtration. Thereafter, 35wt% of hydrochloric acid was added to remove the silver component of the leachate to separate precipitation, and the leachate was also recovered through vacuum filtration. Copper, aluminum and trace impurities were present in the leachate from which the solar cell and silver component were removed. Based on the ionization tendency of metals(K>Ca>Na>Mg>Al>Zn>Fe>Ni>Sn>Pb>H>Cu>Hg>Ag>Pt>Au), copper was selectively recovered from leachate by using a substitution reaction using iron powder having higher oxidation properties than copper. At this time, as a result of the experiment by varying the input amount of iron powder to the leachate at 0.5g, 1g and 2g, copper powder with a purity of 99% or more could be recovered when 1g of iron powder was added.

Keywords: *Solar cell, PV ribbon, Substitution reaction, Copper, Purity*

Acknowledgement: This subject is supported by Korea Ministry of Environment(MOE) as “Korea Environment Industry & Technology Institute (KEITI)

[P-1-9] Ultraviolet Electroluminescence from $CaSiO_3$: Ce^{3+} Oxide in a Metal-oxide-semiconductor Structure

Mohammad M. Afandi, Jongsu Kim[†, *]

Department of Display Science and Engineering, Pukyong National University, Busan 48513, Korea

[†] Leading - Corresponding & Presenting author: jsukim@pknu.ac.kr
[*] Presenting author: jsukim@pknu.ac.kr

Abstract

An ultraviolet-light source is continuously required for general lighting applications. Herein, the ultraviolet electroluminescence (EL) from Ce^{3+}-singly doped $CaSiO_3$ (CSO) thin film on a silicon substrate has been reported for the first time. The EL device has a metal-oxide-semiconductor (MOS) structure which consists of two CSO and SiOx oxide layers on silicon wafer. Above the threshold voltage in AC power, it shows an ultraviolet EL spectrum with the broad two emission bands with 360 nm and 420 nm peaks due to the f-d transition of Ce^{3+} ions. With increasing Ce^{3+} concentrations, the lower-energy band (420 nm peak) gets more dominant due to the energy transfer from the higher-energy (360 nm peak) to the lower- energy (420 nm peak) bands. Furthermore, we demonstrate the EL-voltage transient behavior with a large hysteresis in a positive voltage polarity.

Keywords: *Ultraviolet, Electroluminescence, $CaSiO_3$:Ce^{3+}, Metal-oxide-semiconductor structure*

[P-1-10] A Study on the Design of Rock Crushing Machine for Mining Use

Tserendejid Bayarmaa[1, *], Haltar Chuluunbaatar[2, †]

[1] Department of Mechanical Engineering School of Technology of MUST, in Darkhan, Mongolia
[2] Department of Mechanical Engineering of MUST School of Mechanical Engineering and Transportation, Ulaanbaatar, Mongolia

[†] Leading - Corresponding author: chuluunbaatar@must.edu.mn
[*] Presenting author: bayarmaa@stda.edu.mn

Abstract

Recently, around 10 percent of the world's total delivered energy is used in the mining sector, where crushing and milling processes use about 60 percent of its, consuming more than any other end-use sector delivered energy. For crushing largely hard rock, impaction techniques are less consuming than other techniques, therefore, this study estimated the energy of unit force and impact of strike force with a surface of contacting between workpiece and material on the rock's strength and hard for optimizing complex theoretical basis of the crushing rock. Even though most researchers confirm that it needs to increase the unit strike energy with increasing work speed and weight of hydraulic hammer according to the excavator's weight for crushing large rock, this is contrary to the modern challenge as the preventing energy consumption of technology process. In this study, distribution and structure of strike's energy and causes of cracks in the rock by strike force were estimated, and objects of this study were a measurement of indenter speed, hydraulic hammer of experiment and a designed hydraulic hammer of excavator with twin indenters. A speciality of this study was the causes of interference of maximum shear stress into certain depth of rock defending the rock's nature when the twin indenter tends to get crushing.

Keywords: *Indenter, Rock, Excavator, Crushing, Hydraulic hammer*

[P-1-11] The Study on the Sintering Condition for Manufacturing of Sintered-wick Heat Pipe

Im-Nam Jang, Yong-Sik Ahn[*, †]

Department of Materials Science and Engineering, Pukyong National University, 48547, Busan, Korea

[†] Leading - Corresponding author: ysahn@pknu.ac.kr
[*] Presenting author: ysahn@pknu.ac.kr

Abstract

Effects of copper powder size, pore-forming agent and sintering conditions were investigated on the porosity, permeability and capillary force of porous sintered copper wick. The pore-forming agent ranging 15-45 wt.% was added to the Cu powder with the size of 100 ㎛, 150 ㎛ and 200 ㎛ respectively, and the mixture was sintered in a vacuum tube furnace. The necks between copper powder were formed over the sintering temperature of 900℃. The porosity using Archimedes measurement method and permeability performance of composite wicks increased with the amount of pore forming agent and showed the highest value at the Cu powder size of 150 ㎛ . To investigate the capillary force of sintered body risen meniscus test was conducted with ethanol as the working fluid. The capillary pressure increased with the increase of forming agent, and showed the highest value at the Cu powder size of 200 ㎛.

Keywords: *Capillary force, Permeability, Porosity, Sintering, Wick*

[P-1-12] Performance Evaluation of GCH_4-LOx Small Rocket Engine According to the Equivalence ratio Variation under a Fixed Combustion-chamber Pressure

Yun Hyeong Kang, Jeong Soo Kim[*, †]

Pukyong National University, 45 Yongso-ro, Nam-gu, Busan, 48513, Republic of Korea

[†] Leading - Corresponding author: jeongkim@pknu.ac.kr
[*] Presenting author: jeongkim@pknu.ac.kr

Abstract

A correlation between the propellant supply condition and chamber pressure in GCH_4-LOx small rocket engine was explored and hot-firing tests were conducted to analyze the engine performance characteristics according to the equivalence ratio variation under a fixed pressure of combustion chamber. Correlation studies have shown that the chamber pressure is linearly proportional to oxidizer supply pressure. As a result of the test, the main performance parameters of a rocket engine such as the thrust, specific impulse, and characteristic velocity were found to be enhanced as the equivalence ratio starting from a fairly fuel-lean condition approached the stoichiometric ratio (equivalence ratio of 1), but the efficiencies of characteristic velocity and specific impulse were on the contrary, in their dependency on the equivalence ratio.

Keywords: *Small rocket engine, Methane, Constant-chamber pressure, Equivalence ratio*

[P-1-13] Fabrication of Carbon Dots (CDs) Deposited Graphitic Carbon Nitrides for Photocatalytic CO_2 Reduction

Minh-Tri Nguyen-Le[1, 2, †, *], Young Soo Kang[3]

[1] Laboratory of Advanced Materials Chemistry, Advanced Institute of Materials Science, Ton Duc Thang University, Ho Chi Minh City, 758307, Vietnam

[2] Faculty of Applied Sciences, Ton Duc Thang University, Ho Chi Minh City, 758307, Viet Nam

[3] Department of Chemistry, Sogang University 121-741, Seoul, Korea

[†] Leading - Corresponding author: nguyenleminhtri@tdtu.edu.vn

[*] Presenting author: nguyenleminhtri@tdtu.edu.vn

Abstract

The artificial photosynthesis using photocatalysts to convert CO_2 into useful solar fuels is a promising means of sustainable energy-oriented use. Herein, a facile deposition of carbon dots (CDs) on graphitic carbon nitride (C_3N_4) photocatalyst for photocatalytic CO_2 reduction into solar fuels was reported. The CDs@C_3N_4 composites showed more enhanced visible light absorption and lower band gap energy than the pristine C_3N_4. The extended response to visible and NIR ranges, and narrower band gaps are probably due to the doping of C which introduces midgap states into the band gap energy of C_3N_4. Results determined by SEM, XRD showed that CDs were successfully deposited on C_3N_4. The synthesized materials had ability to convert CO_2 to MeOH after 8h, proving that CDs@C_3N_4 composites are promising candidates for photocatalytic CO_2 conversion.

Keywords: *Artificial, CO_2, Carbon nitrite, Photoreduction, Quantum dots*

[P-1-14] Reduction-responsive Carboxymethyl Cellulose-Based Soft Hydrogels for Cancer Therapy Application

Israr Ali[1], Sung-Han Jo[2], Sang-Hyug Park[2], Kwon Taek Lim[1, †, *]

[1] Department of Smart Green Technology Engineering, Pukyong National University, Busan 48513, Republic of Korea

[2] Department of Biomedical Engineering, Pukyong National University, Busan 48513, Republic of Korea

[†] Corresponding author: ktlim@pknu.ac.kr

[*] Presenting author: ktlim@pknu.ac.kr

Abstract

In this work, novel biocompatible and reduction-responsive soft hydrogels were formulated from norbornene (Nb)-functionalized carboxymethyl cellulose (CMC-Nb). To cross-link the CMC-Nb via a highly biorthogonal inverse electron demand Diels-Alder (IEDDA) reaction, we employed a water-soluble and reduction-responsive diselenide-based cross-linker possessing two terminal tetrazine (Tz) groups with varying molar concentrations (Nb/Tz molar ratios of 10/10, 10/05, and 10/2.5). The N2 microbubbles liberated as a by-product during the IEDDA reaction generated in-situ pores in hydrogel networks. The resulting hydrogels had highly porous structures and relatively soft mechanical properties (storage moduli in the range 74 ~160 Pa). The hydrogels showed high swelling ratios (>35 times), tunable gelation times (1-5 min), and excellent doxorubicin (DOX) loading efficiencies (>85 %). The hydrogels exhibited stimuli-responsive and fast release of DOX (99 %, after 12 h) in the presence of 10 mmol of glutathione as compared to the normal PBS solution (38 %). The cytotoxic effects of blank hydrogels were not observed against HEK-239 cells, while the DOX-encapsulated hydrogels exhibited antitumor activity in BT-20 cancer cells. The results indicate potential applications of the CMC-based soft hydrogels in injectable drug delivery systems.

Keywords: *Carboxymethyl cellulose, Tetrazine click chemistry, Reduction responsive hydrogels, Porous hydrogels*

[P-1-15] Experimental Evaluation of the Electrical and Thermal Efficiency of Dual Duct PV/T Collectors

Seongbhin Kim[1], Kwangam Moon[1], Kwnaghwan Choi[2, *, †]

[1] Graduate School of Refrigeration and Air Conditioning Engineering, Pukyong National University, Busan, 48513, Republic of Korea
[2] Department of Refrigeration and Air Conditioning Engineering, Pukyong National University, Busan, 48513, Republic of Korea

[†] Leading - Corresponding author: choikh@pknu.ac.kr
[*] Presenting author: choikh@pknu.ac.kr

Abstract

The purpose of this study is to evaluate the electrical and thermal efficiencies of a novel type of photovoltaic/thermal(PV/T) collector experimentally on actual climate conditions in Korea. The PV/T collector using air as fluid normally has low thermal efficiency because of the low heat conductivity of air. Thus, the PV/T collector, which was designed and tested in this study, had an air channel above and below the PV cell and turbulence promoter to maximize its thermal performance. As a result, the electrical and thermal efficiencies showed 14-15% and 40-50%, respectively.

Keywords: *PV/T, Dual duct, Experiment, Electrical efficiency, Thermal efficiency*

[P-1-16] Motion Control for Two-wheeled Mobile Inverted Pendulum Using a MIMO Robust Servo Controller

Dae Hwan Kim[1, *, †], Hyuk Yim[2]

[1] Realmaker.Inc, R304 B23 Sinseon-ro, Nam-gu, Busan, KS012, Republic of Korea

[2] Nsquare.Inc, 11-3,4sandan 5-gil, Jiksan-eup,Seobuk-gu, Cheonan-si, KS002, Republic of Korea

[†] Leading - Corresponding author: dhkim@realmaker.kr

[*] Presenting author: dhkim@realmaker.kr

Abstract

This paper proposes a MIMO robust servo controller design for two-wheeled Mobile Inverted Pendulums (MIPs) with an external disturbance to track desired linear displacement and orientation reference inputs using a linear shift invariant differential (LSID) operator. To do this task, the followings are done. Firstly, based on Newton's 2nd law, the modeling of the two-wheeled MIP is presented. Secondly, by operating the LSID operator to the state space model and the output error vector, a new extended system and a new control law are obtained. Thirdly, a proposed MIMO robust servo controller for the given two-wheeled MIP is designed by using the pole assignment approach. Fourthly, by operating the inverse LSID operator, a servo compensator for the MIMO system is obtained. Finally, in order to verify the effectiveness of the proposed MIMO robust servo controller, the simulation results are shown. The simulation results show the good tracking performance of the proposed MIMO robust servo controller under a step type of disturbance and the step linear displacement and angular reference signals, and their significance.

Keywords: *MIMO, MIP, LSID, Operator, Robust servo controller*

[P-1-17] Ultraviolet Electroluminescent Sensor in Metal-oxide-semiconductor Structure

Mohammad M. Afandi, Jongsu Kim[†, *]

Department of Display Science and Engineering, Pukyong National University, Busan 48513, Korea

[†] Leading - Corresponding & Presenting author: jsukim@pknu.ac.kr

[*] Presenting author: jsukim@pknu.ac.kr

Abstract

The desire for multifunctional and integrated electronic devices has been constantly developed by emerging more than one function, which is beneficial in novel applications, space-saving, as well as cost-effectiveness. Herein, a multifunctional ultraviolet-A (UV-A) emitting and solar-blind UV photo-detecting device was fabricated using a wide bandgap ZnGa2O4 oxide layer in a metal-oxide-semiconductor structure. The film was formed on the silicon substrate through a facile solid-state reaction all-solution precursor process. The strategy to achieve bi-functionality was demonstrated by changing the electric configurations. Under a sinusoidal AC source, it emits broad UV-A light, while under UV irradiation, it presents a photo-current response with the help of an external electric field from DC bias.

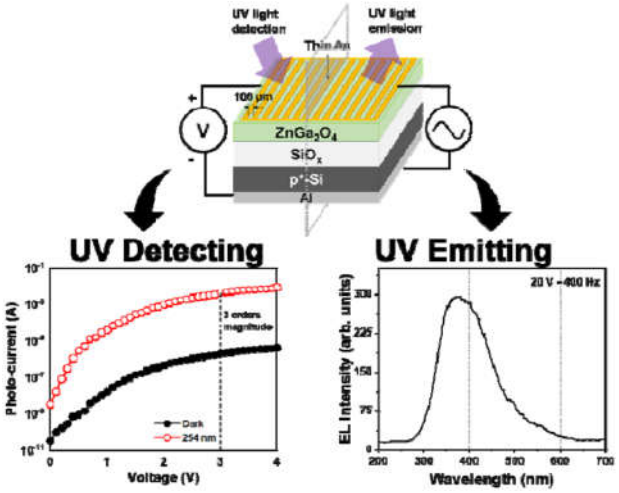

Figure 1. Ultraviolet electroluminescent sensor in a metal-zinc gallate oxide-semiconductor structure: (left) photocurrent curve and (right) EL spectrum as detecting and emitting device, respectively.

Keywords: *Ultraviolet, Electroluminescence, Zinc gallate ($ZnGa_2O_4$), Metal-oxide-semiconductor structure*

[P-2-1] Switching Control of Nonlinear Systems with Multiple Inputs and Multiple Outputs

Seon Geon Kim[1], Seong Woo Kwak[2, *, †], Nam Ho Kim[2], Yeong Yeun Hwang[2], Marn Go Kim[2], Kyung Chang Lee[2], Chun Kwon Lee[2], Byung Gwon Cho[3]

[1] Department of Robot Engineering, Pukyong National University, Busan 48513, Republic of Korea

[2] Department of Control and Instrumentation Engineering, Pukyong National University, Busan 48513, Republic of Korea

[3] Department of Display and Semiconductor Engineering, Pukyong National University, Busan 48513, Republic of Korea

[†] Leading - Corresponding author: ksw@pknu.ac.kr

[*] Presenting author: ksw@pknu.ac.kr

Abstract

Twin rotor multi-input multi-output system (TRMS) is a laboratory setup, which resembles a helicopter with unstable, nonlinear, and coupled dynamics. In this paper, we design a new controller which combines two conventional controllers using a switching technique. A sliding mode controller with input/output linearization and a state feedback controller with Jacobian linearization are designed separately. In our algorithm, one controller is switched to the other based on the square of error and derivative error. It is revealed that the combined controller produces improved performance than the single one.

Keywords: *Multiple input and multiple output, Nonlinear system, Switching control, Twin rotor system*

[P-2-2] Distribution Cable Fault Location Using Line Impedance Resonance Analysis

Chun-Kwon Lee[†,*], Nam-Ho Kim, Yeong-Yeun Hwang, Marn-Go Kim, Kyung-Chang Lee, Seong Woo Kwak

Department of Control and Instrumentation Engineering, Pukyong National University, Busan, 48513, Korea

[†] Leading - Corresponding author: ck.lee@pknu.ac.kr
[*] Presenting author: ck.lee@pknu.ac.ckr

Abstract

The most crucial element for the effective operation of the power system is the distribution cable, which transmits control and instrumentation data and electricity supplementation. Therefore, there is a growing need for cable diagnostic methods that offer accurate status monitoring and problem identification in cables. The use of reflected signal measurement technology to find the locations of fault or impedance mismatch inside cables started in earnest as radar, which was first developed for military usage, was put to use for civilian applications. This study proposes a method for pinpointing faults that uses frequency domain data processing, which is line impedance resonance analysis (LIRA). Frequency domain reflectometry applies a stepped frequency sinusoidal signal whose frequency grows linearly to a distribution cable in the frequency domain, in contrast to the conventional time-domain reflectometry methods. By examining the reference sinusoidal signal and the reflected wave in the frequency domain, the fault location is calculated. Results from experiments on fault location and the classification of reflected signals in subsea distribution cable have confirmed the utility of the suggested technique.

Keywords: *Reflectometry, Cable diagnosis, Fault location, Line impedance resonance analysis, Distribution cable*

[P-2-3] Inspection of Welding Bead Defectiveness Using Brightness Values

Jae Eun Lee, Yong-Bong Kim, Jong-Nam Kim[*, †]

Division of Computer Engineering and AI, Pukyong National University, 45, Yongso-ro, Nam-gu, Busan, 48516, Korea

[†] Leading - Corresponding author: jongnam@pknu.ac.kr
[*] Presenting author: jongnam@pknu.ac.kr

Abstract

Welding is used in various industries such as automobiles, construction, shipbuilding, and machinery industries, and plays an important role in determining productivity. Therefore, welding quality inspection is essential to determine whether the product is perfect or defective. In this study, we first inspect the quality of the welding bead by calculating brightness values in the vertical direction of the image. We implement the inspection algorithm based on the distribution of the brightness value by finding a position corresponding to 50% of the height. We determine the welding bead margins based on the predefined threshold. Secondly, we inspect the quality of the welding bead by dividing it in a horizontal direction. After that, we inspect the quality of the welding bead. In this method, we can reduce the time complexity by designating the area of interest where the bead is located. In addition, this method improves accuracy based on the difference in brightness values between the background and the welding bead.

Keywords: *Brightness value, Region of interest, Quality inspection, Segmentation, Welding bead*

[P-2-4] Test Bed Methods for Big Data Collection Based on Klean IoT API

Vandha Pradwiyasma Widartha, Yeonjee Choi, Chang Soo Kim[*, †]

Division of Computer Engineering and AI, Pukyong National University, 45, Yongso-ro, Nam-gu, Busan, 48516, Korea

[†] Corresponding author: cskim@pknu.ac.kr

[*] Presenting author: cskim @pknu.ac.kr

Abstract

This paper studies design methods for web-based test bed monitoring of data such as ozone, volatile organic compounds, temperature, and humidity collected from Klean air sterilizer device. To this end, we design a web-based system configuration for real-time data collection using the Klean IoT API, and design a prototype system to analyze the collected data. The system environment designs Django Framework-based Mongo DB design and major functions for monitoring the client.

Keywords: *Plasma, Indoor air sterilization, IoT API, Big data collection, Test bed method*

[P-2-5] Application of Dimension Reduction Techniques for Similar Data Search in Oceanographic Observation Archives

Wonjun Jung, Oh-Heum Kwon, Ha-Joo Song[*, †]

Puyong National University, Yongsoro 45, Busan, 48513, South Korea

[†] Leading - Corresponding author: hajoosong@pknu.ac.kr
[*] Presenting author: hajoosong@pknu.ac.kr

Abstract

Oceanographic observation data often reaches more than tens of gigabytes in size because it holds data from the past decades. Therefore, it takes several tens of minutes or more to compare and search data one by one to find historical observations similar to observation data at a certain point in time. This paper presents a technique that can shorten the search time by using a dimension reduction technique using an autoencoder, one of the deep learning algorithms. The proposed technique compresses the original data for each observation data and then uses an autoencoder to extract feature vectors and construct an array of feature vectors. At the time of search, a candidate group is extracted by comparing the similarity between the feature vector of the search data and the stored feature vector array. The candidate group and the search data are compared at the original scale to find the most similar one. We conducted performance tests using satellite observation data stored in netCDF format. The proposed method showed performance improvement of around four times in terms of search speed while occupying less additional storage space.

Keywords: *netCDF, AutoEncoder, Similarity search*

[P-2-7] Fish Size Detection for a Fish Farm by Using Deep Learning

Moon G. Joo [†, *]

Pukuong national university, Yongso-ro 45, Busan, 48513, S. Korea

[†] Leading - Corresponding author: gabi@pknu.ac.kr
[*] Presenting author: gabi@pknu.ac.kr

Abstract

We have developed a device that automatically measures the size of fish in fish farms. The device receives the image from the CCTV using the RTSP protocol and locates the fish and the sticks that know the size by YOLO3, one of the deep learning methods. The calculated fish size information is stored in the DB and provided as a graph to check the growth of the fish.

Keywords: *Deep learning, Fish farm, Fish size detection, RTSP, YOLO3*

[P-2-8] Spontaneous Conformational Changes and Functions of Angiotensin I Converting Enzyme

Myunggi Yi[1, 2, *, †], Thi Tuong Vy Phan[3], Seong-Yeong Heo[4], Won-Kyo Jung[1, 2]

[1] Major of Biomedical Engineering, Division of Smart Healthcare, Pukyong National University, Busan, 48513, South Korea

[2] Industry 4.0 Convergence Bionics Engineering, Pukyong National University, Busan, 48513, South Korea

[3] Center for Advanced Chemistry, Institute of Research and Development, Duy Tan University, Danang 550000, Vietnam

[4] Jeju Marine Research Center, Korea Institute of Ocean Science & Technology, Jeju, 63349, South Korea

[†] Leading - Corresponding author: myunggi@pknu.ac.kr

[*] Presenting author: myunggi@pknu.ac.kr

Abstract

The inhibition of human angiotensin I converting enzyme (ACE) has been regarded as a promising approach for the treatment of hypertension. Despite its importance and research attempts over many years, the mechanisms of activation and inhibition of ACE remain understudied. We have performed all atom molecular dynamics simulations of ACE with and without several ligands and present the results. Two types of inhibitors, competitive (bradykinin potentiating peptide b) and mixed non-competitive (*Spirulina* derived heptapeptide), were used to model the ligand bound forms. In the absence of a ligand the simulation showed spontaneous large hinge-bending motions of multiple conversions between the closed and open states of ACE, while the ligand bound forms were stable in the closed state. Our simulation results imply that the equilibrium between pre-existing backbone conformations shifts in the presence of a ligand. The hinge-bending motion of ACE is considered as an essential to the enzyme function. In addition, the heptapeptide derived from *Spirulina* from our molecular dynamics simulation showed the inhibition mechanism of a mixed non-competitive inhibitor together with angiotensin I, which is the product of the enzyme function. A mechanistic model of activation and the inhibition may provide valuable information for novel inhibitors of ACE.

Keywords: *Activation and inhibition mechanism, Angiotensin converting enzyme, Hinge-bending motion, Molecular dynamics simulation, Spontaneous conformational change*

[P-2-9] CNN and Vision Transformer-based for Video Deepfake Detection

Ki-Ryong Kwon[†, *]

Division of Computer Engineering and AI, Pukyong National University, 45, Yongso-ro, Nam-gu, Busan, 48516, Korea

[†] Leading - Corresponding author: krkwon@pknu.ac.kr

[*] Presenting author: krkwon@pknu.ac.kr

Abstract

Models that can create and synthesize hyper-realistic data using deep learning, often known as Deepfake, are rapidly advancing. With the rise of Deepfake videos, some convolutional neural network classifiers can recognize fake videos. However, previous research based on the Convolution Neural Network (CNN) architecture, on the other hand, had problems with not only overfitting, but also misjudging fake content as real. In this paper, we propose the use of Vision Transformer (ViT) and Convolutional Neural Network (CNN) to detect Deepfake.

Keywords: *CNN, ViT, Deepfake*

[P-2-10] SARS-CoV-2 Omicron RBD Binds More Weakly to hACE2 Than Delta RBD, as Shown by the Coarse-grained Model

Thanh Hoa Le[1, 2, †], Linh Hoang Tran,[3, 4, †] Nguyen Thanh Tung[5, 6], Son Tung Ngo[1, 7, *], Huong Thi Thu Phung[8, *]

[1] Laboratory of Theoretical and Computational Biophysics, Advanced Institute of Materials Science, Ton Duc Thang University, 19 Nguyen Huu Tho, District 7, Ho Chi Minh City, 70000, Vietnam
[2] Faculty of Applied Sciences, Ton Duc Thang University, 19 Nguyen Huu Tho, District 7, Ho Chi Minh City, 70000, Vietnam
[3] Faculty of Civil Engineering, Ho Chi Minh University of Technology (HCMUT), 268 Ly Thuong Kiet, District 10, Ho Chi Minh City, 70000, Vietnam
[4] Vietnam National University, Ho Chi Minh City, 70000, Vietnam
[5] Institute of Materials Science, Vietnam Academy of Science and Technology, 18 Hoang Quoc Viet, Cau Giay District, Hanoi, 10000, Vietnam
[6] Graduate University of Science and Technology, Vietnam Academy of Science and Technology, 18 Hoang Quoc Viet, Cau Giay District, Hanoi, 10000, Vietnam
[7] Faculty of Pharmacy, Ton Duc Thang University, 19 Nguyen Huu Tho, District 7, Ho Chi Minh City, 70000, Vietnam
[8] NTT Hi-Tech Institute, Nguyen Tat Thanh University, 300A Nguyen Tat Thanh, district 4, Ho Chi Minh City, 70000, Vietnam

[†] Leading - Corresponding author: ngosontung@tdtu.edu.vn and ptthuong@ntt.edu.vn

[*] Presenting author: lethanhhoa1@tdtu.edu.vn

Abstract

As in 2022, COVID-19 remains a global epidemic, and Omicron is still the predominant variant. An understanding of the residues involved in the binding mode of the spike protein of SARS-CoV-2 with the receptor human Angiotensin-Converting Enzyme 2 (hACE2) is essential to elucidate the initial stage of pathogenesis pathway and to guide the process of drug screening, design and development. We aimed to utilize molecular docking and steered-molecular dynamics (SMD) simulations to explore the binding mechanism of SARS-CoV-2 Delta/Omicron receptor binding domain (RBD) to hACE2. The binding pose between RBD and hACE2 predicted by docking was in agreement with the experimental structure. In preparation of the SMD simulation to estimate the binding affinity of Delta/Omicron RBD with hACE2, we parameterized the system using Martini 3 coarse-grained model and force field. The obtained results concurred with the respective experiment that Omicron RBD was associated with a weaker binding affinity to hACE2 compared to Delta RBD.

Keywords: *Angiotensin-converting enzyme 2, Coarse-grained model, Molecular docking, SARS-CoV-2 spike protein, Steered molecular dynamics*

[P-2-11] A Self-attention-based Feature Learning Framework for Visual Localization

Dae Hwan Kim[1, *, †], Hung Nguyen Huy[2]

[1] Realmaker Inc, R304 B23 Sinseon-ro, Nam-gu, Busan, KS012, Republic of Korea

[2] Saigon University, 273 An Duong Vuong Street, Ward 3, District 5, Ho Chi Minh City 700000, Vietnam

[†] Leading - Corresponding author: dhkim@realmaker.kr

[*] Presenting author: dhkim@realmaker.kr

Abstract

Visual camera localization can be defined as a computer vision problem, which aims to retrieve the pose of a camera given a query image which was originally captured by the camera. This paper proposes a new deep-learning architecture for indoor visual camera localization. Our deep learning framework uses deep spatial points in low-level feature maps as input to precisely model the scene coordinate regression problem. The proposed approach focuses on learning important and invariant visual deep features, which removes the variance between the different level feature representations and combines multi-scale context information. We implement a robust training pipeline that provides an attention-based feature map with straight regulation from the ground truth to enhance pose estimation accuracy. Comprehensive experiments show how our approach achieves comparable performance against previous methods on the indoor benchmark 7-Scens dataset.

Keywords: *Camera relocalization, Deep learning, Indoor scenes, Pose estimation*

[P-2-12] Energy Efficiency Optimization for UAV-enabled Finite Block Length Backscatter Communications

Tran Manh Hoang[1, 2], Ba Cao Nguyen[1, 2], Pham Thanh Hiep[3], Phuong T. Tran[4, †, *]

[1] Telecommunications University, Nha Trang 650000, Vietnam

[2] School of Information and Communication Engineering, Chungbuk National University, Cheongju 28644, South Korea

[3] Faculty of Radio, Le Quy Don University, Hanoi City 6000, Vietnam

[4] Wireless Communications Research Group, Faculty of Electrical and Electronics Engineering, Ton Duc Thang University, 19 Nguyen Huu Tho Street, Tan Phong Ward, District 7, Ho Chi Minh City 729000, Vietnam

[†] Leading - Corresponding author: tranthanhphuong@tdtu.edu.vn

[*] Presenting author: tranthanhphuong@tdtu.edu.vn

Abstract

In this paper, an Internet-of-Things (IoT) system, where an unmanned aerial vehicle (UAV) is utilized to assist the wireless energy charging for terrestrial tags and then collect data via backscatter communication of them with finite block length, is proposed and analyzed. The block error rate (BLER), energy efficiency (EE), and spectrum efficiency (SE) are derived to evaluate the proposed system performance. In particular, the BLER expression is approximated by using Gaussian-Chebyshev quadrature and the first-order Riemann integral. We formulate an optimization problem to maximize the EE and minimize the transmit power, which is solved by using a searching algorithm. The energy and SE with respect to the number of transmission bits is investigated to show that the system performance can be maximized by selecting an appropriate number of transmission bits and the altitude of the UAV. Finally, simulations are conducted to verify the accuracy of our analysis.

Keywords: *Backscatter, BLER, energy efficiency, spectrum efficiency, UAV, URLLC*

[P-3-1] Evaluation of Ventilation Performance in a Multi-use Facility for the Preparedness to Prevent the next Pandemic

Chul Kim[*, †], Kyu Nam Rhee, Gun Joo Jung

Department of Architectural Engineering, Pukyong National University, Busan, 48513, Republic of Korea

[†] Leading - Corresponding author: chulkim@pknu.ac.kr

[*] Presenting author: chulkim@pknu.ac.kr

Abstract

During the last three years, we have experienced unprecedented and unfortunate situations due to COVID-19. The vulnerability of architectural design and systems caused the airborne spread and weakness in the management of bioaerosols in buildings. Especially community spread and cluster infections were mostly found in multi-use facilities because those facilities are typically used by the unspecified public, and no mask environment is inevitable during their meal time in restaurants and cafes. However, in many cases, the existing ventilation systems were not planned in system design, capacity, and type to perform recommendations from health authorities and professional societies using outdoor air against COVID-19. Therefore, for the preparedness to prevent the next pandemic, we need to diagnose the ventilation performance of existing multi-use facilities (i.e., café) and then develop a ventilation system design and operation guidelines as a reference to improve the current national codes and conventional HVAC design practice. To do this, this study experimented with ventilation performance using virus-similar particles depending on ventilation modes (i.e., closed and naturally ventilated conditions) in a café in Korea. Under the typical operation modes of the VRF system on the ceiling, the behavior and transmission of virus-similar particles were monitored for 30 minutes in six sensor points (i.e., counter, dining space). The experiments revealed that natural ventilation distinctly mitigated the densities of virus-similar particles in most sensing points, which identified the usefulness of natural ventilation as an effective control measure. However, the densities of virus-similar particles in some points were not fully back to their original PM (particulate matter) densities before the experiment. This fact means that additional mechanical ventilation equipment should be considered in the case study café to improve insufficient and unbalanced local ventilation performance in indoor spaces. The findings of this study will provide evidence to perform an evaluation of ventilation performance in more multi-use facilities and to understand airborne infection and virus transmission behavior in the indoor air due to indoor airflow (i.e., HVAC systems).

Keywords: *Field measurement, Infectious disease, Multi-use facility, Preparedness, Ventilation*

[P-3-3] Development of an Evacuation Model for Fire Safety Managers

Ryun-Seok Oh[1, *], Young-Hoon Bae[2], Joon-Ho Jeon[3], Jun-Ho Choi[3, †]

[1] Industry-University Cooperation Foundation, Pukyong National University, 45 Yongso-ro, Nam-gu, Busan 48513, South Korea

[2] Research Institute of Intelligent Fire Safety Technology and Human Behavioural Science, Pukyong National University, 45 Yongso-ro, Nam-gu, Busan 48513, South Korea

[3] Division of Architectural and Fire Protection Engineering, Pukyong National University, 45 Yongso-ro, Nam-gu, Busan 48513, South Korea

[†] Leading - Corresponding author: jchoi@pknu.ac.kr

[*] Presenting author: kaing367@gmail.com

Abstract

A fire safety manager establishes evacuation plans such as designating the shortest evacuation route and arrangement of evacuation staff, for building fire safety in South Korea. According to previous studies, the placement of evacuation staff shortened evacuation time by about 46%. This means that the work of the fire safety manager has a great influence on the safety of the evacuees. However, the current education program for establishing an evacuation plan for fire safety managers relies only on theoretical education. In addition, since there is no simulation software that can help fire safety managers establish evacuation plans, there is no way to quantitatively evaluate the effectiveness of evacuation plans. In the case of buildingEXODUS and Pathfinder, which are evacuation model mainly used in South Korea, they are used by experts, and it is difficult for safety managers to use the programs because they require a high level of expertise. Therefore, we are developing an evacuation model customized for fire safety managers that can secure both the convenience of the user interface and the reliability of fast calculation results, and a prototype has been developed. In this paper, we would like to introduce the fire and evacuation model we developed.

Keywords: *Fire safety manager, Evacuation model, Fire model*

[P-3-4] Rainfall-runoff-inundation Assessment Based on the Radar Rainfall Database from the Global Precipitation Climatology Centre: A Case Study in North-central Vietnam

Nguyen Van Toan[*, †]

Thuyloi University Southern Campus, 02 Truong Sa Street, Ward 17, Binh Thanh District, Ho Chi Minh City, 72321, Vietnam

[†] Leading - Corresponding author: toannv@tlu.edu.vn

[*] Presenting author: toannv@tlu.edu.vn

Abstract

North-Central Vietnam has suffered annually from complex and far-reaching floods resulting from heavy rain. As of November 15th, 2020, the floods had resulted in over 233 fatalities, 66 people missing, and damaged almost 35.2 trillion VND (~US$ 1.52 billion) in this area in 2020. General climate and topographic characteristics of North-Central Vietnams are narrow horizontal terrain and steep river alongside heavy rains annually. The analysis and forecast of floods caused by heavy rain have been an urgent issue for this area, especially severe natural disaster floods, to assess the influence of climate change. This study presents a computer-based approach to investigate HaTinh province as a case study of North-Central Vietnam under heavy rain in October 2020. A rainfall-runoff-inundation (RRI) model was developed with actual topographic data and radar rainfall data inputs, taking reservoirs upstream into account. The hourly rainfall data was extracted from the radar rainfall database from the Global Precipitation Climatology Centre (GPCC) using Opengrads in the MobaXterm operating platform loaded to the area. Surface/subsurface flow conditions were considered in the model by adjusting the permeability coefficient responding to types of soil cover. Thus, the sophisticated numerical model simulated the streamflow discharge of the basin during the studied period, October 1st to 31st. Floods resulting from rainfall input reflected flooding behaviors on the basin. Results indicate that the RRI model using GPCC's data is a reasonable and predictive method for study and investigation due to reflecting the actual behavior of the basin region. Therefore, the present approach is suitable for rapidly forecasting flood scenarios due to heavy rain. The key findings show that the inundation depth depends on upstream and surface/subsurface flow conditions adjusted to the reservoirs. The computer-based approach is a potential method to simulate and examine floods downstream with a cost matching. The study provides valuable insights into the heavy rainfall model's procedural aspects and evaluation of its effects on downstream regions.

Keywords: *Computer-based approach, Heavy rain, North-central Vietnam, Rada rainfall database, Rainfall-runoff-inundation model*

[P-3-5] Production Capacity Planning in Uncertain Time Condition: A Case Study at a Plastic Manufacturing Company

Tran Lan Anh[†, *] and Phan Thi Mai Ha

Ho Chi Minh City University of Technology, HCM City, 742620, Vietnam

[†] Leading - Corresponding author: anh.tranbku.k1985@hcmut.edu.vn
[*] Presenting author: anh.tranbku.k1985@hcmut.edu.vn

Abstract

This paper considers a capacity planning problem in uncertainty time condition. Although production capacity planning is an important part of the production planning process, it has received insufficient attention in practice. Companies usually implement capacity planning in terms of deterministic production time, ignoring or paying little attention to time uncertainty factors. The Covid-19 pandemic, as well as a series of tumultuous events in recent years, have caused businesses and manufacturing companies to plan over time to inevitably experience a lot of deviation in planning results compared to reality, resulting in underproduction or excess production far more than the forecast results. The case study of this study will focus on building a new production capacity planning model for the production process of the 5-compartment plastic cabinet, a key product in the household products of the company. To build the model, the first step is analyzing each stage of the employee's job performance by determining the time level which includes both deterministic and indeterminate time (start-up time, error compensation time, machine downtime). The next step is investigating the use of Monte Carlo simulation to simulate the production capacity planning process in an uncertain time. The study's findings indicate that the construction model has a positive impact and significantly reduces the deviation of the plan from reality. Furthermore, the model is applicable to other manufacturing cases.

Keywords: *Capacity planning, Uncertainty, Simulation, Monte Carlo, Work design, Production planning*

The 2023 International Symposium on Advanced Engineering - ISAE2023

PUKYONG NATIONAL UNIVERSITY 부경대학교, Khoa học và Công nghệ, Trường Đại học Bách Khoa, Đại học Quốc gia Thành Phố Hồ Chí Minh

NHÀ XUẤT BẢN ĐẠI HỌC QUỐC GIA THÀNH PHỐ HỒ CHÍ MINH

Trụ sở:
Phòng 501, Nhà Điều hành ĐHQG-HCM, phường Linh Trung, thành phố Thủ Đức, Thành phố Hồ Chí Minh.
ĐT: 028 62726361
E-mail: vnuhp@vnuhcm.edu.vn

Văn phòng đại diện:
Tòa nhà K-Trường Đại học Khoa học Xã hội & Nhân văn, số 10-12 Đinh Tiên Hoàng, phường Bến Nghé, Quận 1,Thành phố Hồ Chí Minh
ĐT: 028 62726390
Website: www.vnuhcmpress.edu.vn

Chịu trách nhiệm xuất bản và nội dung
TS ĐỖ VĂN BIÊN

Biên tập
SIN KẾ DUYÊN

Sửa bản in
NHƯ NGỌC

Trình bày bìa
LÊ THANH LONG

Đối tác liên kết
PHÒNG THÍ NGHIỆM TRỌNG ĐIỂM
ĐIỀU KHIỂN SỐ VÀ KỸ THUẬT HỆ THỐNG

Xuất bản lần thứ 1. Số lượng in: 200 cuốn, khổ 20 x 29 cm. Số XNĐKXB: 594-2023/CXBIPH/2-08/ĐHQGTPHCM. QĐXB số: 28/QĐ-NXB cấp ngày 17/3/2023. Công ty TNHH Dịch vụ - Kỹ thuật Đức Cảnh. Địa chỉ: 42/6/2 đường Đồng Xoài, Phường 13, Quận Tân Bình, TP.HCM. Nộp lưu chiểu: Năm 2023.
ISBN: **978-604-73-9697-9**.

SPONSORS

ISBN:978-604-73-9697-9
SÁCH KHÔNG BÁN